A Numerical Analysis of the Flow in a Carousel Wind Tunnel in Martian Atmospheric Conditions

S. Van Dam

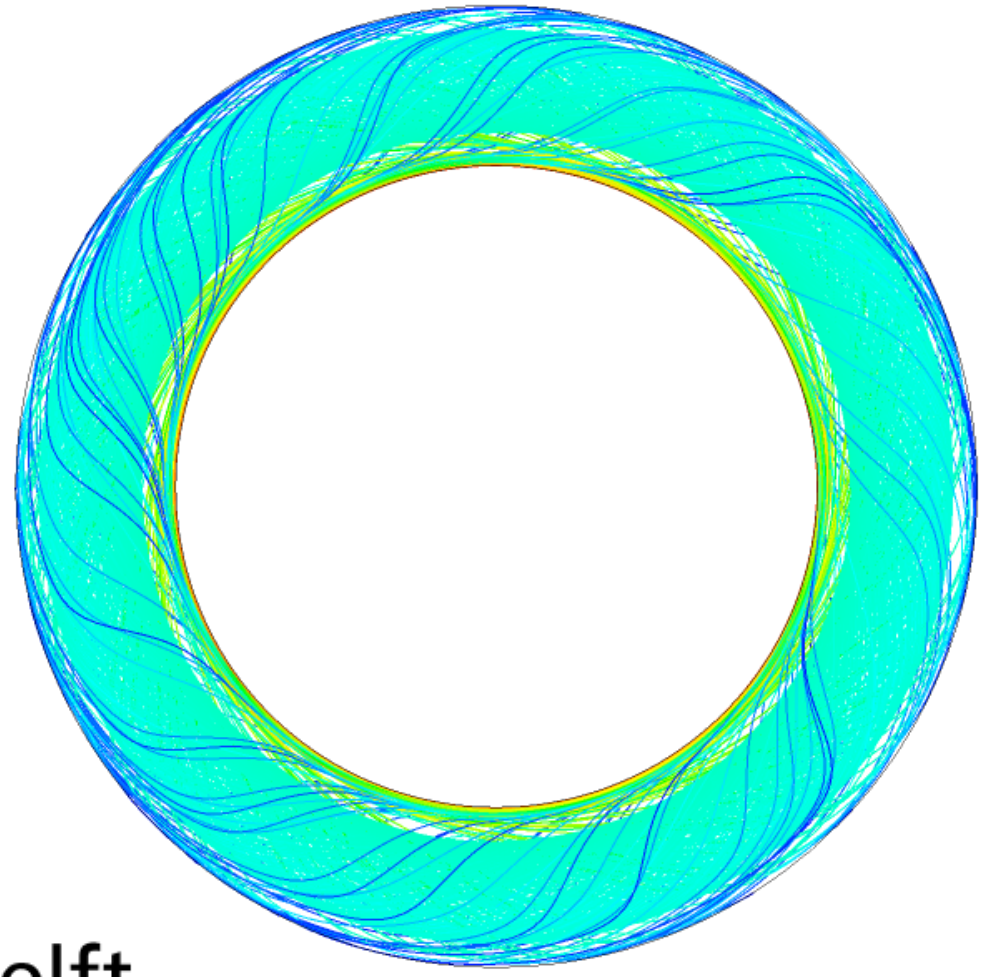

TU Delft

A Numerical Analysis of the Flow in a Carousel Wind Tunnel in Martian Atmospheric Conditions

by

S. Van Dam

to obtain the degree of Master of Science at the Delft University of Technology,
to be defended publicly on Monday December 12, 2022 at 14:00.

Student number:	4674901	
Project duration:	January 7, 2022 – December 12, 2022	
Thesis committee:	Dr. F. Avallone,	TU Delft, Assistant Professor
	Dr. S.J. de Vet,	TU Delft, Lecturer
	T. Michelis,	TU Delft, Postdoc Researcher
	Dr. D. Ragni,	TU Delft, Associate Professor

An electronic version of this thesis is available at `http://repository.tudelft.nl/`.

TU Delft

Abstract

With new rovers landing on Mars, like the Perseverance rover in 2020, the interest in Mars has grown recent years. The atmospheric conditions on Mars result in challenging conditions due to its low density atmosphere and extremely low temperatures. With a density on Mars that is 1% of that on Earth, creating sufficient lift for vehicles to fly becomes a challenge. The low density results in low Reynolds numbers. The low temperature has an effect on the speed of sound, due to which the Mach number is significantly higher at the same flow velocity compared to Earth. Airfoil data at these conditions, low Reynolds number - high Mach number, are sparse, but crucial for design of aerial vehicles. Next to the aerodynamic conditions, dunes on Mars are formed and migrate. The parameter of interest which defines the conditions required for transportation of particles is the threshold shear velocity. This parameter has been determined by different analytical expressions. However, the outcome remains a broad range, which point out the difficulty and inaccuracy of the results. Therefore, in this document, the design of a carousel wind tunnel is investigated to determine its feasibility to perform aerodynamic and aeolian measurements. The carousel wind tunnel consists of two concentric drums, of which the inner one rotates. The carousel wind tunnel is analysed by a computational fluid dynamics analysis with the k - ω turbulence model. The results indicate that due to secondary flow effects and the wake of a test object, no accurate aerodynamic measurements can be performed. Aeolian measurements are deemed feasible, with increased accuracy at sufficiently high rotational velocities.

Preface

Now that I've finished my thesis, my time as a student almost comes to an end. I would like to dedicate this page to all who have supported me during this, often difficult, but captivating journey at the Delft University of Technology to obtain the degree of Master of Science.

First of all, I would like to thank my supervisors Theo, Sebastiaan, Francesco and Daniele. Theo and Sebastiaan for their weekly inputs which helped me stay on track to answer the research questions. Without their continuous supervision and the numerous meetings we had, this thesis would not have become what it is today. Francesco and Daniele, for their judgements which allowed me to gain new insights. They have helped me greatly in critically assessing my results.

Secondly, I would like to thank my friends and girlfriend Babeau. My friends, both in Delft and Belgium, who where always ready to take my mind of the thesis. Without every now and then taking my mind of my thesis, it would not have been possible to finish this research, for that I thank you. Babeau, for her support she gave me to persist these last months. Her interest in my research kept me motivated and made me feel my research was making a contribution to the world of science.

Lastly, I would like to thank my incredible supportive parents. The unconditional support they provided made the last several months took weight of my shoulders. Not only the last several months, but the last six years of my study they have shown me great support for which I am eternally grateful.

My time as a student would have been much less memorable without everyone I have mentioned (and everyone I forgot). I will never forget this experience, it was an exciting and memorable time!

S. Van Dam
Delft, September 2022

Contents

List of Figures

List of Tables

List of Symbols – 1

Symbol	Explanation
a	Speed of Sound
A	Cross Sectional Area
B	Empirical Constant Law of the Wall
c_a	Axial Force Component
c_n	Normal Force Component
C_d	Constant in Turbulence Model
C_d'	Uncorrected Drag Coefficient
C_D	Drag Coefficient
C_f	Friction Coefficient
C_l	Lift Coefficient
C_p	Pressure Coefficient
CO_2	Carbon Dioxide
H	Shape Factor
k	Turbulence Kinetic Energy
k_{cr}	Critical Wave Number
L	Length
M	Mach Number
p	Static Pressure
p_∞	Freestream Static Pressure
q_∞	Freestream Dynamic Pressure
R	Gas Constant
Re	Reynolds Number
R^2	Coefficient of Determination
S	Sutherland's Temperature Constant
$\overrightarrow{S}$	Rate of Strain
T	Temperature
Ta	Taylor Number
u	Velocity Component in X-direction
U'	Undisturbed Velocity
u_*	Shear Velocity
$\overline{U}$	Average Velocity
v	Velocity Component in Y - direction
V	Velocity
V_∞	Free Stream Velocity
y	Distance From the Wall
y^+	Normalized Distance From the Wall

List of Symbols – 2

Symbol	Explanation
α	Angle of Attack
β	Prandtl-Glauert Compressibility Correction Factor
γ	Specific Heat Ratio
δ	Boundary Layer Thickness
δ^*	Displacement Thickness
ϵ	Turbulence Eddy Dissioation
ϵ_b	Total Blockage Correction Factor
ϵ_b	Solid Blockage Correction Factor
ϵ_w	Wake Blockage Correction Factor
θ	Momentum Thickness
κ	Empirical Constant Law of the Wall
λ	Wavelength
μ	Dynamic Viscosity
ν	Kinematic Viscosity
ν_T	Eddy Viscosity
ρ	Density
τ	Shear Stress
ψ	Flow Curvature Parameter
ω	Specific Turbulence Dissipation Rate
$\overrightarrow{\omega}$	Vorticity
Ω	Rotational Velocity, RPM
$\overrightarrow{\Omega}$	Vorticity Tensor
∇	Gradient of

List of Abbreviations

Abbreviation	Explanation
AoA	Angle of Attack
c	Chord
cr	Critical
CFD	Computational Fluid Dynamics
CWT	Carousel Wind Tunnel
d	Distance between Inner and Outer Drum
D	Diameter
e	edge of the boundary layer
f	Friction
h	Height of the Tunnel
i	inner
ISO	Isometric
l	Lower
Min	Minimum
o	outer
r	Radial
ref	Reference
R	Radius
RMS	Root Mean Square
RPM	Radians Per Minute
th	Threshold
u	Upper

1

Introduction

The Martian atmosphere has challenging conditions to enable flight on Mars due to its low density and low temperature. Due to the low density, creating sufficient lift is challenging. Flying at this low density results in a low Reynolds number which has a significant effect on the performance. Furthermore, in combination with the low Reynolds number, the Mach number is relatively high because of the lower speed of sound, which can results in shock waves being present. This is due to the CO_2 atmosphere and low temperature. However, since the Reynolds number is low, the exceptional combination of high Mach number - low Reynolds number occurs, of which few data on the performance of airfoils is available. Next to flying on Mars, the low density results in low shear stress due to the wind. However, it is known due to recent satellite imagery that geological processes occur on Mars despite the unfavourable conditions (low density atmosphere). The start of the geological process has been investigated by wind tunnel measurements and analytical solutions. However, their different analytical solutions provide a broad range of results, due to which the exact solution remains uncertain.

The aim of this report is to analyse the design of a carousel wind tunnel, which consists of two concentric drums where the inner drum rotates, to determine its feasibility on performing aerodynamic and aeolian experiments by a computational fluid dynamics (CFD) analysis. Therefore, this report aims to answer the question: **Can a velocity profile be created in a carousel wind tunnel in Martian atmospheric conditions that allows for both the measurement of aerodynamic forces and threshold shear velocities?** To answer this question, the two applications have to be analysed separately. Therefore, to provide an answer to the main research question, the following sub research questions need to be answered:

1. Are we able to create a boundary layer in the carousel wind tunnel that allows us to measure threshold shear velocities?
2. Can inflow and wake flow properties be generated to measure aerodynamic forces on a test object?
   (a) What is the angle and velocity of the inflow?
   (b) Does the flow recover from the wake of a test object?

This report starts with Chapter 2, where the reason behind the necessity is explained by determining the different phenomena of interest occurring on Mars. Both the aerodynamic and aeolian phenomena are explained, and the carousel wind tunnel is introduced. Next, in Chapter 3, the methodology is explained. The different research questions are formulated, and the setup of the CFD analysis is explained. The meshes of the different analysis that will be performed are explained in detail. Furthermore, the boundary & initial conditions are set, and the turbulence model is explained. To ensure a mesh is created of great quality, a mesh convergence analysis is performed. Lastly, before using the results of the CFD analysis, it must be determined if the analysis solves the correct equations (verification), and if the results represent the real physical phenomena (validation). Now that the results are verified and validated, they can be analysed and interpreted, which is done in Chapter 4. Here the results of the 2D and 3D analysis of the carousel wind tunnel, with and without a disturbance, are analysed. The results are discussed both from the aerodynamic and the aeolian point of view. Lastly, in Chapter 5, the analysis on the carousel wind tunnel is concluded.

2

Aeolian & Aerodynamic Phenomena on Mars

Due to the recent rover landings, there is a renewed interest in Mars. With helicopters flying on Mars [6], the goal is to broaden the knowledge related to flying on Mars. Furthermore, with improved satellite images, dune formation and migration are discovered to appear more frequently than first thought. The common parameter between flying and dunes on Mars is the difficulty it has due to the low density. In Section 2.1, the Martian atmospheric properties are discussed and compared to Earth. Secondly, in Section 2.2, existing Martian wind tunnel facilities are compared and discussed. Next, in Section 2.3, the effects of having a low Reynolds number and high Mach number is discussed. Here, important aerodynamic parameters such as the Reynolds number and Mach number, and the related shock waves are explained in detail. The Reynolds number and Mach number are two important parameters when discussing flight on Mars. Due to the low density, the Reynolds number is significantly decreased with respect to Earth. Secondly, due to the low temperature and different gas composition on Mars, the speed of sound is reduced, which results in higher Mach number for the same velocity relative to Earth. However, to create sufficient lift, higher velocities are required to enable flight. Therefore, data on the performance of airfoils at low Reynolds numbers and high Mach numbers must be available. Next, the aeolian process of sand displacement, related to the formation of dunes, is explained in Section 2.4 along with the associated parameters of interest. The testing facility central in this document, the carousel wind tunnel design, is explained in Section 2.5. Lastly, the flow around a cylinder is explained in Section 2.6 because of its usability to compare the flow around the cylinder in the carousel wind tunnel with a regular flow passing a cylinder, for which extensive literature is available.

2.1. Martian Atmospheric Properties

With the flight of the helicopter Ingenuity on Mars, a new and exciting era in (space) flight has began: flying on Mars [6]. However, what makes flying on Mars so different compared to Earth is the substantial difference in atmospheric properties. The most influential parameter of the atmospheric properties is the atmospheric density. The atmospheric density is roughly only 1% of Earth's. Apart from the atmospheric density, there are differences in gravitational acceleration, temperature, pressure, dynamic viscosity, sound velocity, specific heat ratio, gas constant, and atmospheric composition. The air on Mars consists of 95% CO_2, significantly affecting the specific heat ratio and gas constant [65]. The only parameter of the list mentioned that aides the flight on Mars is the reduced gravitational acceleration. The lift has to overcome the weight to enable flight, and thus, a reduced gravitational acceleration results in a reduced weight which lowers the limit of lift necessary to fly. An overview of the parameters that are mentioned with their values on Mars compared to Earth can be seen in Table 2.1. Furthermore, the properties at an altitude of 30km on Earth are also listed to get a grip on the extremely low atmospheric density. The density on Mars is comparable with the density on Earth at this altitude of 30km.

Table 2.1: Average characteristic of Earth's and Mars' atmosphere[12]

Quantity	**Earth (ground)**	**Mars (ground)**	**Earth (30 km)**
Gravitational acceleration [m/s^2]	9.81	3.72	9.78
Density [kg/m^3]	1.225	0.0167	0.0177
Temperature [°C]	15	-63	-46
Pressure [Pa]	10^5	660	1150
Dynamic viscosity [Pa.s]	$1.8 \cdot 10^{-5}$	$1.06 \cdot 10^{-5}$	$1.47 \cdot 10^{-5}$
Sound velocity [m/s]	340	230	300
Specific heat ratio [-]	1.4	1.32	1.4
Gas constant [J/kg/K]	287	188	287

2.2. Existing Martian Wind Tunnel Facilities

Environmental wind tunnels that simulate Martian conditions have been made. Examples of this are the Mars Wind Tunnel at Tohoku University, the Aarhus wind tunnel simulator at Aarhus University and the Mars Surface Wind Tunnel (MARSWIT) facility at NASA Ames [34, 38, 46, 70]. The dimensions of the wind tunnels can be seen in Table 2.2. It can be seen that although the test sections are similar, the length of the tunnel differs significantly. It varies from a few meters up to 13m. This length varies based on the flow velocity that can be reached in the wind tunnel.

Table 2.2: Example of Martian environmental wind tunnels

	Total length [m]	Test section [m]
Mars Wind Tunnel at Tohoku University [34]	3.49	0.1 x 0.15
Aarhus wind tunnel simulator [38, 46]	4.5	1 x 2
MARSWIT facility [38, 70]	13	1.2 x 0.9

The range of total pressure the Mars Wind Tunnel at Tohoku University is between 1 and 60 kPa, both for air and CO_2. The Mach number goes up to 0.74 for air, and 0.84 for CO_2. The range of the Reynolds number is between $2.6 \cdot 10^3$ and $1.1 \cdot 10^5$ for air, and between $4.2 \cdot 10^3$ and $1.3 \cdot 10^5$ for CO_2. The Aarhus wind tunnel simulator has a flow velocity up to 30 m/s and a temperature that can go as low as -170°. The total pressure in the MARSWIT facility can vary between 1 bar and 5.5 millibar. The velocity can go up to 10.5 m/s. It can be seen that the operational range varies significantly, depending on the facility.

From the discussion above, it is clear that the Martian environmental wind tunnels are relatively large in size. This increases the costs of the wind tunnel significantly. When performing measurements in exact Martian conditions, the gravitational acceleration of Mars has to be inserted in the facility somehow. A solution to this would be to place a wind tunnel on board an aircraft such that by performing parabolic flights, different gravitational accelerations can be obtained. However, the large size of the wind tunnel does not allow this. Therefore, a different design of wind tunnel is required.

As mentioned before, conditions on Mars are different compared to Earth. Therefore, to gain more knowledge on different aspects occurring on Mars, wind tunnels in Martian atmospheric conditions are needed. The parameters of interest are the effect of the low Reynolds number in combination with a high Mach number on the performance of an airfoil, which will be explained in the next section, and the threshold shear velocity, which indicates the movements of particles. This will be explained in Section 2.4.

2.3. The Effect of Low Reynolds Number & High Mach Number

Two important parameters relating the flow characteristics to the performance of airfoils are the Reynolds number and the Mach number. The Reynolds number is the ratio of inertial forces to viscous forces. The Reynolds number is defined as:

$$Re = \frac{\rho U L}{\mu} \tag{2.1}$$

where ρ is the atmospheric density, U is the flow velocity, L is a characteristic length, and μ is the dynamic viscosity.

Looking back at Table 2.1, it can be seen that the atmospheric density is extremely low, and the dynamic viscosity is decreased only by a limited amount. Therefore, the Reynolds numbers occurring on Mars for a certain characteristic length and velocity will be low compared to Earth. To provide an example, a closer look is taken at the Ingenuity helicopter. It has a rotational velocity of 2400 RPM and a rotor length of 1.2m, which results in a velocity at the tip of the blade of 301 m/s. With a chord of 0.1m and using the regular atmospheric density on Mars, this results in a Reynolds number of 46 946 [66]. Comparing this with the Reynolds number that would occur on Earth, i.e. 3 485 390, it can be seen that this is a significant decrease.

The second parameter of interest is the Mach number. Why the Mach number is important will be explained in the next section. The Mach number is the ratio of the velocity over a body to the speed of sound. It is defined as:

$$M = \frac{U}{a} \tag{2.2}$$

where U is the velocity over a body, and a is the speed of sound. The speed of sound is dependent on three different parameters: the specific heat ratio (γ), the gas constant (R) and the temperature (T), which can be seen by Equation 2.3.

$$a = \sqrt{\gamma RT} \tag{2.3}$$

Due to the extremely low temperature on Mars (-63°C) and the different gas composition, which results in a lower specific heat ratio and gas constant, the speed of sound on Mars is significantly lower compared to Earth, 230 m/s vs 340 m/s. Therefore, when having a certain velocity, the Mach number will be higher on Mars compared to Earth. Furthermore, due to the low atmospheric density, the velocities required to fly are relatively high which again results in higher Mach numbers. Taking the Ingenuity helicopter as an example, the Mach number at the tip of the blade is 1.3, and thus supersonic on Mars. On the other hand, the Mach number on Earth would be 0.885, and thus remains in the transonic region.

Lowering the Reynolds number results in a decrease in lift coefficient, and results in the non-linearity of the lift coefficient curve. Increasing the Mach number to the transonic regime results in a large increase in drag coefficient. Because of these influences on the performance of an airfoil, the Mach number and Reynolds number are deemed important parameters. The effect of the Reynolds number and Mach number will be further discussed in Subsection 2.3.1 and 2.3.2.

Looking back at Table 2.1, it can be seen that all the parameters are discussed, and that most of them are represented by the Reynolds number or Mach number. The pressure is related to the temperature, density and gas constant by the ideal gas law and thus follows from those parameters.

2.3.1. The Effect of Low Reynolds Number on Airfoil Lift Coefficient

Figure 2.1 shows the influence the Reynolds number has on the lift coefficient of an airfoil. It can be seen that decreasing the Reynolds number results in a non-linear curve, which is contrary to the $C_l - \alpha$ curve of Reynolds numbers at higher Reynolds number. The lift coefficient increases until a certain angle of attack, the stall angle, at which flow separation occurs, which results in a sudden drop of lift. After the stall angle, it can be seen that the lift coefficient increases further. In practice, increasing the angle beyond the stall angle increases drag significantly, and decreases the lift due to the significant lower velocity. Therefore, although the lift coefficient increases, the lift decreases significantly due to the relation with the velocity.

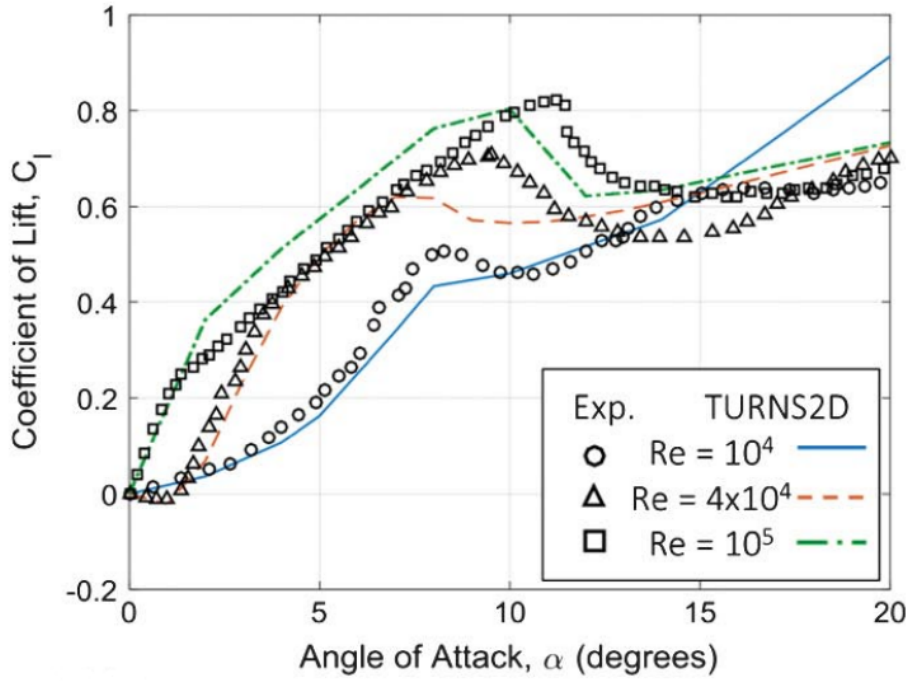

Figure 2.1: Experimental and numerical lift coefficient data for the NACA 0012 airfoil [47, 72]

2.3.2. High Mach Number Effect on Aerodynamic Performance

The second parameter of interest is the Mach number. The Mach number provides an indication where the flow is situated in the compressibility region, i.e., if shockwaves are bound to appear or not.

As mentioned before, the operating range of the Mach number when flying at the same velocity will be higher on Mars compared to Earth. Therefore, it is more likely that the Mach number will be in the transonic range (between 0.8 and 1.2) or higher. When entering this region, shock waves will be present [73]. In Figure 2.2, it can be seen that at a certain free stream Mach number, M_∞, there is a point on the airfoil that has reached sonic conditions, i.e. the Mach number equals one. The free stream Mach number when this happens is called the critical Mach number, M_{cr}. Next, when increasing the free stream Mach number beyond the critical Mach number, a supersonic flow is present over the airfoil, which results in a normal shock wave on the upper surface of the airfoil. When increasing the Mach number further, normal shocks will arise on the upper and lower side of the airfoil. After increasing the Mach number further, the two normal shock waves will come together at the trailing edge of the airfoil [73]. When the free stream Mach number is increased beyond one, there will appear an oblique shock wave, which in contrast to the normal shock wave, has an inclination angle. Apart from the oblique shock wave, a bow shock will be present in front of the leading edge of the airfoil [35].

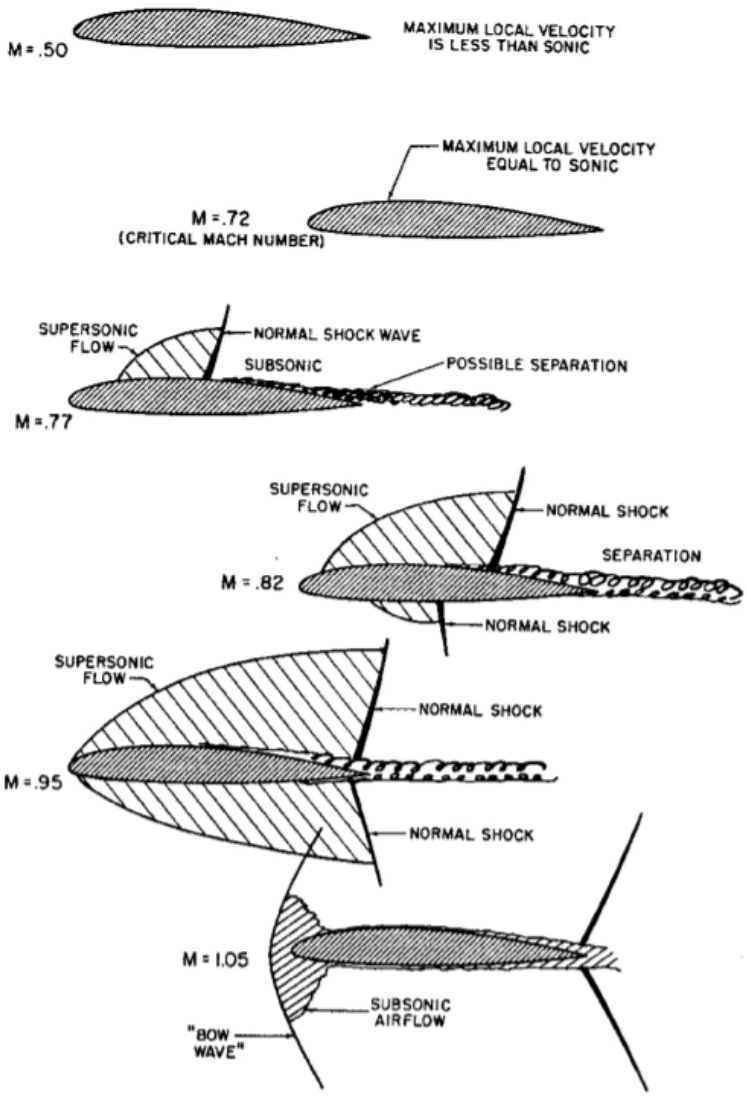

Figure 2.2: Shock wave progression with increasing Mach number [35]

Flying in the transonic region has the disadvantage of a large increase in drag [5]. The drag due to the wave, and due to the energy loss of the shock wave is called wave drag. Furthermore, there is an adverse pressure gradient present due to the increased static pressure after the shock wave, which can result in boundary layer separation [40]. This also increases the drag. The large increase in drag in the transonic region is defined as drag divergence. In Figure 2.3, the increase in drag coefficient in the transonic region can be seen. it has a constant value until the critical Mach number, after which the drag starts to increase. The first increase in drag is gentle, until the drag divergence Mach number is reached, after which the drag increases exponentially due to the separation of the boundary layer [5].

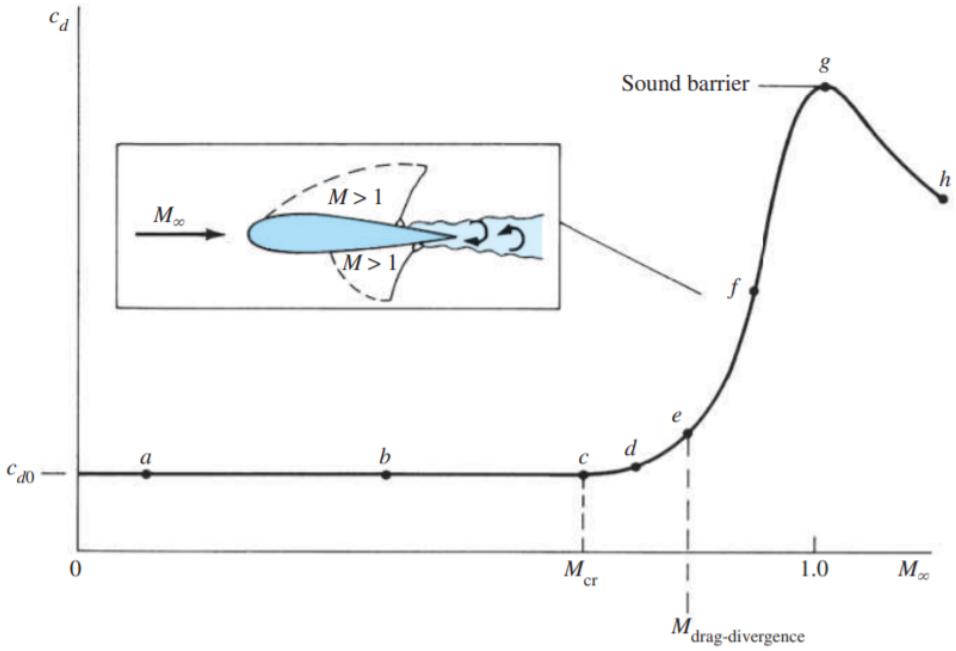

Figure 2.3: Drag coefficient with increasing Mach number [5]

The shock waves causes a reduction in flow velocity, which results in a decreased dynamic pressure. As a result, the total pressure over the airfoil decreases [5].
As a result of the decreased total pressure due to the reduction in flow velocity, the pressure coefficient increases, which can be seen in Equation 2.4 [5].

$$C_p = 1 - \frac{V^2}{V_\infty^2} \tag{2.4}$$

The lift coefficient over the airfoil in the supersonic region is higher due to the supersonic region before the shock. The region after the shock has a higher pressure which results in a lower lift coefficient. However, due to the supersonic region before the shock wave, the overall lift coefficient is increased. Next to the increase in lift coefficient, the drag coefficient is increased as well, which has already been mentioned. The increase in drag is larger compared to the increase in lift. Therefore, the lift-over-drag ratio decreases with increasing Mach number. The increase in lift and drag, and the decrease in lift-to-drag ratio can be seen in Figure 2.4 [16].

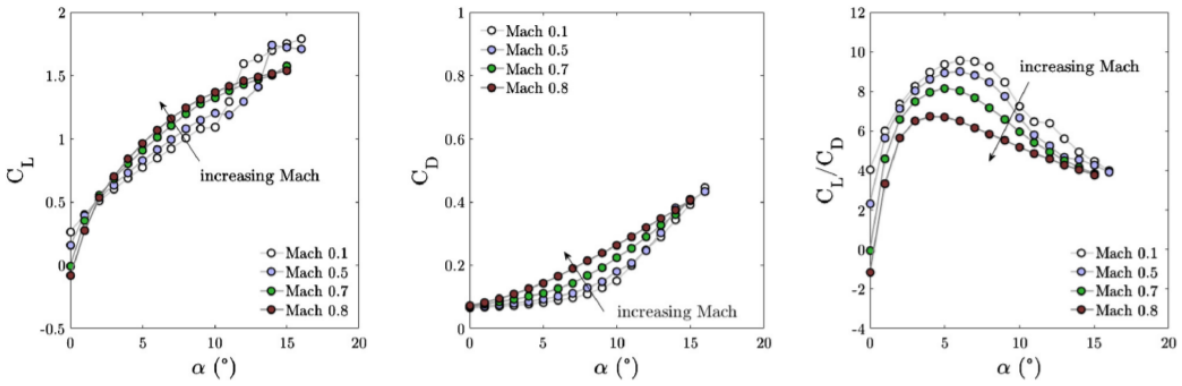

Figure 2.4: Lift and drag coefficient and lift-to-drag ratio for increasing Mach numbers from a 2D Navier-Stokes computation [16]

As mentioned in the introduction of this section, the Mach number operating range of the ingenuity heli-

copter reaches a maximum of 1.3. From the discussion, it can be seen that this Mach number will have an effect on the performance of the airfoil. However, when flying in Martian atmosphere, not only the Mach number is different compared to Earth, the Reynolds number is significantly lower as well. It is therefore crucial that sufficient airfoil data in the low Reynolds number - high Mach number regime is present, which will be discussed in the next section.

2.3.3. Low Reynolds Number - High Mach Number Airfoil Data

The performance of an airfoil is highly influenced by the low Reynolds number and shock waves. The effect the low Reynolds number has on the performance of the airfoil is well understood. Furthermore, the effect of the high Mach number on the performance in Reynolds numbers frequently seen on Earth, and thus higher compared to Mars, is also known in detail. However, in Martian conditions, shock waves in the low Reynolds number regime can be present. Therefore, a closer look is taken at the available airfoil data, which is necessary for the design of aerial vehicles on Mars.

In Figure 2.5, data within the Reynolds number - Mach number range can be seen in grey. In red, it is indicated what data would be necessary to gain insight on the performance of airfoils in the range that would occur on Mars. It is clear that there is only very little overlap between the data available, and the data necessary. Therefore, there remains a knowledge gap on the performance of airfoils withing the Martian Reynolds number and Mach number range.

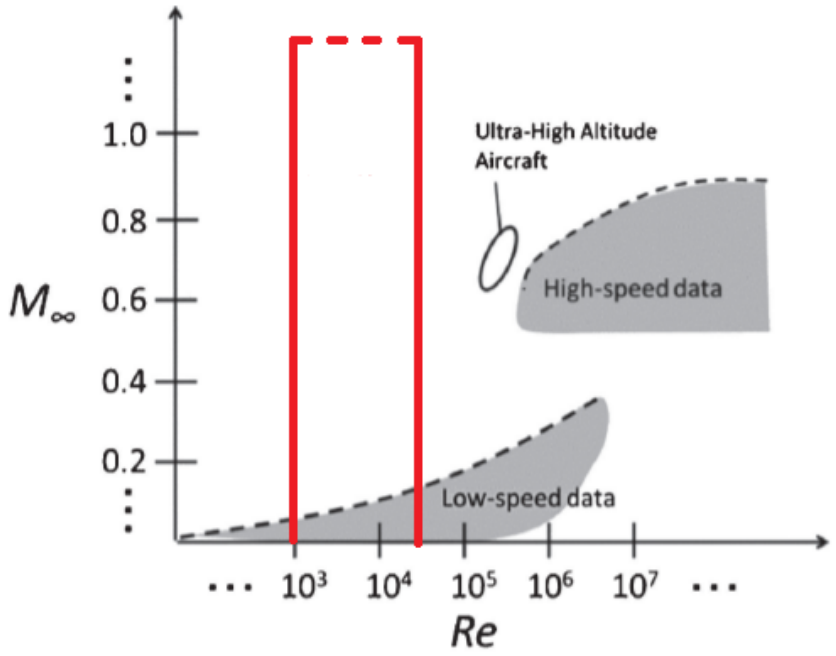

Figure 2.5: Available airfoil data plotted in terms of Re and Mach number [18]

The available Martian wind tunnels, which are extremely costly and have substantial dimensions, in combination with the lack of airfoil data at low Reynolds number - high Mach number range, results in the necessity of a facility that is capable of performing measurements within this range in an affordable manner. However, before going into detail in the design that will be analysed, a completely different phenomenon, that of sediment transport on Mars, is discussed.

2.4. Aeolian Processes on Mars

Aeolian processes are wind driven processes. Sediment is transported or eroded due to wind. On Earth, aeolian processes are very common. However, due to the low density on Mars, aeolian processes where expected to only occur on rare occasions [11]. However, due to the advanced data that has become available from satel-

lites, it is known that dunes migrate centimeters to meters within months to years on Mars [11]. In Figure 2.6[1], the Nili Patera region on Mars can be seen with an example of a sand dune.

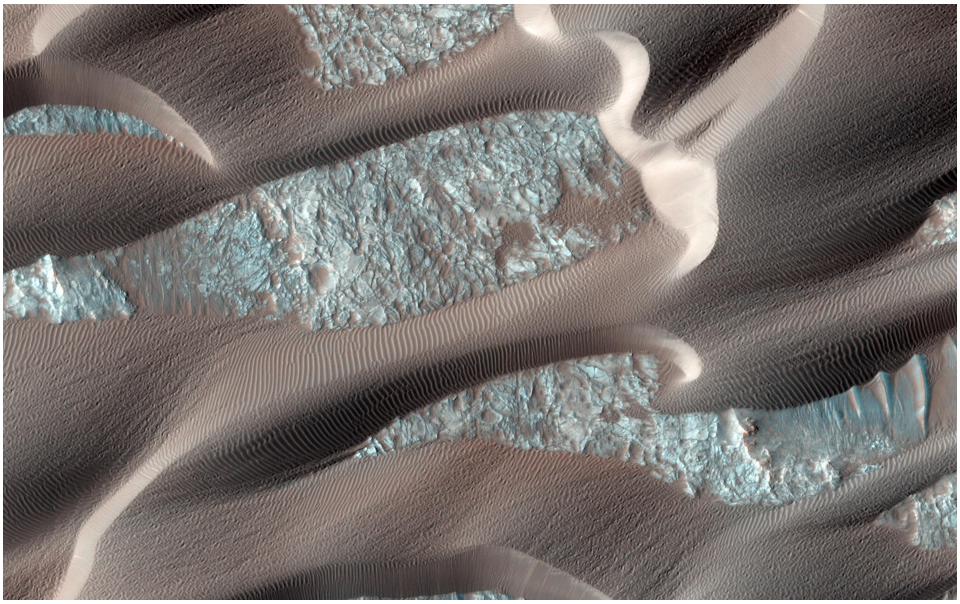

Figure 2.6: Dune field on Mars

2.4.1. Parameters of Interest for Aeolian Processes

On all planets with sufficient atmospheric density, aeolian processes can occur. The shear stress due to the wind is dependent on the atmospheric density. Therefore, this is an important parameter to determine whether or not sediment can be transported. Aeolian process cause for sediment transport which can lead to the formation of sand dunes [11].

Before continuing on the different parameters that influence sediment transport, the difference between sediment entrainment and particle detachment is explained. When a particle is carried aloft (by air), it is called sediment entrainment. On the other hand, when the particle is detached from the surface (by for example rolling, without leaving the surface), it is called particle detachment. Consequently, particle detachment occurs first [23].

Different factors influence the movement of a particle, and whether or not it will move: These factors are:

- Atmosphere
- Particle and surface roughness
- Particle weight/size and shape
- Gravity

First of all, as mentioned before, the atmospheric density has an influence on the stress exerted on the particle by the wind. A denser atmosphere results in a lower shear stress required to move the particle. Secondly, the particle and surface roughness have an influence on the friction. Rough surfaces and particles result in more friction and thus a higher stress required to start movement. Next, the particle weight and size influence the movement. Similar to the particle surface and roughness, the larger the weight and size, the higher the friction between the particle and the surface. Lastly, gravity plays an important role as this affects the weight exerted onto the surface.

The different factors mentioned above have an influence on the shear stress required to move the particles. A different method of looking at the movement of particles is by looking at the threshold shear velocity. This is

[1] https://mars.nasa.gov/resources/7135/dunes-and-ripples-in-nili-patera/?site=msl

the shear velocity required to start the movement of particles, u_{*th}. This is a height independent parameter. There are two different threshold shear velocities: static/fluid and dynamic/impact. The first one refers to the shear stress required for a standstill particle to start moving. The second one is the shear velocity required for a moving particle to sustain its displacement [58]. The dynamic threshold shear velocity is lower compared to the static threshold shear velocity due to the initial velocity of the particle. In this document, when talked about the threshold shear velocity, the static threshold shear velocity is considered.

Lastly, the shear velocity (friction velocity) is different from the threshold shear velocity because this is a scaling parameter which is related to the shear stress by Equation 2.5 [61]. The threshold shear velocity is related in the same way to the shear stress but is an indication on the conditions required for particle movement.

$$\tau = \rho u_*^2 \tag{2.5}$$

where τ is the shear stress and ρ the atmospheric density.

It can be seen that the shear stress is related to the atmospheric density. Relating to Table 2.1, it can be seen that the shear stress (for the same shear velocity) will be significantly lower in Martian conditions. However, the shear stress needed to measure static threshold shear velocity will be equal on Mars and Earth. Therefore, the threshold shear velocity will be significantly higher on Mars compared to Earth. This is an important notice, as this would require higher free stream velocities when measuring the threshold shear velocity.

2.4.2. Static Threshold Shear Velocity

Many different results have been obtained to determine the threshold shear velocity, either analytically or experimentally. Different threshold shear velocities are determined for different particle sizes. A summary of the different results, analytically and experimentally, can be seen in Table 2.3.

Table 2.3: Summary of the predicted and measured threshold shear velocities

	Diameter [mm]	Threshold Velocity [m/s]	Method
de Vet et al [14]	0 - 1.19	0.4 - 1.4	Experimental
Greeley and Iversen [25]	0 - 1	2 - 8	Analytical
Iversen and White [26]	0.1 - 0.5	1.5	Analytical
Shao and Lu [56]	1.5	3.1	Analytical
Merrison et al. [37]	1.5	1.7	Analytical

From the table it can be seen that there is a wide variety in results, for different particle sizes, but also for the same particle size. This gives an indication on the uncertainty of these results due to the significant difference for each case.

From satellite images it is known that dune formation occurs on Mars. The parameter if interest is the static threshold shear velocity. The threshold shear velocity is determined by different researches, which could be seen in Table 2.3. However, it can also be seen that there remains a large uncertainty. Therefore, to limit the wide range of threshold shear velocities, a testing facility capable of recreating the exact Martian conditions would be of aide to narrow down the current uncertainty.

2.5. The Carousel Wind Tunnel Design

In Section 2.2, the existing wind tunnels that can perform in Martian atmospheric conditions are discussed. From this, it can be seen that the available Martian wind tunnels are substantial in size, which results in high manufacturing and operating costs. Furthermore, the wind tunnels only focus on one application. The transition from one application to another would result in a large time and cost investment. Therefore, the design of Greeley et al.[21] is analysed in this document to determine its applicability for both aerodynamic and aeolian measurements. The testing facility that Greeley et al.[21] designed is called the carousel wind tunnel. It will be investigated to determine if suitable conditions can be reached in Martian atmospheric conditions. The carousel wind tunnel design has also been used by Demirci et al.[15] to perform measurements related to the erosion of planetesimals (a solid object that moves through a dense gas and dust in space). A more detailed comparison of the carousel wind tunnel measurements performed by Demerci et al.[15] will be done

in Chapter 4, after the results have been analysed.

A carousel wind tunnel consists of two coaxial drums, as can be seen in Figure 2.7 [21]. By rotating the inner drum, a flow field is created between the two drums. To be able to gather reliable data, the flow field, namely the velocity profile, needs to be determined. From the velocity profile the threshold shear velocity, and the applicability of performing aerodynamic measurements can be determined. This velocity profile gives an indication on the achievable velocities in the wind tunnel and how this is distributed over the domain.

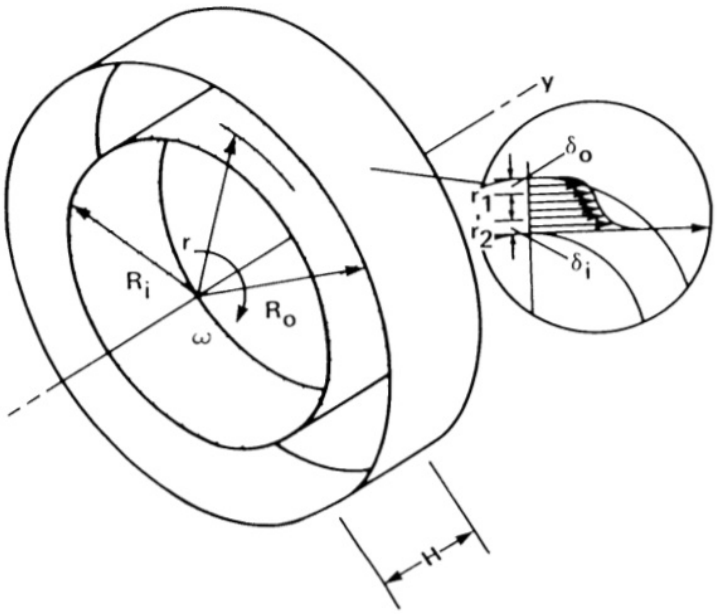

Figure 2.7: Sketch of the composition of the carousel wind tunnel [21]

The first advantage of using a carousel wind tunnel compared to regular environmental wind tunnels is its limited size and simple design. Due to the simple design of two coaxial drums, the (operating) costs can be reduced significantly. Secondly, due to the limited size, the carousel wind tunnel has the opportunity to be brought on board an aircraft and perform measurements in variable gravitational accelerations. The gravitational acceleration can be adjusted by performing parabolic flights. Consequently, the gravitational acceleration of Mars can be simulated to create the exact Martian environment.

A possible disadvantage of the carousel wind tunnel design is the occurrence of secondary flow effects. The carousel wind tunnel is similar to the so-called Taylor-Couette flow. This flow has been analysed extensively, and many data is available. To determine if the carousel wind tunnel would be feasible, a 3D simulation needs to be performed, this will be done in Chapter 4. However, before performing the simulation, the flow characteristics of the carousel wind tunnel, without the goal to use it as any application, should be known.

In the carousel wind tunnel, energy is transferred from the rotating inner drum (mechanical energy) to the flow. The flow gains energy by shear with the inner drum, and from momentum transfer which occurs between fluid layers [42]. Therefore, the flow within the carousel wind tunnel is called a shear-driven flow [9]. Due to the rotation of the inner drum, a centrifugal force is exerted onto the flow. This centrifugal force is the cause of instabilities occurring in the carousel wind tunnel [57, 69]. The centrifugal force is therefore called the unstable driving force [42]. Instabilities due to the centrifugal force occur due to the fact that the centrifugal forces are able to overcome viscous forces [30]. Because the rotating inner drum is causing the instability, the source of the instability can be seen as the adverse pressure gradient at the inner drum, resulting in an adverse gradient of angular momentum [30]. However, since the centrifugal force has to overcome the internal friction between the fluid particles, the rotational velocity has to be sufficiently large. To provide a dimen-

sionless parameter which describes the type of instability, the Taylor number (Ta) is defined by Equation 2.6 [17, 67]. Here the Taylor number is simplified to the equation with only the inner drum rotating.

$$Ta = \frac{\Omega^2 R_1 (R_2 - R_1)^3}{\nu^2} \tag{2.6}$$

The Taylor number represents the ratio of the centrifugal force over the viscous force. When the Taylor number exceeds a certain threshold, called the critical Taylor number (Ta_{cr}), instabilities start to occur. When instabilities occur, they first start to appear in the form of counter-rotating toroidal vortices, called Taylor vortices [48, 62]. When increasing the Taylor number further, the Taylor vortices become unstable and progress to wave-like Taylor vortices. Depending on the Taylor number (and Reynolds number, as they are highly correlated), many different flow phenomena can occur. A part of these phenomena at low Reynolds numbers is summarized by Andereckt, Lius and Swinney [4]. The graph showing the different flow Regimes can be seen in Figure 2.8 [4, 22]. It can be seen that the graph represents flow regimes which cover a rotating inner drum, outer drum, and both. Since the focus of this thesis is on a carousel wind tunnel with rotating inner drum, the main flow phenomena of interest are wavy vortex flow, modulated waves and turbulent Taylor vortices. The analysis will be performed at an inner drum Reynolds number of 1278. Therefore, the phenomena occurring will be modulated waves or turbulent Taylor vortices. However, since this is an estimation of the different regimes, the other flow phenomena and regimes are not neglected and can still occur when performing a simulation.

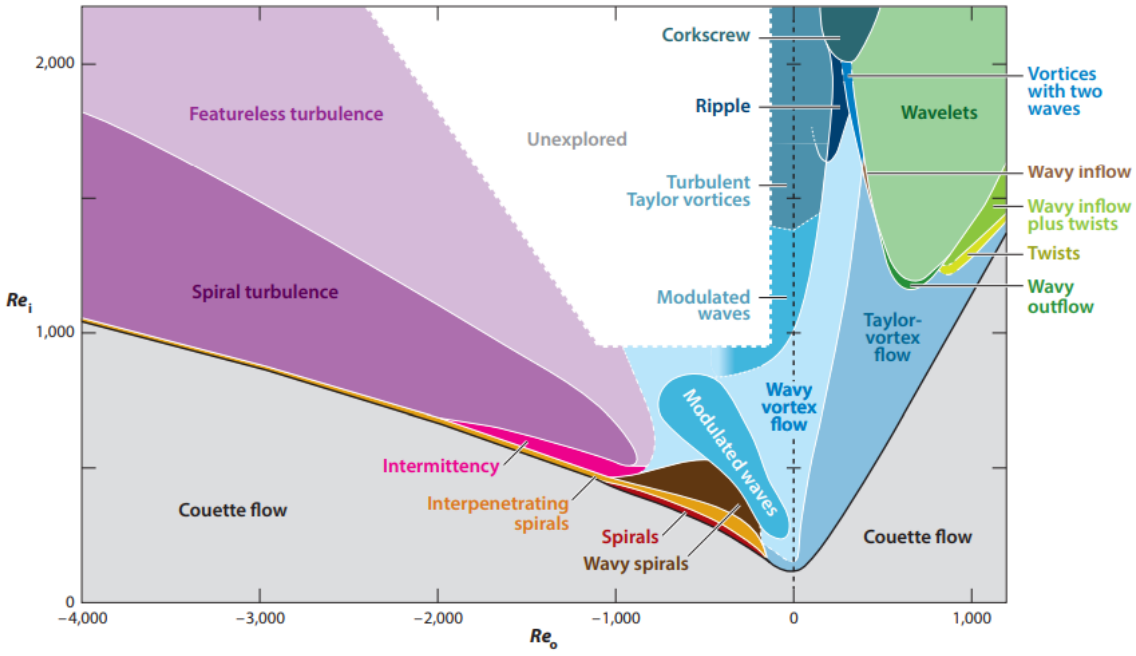

Figure 2.8: Flow phenomena occurring in the carousel wind tunnel at different Reynolds numbers [4, 22]

Due to the fact that the Taylor vortices appear frequently in Taylor-Couette flow, a more in depth analysis of the Taylor vortices is done An example of Taylor vortices can be seen in Figure 2.9 [54]. Here, the toroidal vortices can clearly be seen. The critical wave number of the Taylor vortices is determined and equals 3.12. This implied that the wavelength equals [30]:

$$\lambda_{cr} = \frac{2\pi d}{k_{cr}} \tag{2.7}$$

where d is the distance between the inner and outer drum. Due to the fact that the wave number is close to π, the height and width of a cell of toroidal vortices are almost equal, resulting in a square when looking at the cross-section. Same can be seen in Figure 2.9.

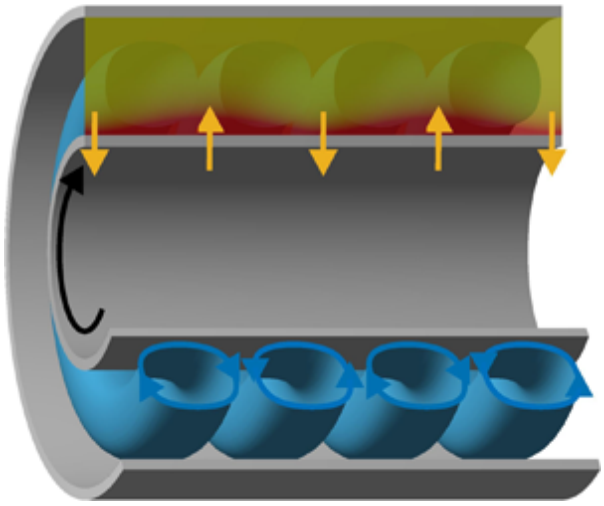

Figure 2.9: Example of Taylor vortices in a Taylor-Couette flow [54]

Now that it is clear that in the carousel wind tunnel, a large variety of flow phenomena can occur, the results from the CFD analysis can be interpreted with sufficient background knowledge.

2.6. Flow Regime of a Cylinder

Using the flow in a carousel wind tunnel to perform measurements has been done sparsely. Therefore, a closer look is taken at flow around a cylinder. This is done to understand the flow in the carousel wind tunnel better, and to be able to thrust the results later on when performing the analysis. By first analysing the behaviour of the flow around the cylinder in more detail to see if it behaves as expected, the results of the simulation can be deemed trustworthy after comparing the results. This can be done because the flow around a cylinder is well established and comparisons with literature can made relatively easily.

Furthermore, by being able to have a testing facility that is capable of providing results of the flow around a cylinder in Martian atmospheric conditions, the carousel wind tunnel can be used as a small scale benchmarking facility, to which different turbulence models can be tested. This would allow for the analysis of the turbulence models which would improve their accuracy and reliability in different flow regimes.

A closer look is taken at the different possibilities of the flow around a cylinder. The different flow regimes can be seen in Figure 2.10 [3, 32]. It is known that the Reynolds number in the carousel wind tunnel is relatively low (the Reynolds number of the carousel wind tunnel that will be investigated is 1278), and thus it is expected that one of the five following options occurs:

1. Regime of unseparated flow, given by extremely low Reynolds numbers, depicted as the first flow regime in Figure 2.10.
2. A fixed pair of Föppl vortices occurring in the wake of the cylinder for Reynolds numbers between 5/15 to 40, depicted as the second flow regime in Figure 2.10.
3. Shedded vortices in the wake of the cylinder, occurring for Reynolds numbers between 40 and 150, depicted as the third flow regime in Figure 2.10.
4. A region of transition between laminar vortex shedding and turbulent vortex shedding in the wake of the cylinder, for Reynolds numbers between 150 and 300.
5. Turbulent vortex shedding in the wake of the cylinder, for Reynolds numbers between 300 and $3 \cdot 10^6$, depicted as the fourth flow regime in Figure 2.10.

When inserting a cylinder in the flow, the Reynolds number will be known and can be compared to the regime as described above.

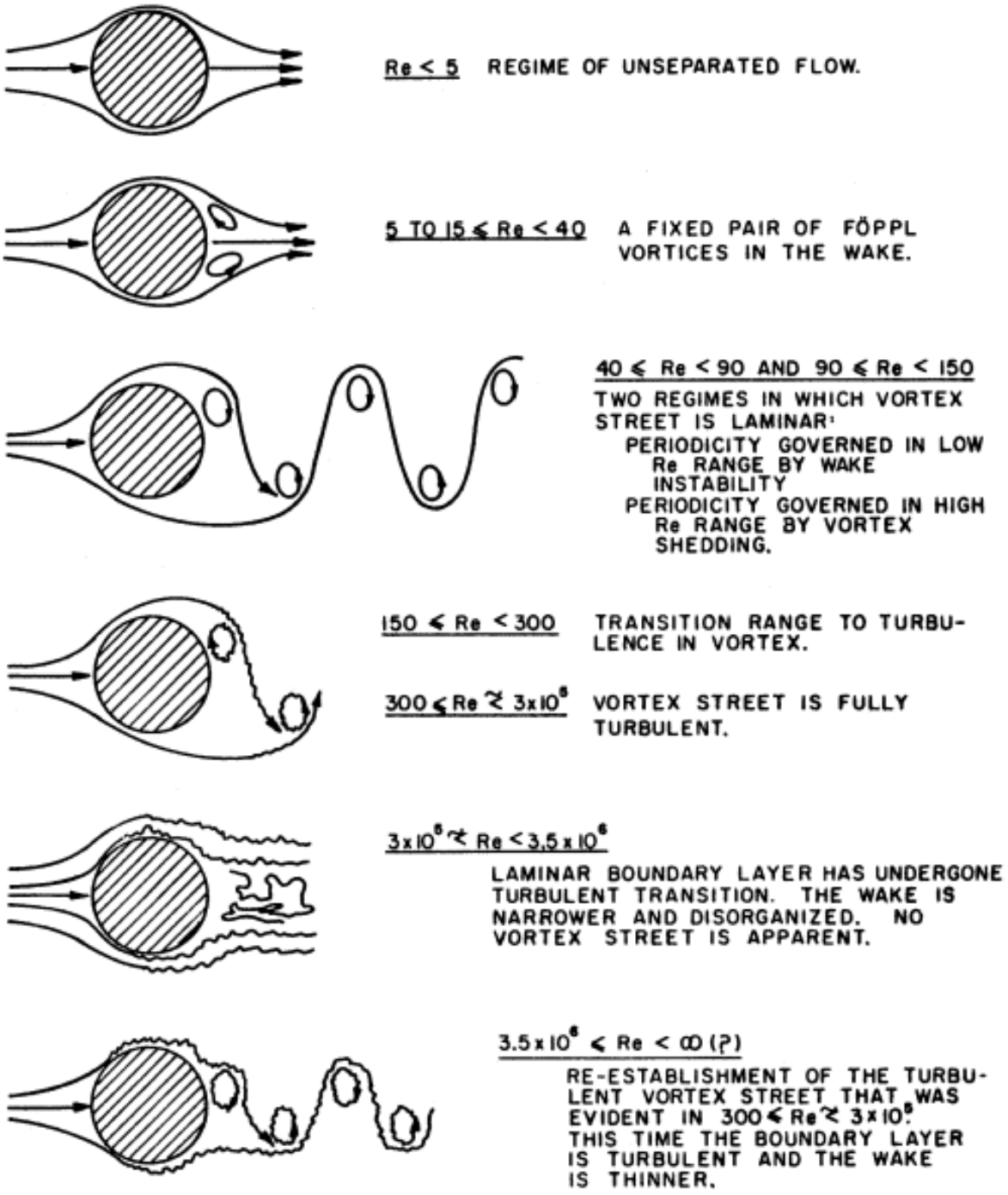

Figure 2.10: Representation of different flow regimes over a cylinder [3, 32]

3

Methodology

The lack of airfoil data discussed in the previous chapter resulted in the necessity of a new type of testing facility. For this, the carousel wind tunnel design was selected. To conclude on the usage of the carousel wind tunnel, research questions are formed, which, when answered, result in a definite answer to whether or not the facility can be used. In this chapter, the researched questions are formulated, and the different steps such as creating a mesh and including boundary conditions that need to be done before an analysis can be performed, are explained. First of all, in Section 3.1, the toplevel and different sublevel research questions are formulated. Secondly, the numerical solver and the discretization is explained in Section 3.2. Next, the mesh and all the steps following up to the mesh for the different analysis that will be performed, are explained in Section 3.3. Section 3.4 covers the boundary and initial conditions in detail. Furthermore, the fluid model used for the analysis is described. In Section 3.5, the k - ω turbulence model and its applicability to low Reynolds number flows is discussed. Before going to verification and validation, the convergence criteria are discussed, and the mesh convergence is shown in Section 3.6. In Section 3.7, verification is done. Here, the obtained numerical data is compared to analytical data. Lastly, in Section 3.8, validation is done by comparing experimental data with the numerical data from the computational fluid dynamics analysis.

3.1. Formulation of Research Questions

From Chapter 2, it was determined that there remains a research gap in both the aerodynamic and the planetary science research field. To fill the knowledge gap, a configuration of a wind tunnel, the so-called carousel wind tunnel design, is proposed as testing facility to measure in Martian atmospheric conditions. This design will be analysed to determine whether or not it is feasible to use as testing facility. For both the aerodynamic and the aeolian experiments, the most crucial part of the carousel wind tunnel is the velocity profile it can achieve. Therefore, to determine the applicability of the carousel wind tunnel, the top level problem, and main research question to answer is:

> Can a velocity profile be created in a carousel wind tunnel in Martian atmospheric conditions that allows for both the measurement of aerodynamic forces and threshold shear velocities?

It can be seen that the main research question involves both the planetary science and aerodynamic experiments. However, based on the knowledge of Chapter 2, the areas of interest to perform measurements in the carousel wind tunnel is very different depending on performing aerodynamic or aeolian experiments. To answer the main research question, two second-level problems, sublevel research questions are created. One sublevel research question for each area of interest. For aeolian experiments, the importance lays in the boundary layer. The boundary layer on Mars needs to be recreated to develop the shear stress necessary to measure the threshold shear velocity. Therefore, the sublevel research question for the aeolian experiments is:

> Are we able to create a boundary layer in the carousel wind tunnel that allows us to measure threshold shear velocities?

On the other hand, when performing aerodynamic measurements, it is important to know both the inflow properties, and the wake flow properties. To enable accurate measurements, the inflow properties need to

be known exactly and are required to be uniform. Furthermore, since the carousel wind tunnel is a closed loop wind tunnel, the wake of the test object is important to not have an influence on the inflow properties. Therefore, the sublevel research question for aerodynamic experiments is:

> Can inflow and wake flow properties be generated to measure aerodynamic forces on a test object?

To answer the sublevel research question, one must answer two separate questions: one based on the inflow characteristics, and one based on the wake flow properties. Therefore, this sublevel research question is divided into two separate questions, which will allow answering the combined sublevel research question.

> What is the angle and velocity of the inflow?

> Does the flow recover from the wake of a test object?

Note that the answer of the test object question, also has an influence on the sublevel research question of the aeolian experiments. To measure the threshold shear velocity, a test bed need to be inserted in the carousel wind tunnel, which potentially could also have a (detrimental) effect on the flow properties.

An overview of the research questions can be found in Figure 3.1. Note the arrow between the sublevel research question of the aeolian experiments, and the wake flow properties, indicating that they are coupled.

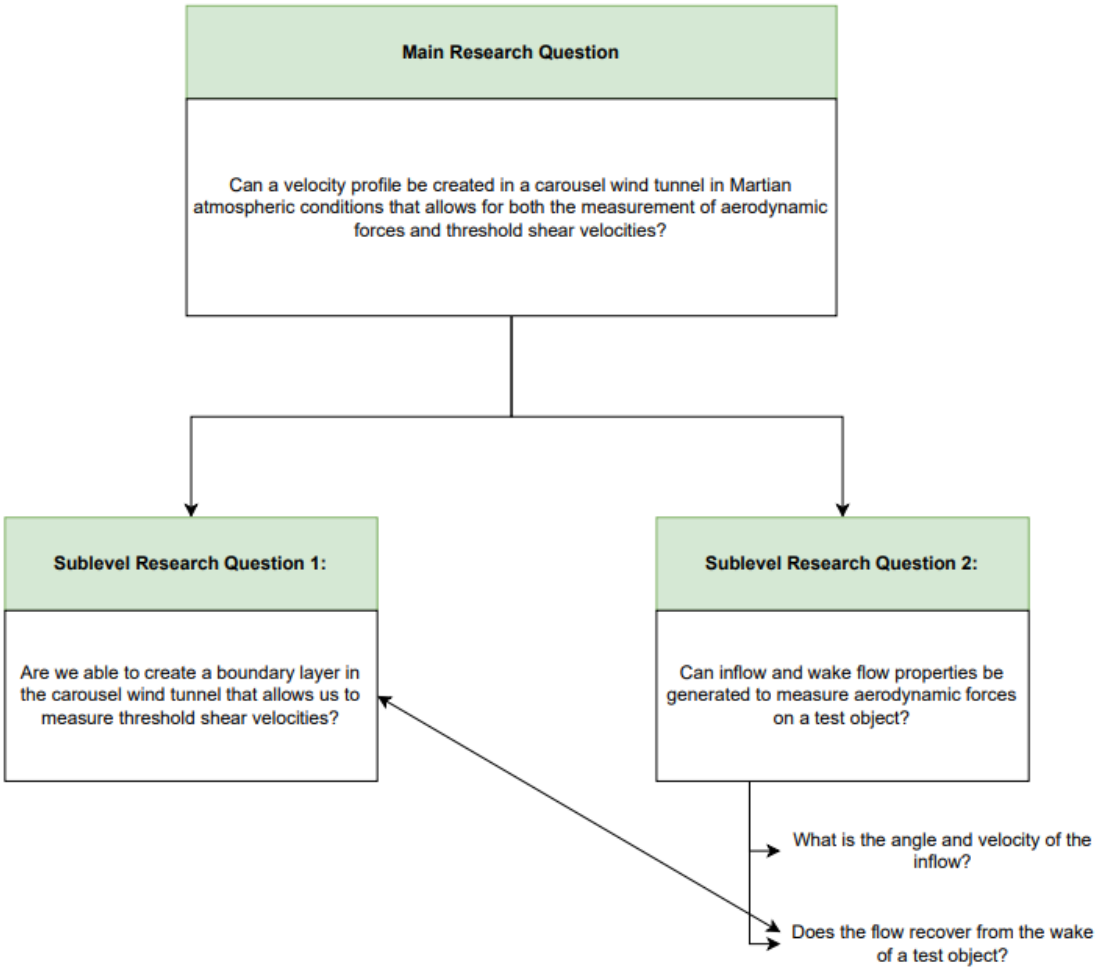

Figure 3.1: Diagram of the research questions

When answering the research questions, the question to whether or not the carousel wind tunnel is applicable for aerodynamic and aeolian experiments in Martian conditions will be answered. The flow inside the carousel wind tunnel in Martian atmospheric conditions provides a scientific answer to the applicability of the carousel wind tunnel.

To answer the research questions, a numerical analysis will be performed. More specifically, a computational fluid dynamics (CFD) analysis. This analysis tool allows for creating a model and analysing the flow properties, while being able to control the atmospheric properties, and the size of the model. However, before being able to perform a simulation, a mesh needs to be created.

3.2. Numerical Solver & Discretization

The Navier-Stokes equation are solved by ANSYS CFX by a numerical approach. A finite volume method is used. This includes first discretizing the domain into different elements, creating a mesh. From these elements, finite volumes are created, for which the quantities mass, momentum and energy are calculated.

In ANSYS CFX, three different discretization schemes can be used: first-order, specified blend factor, and high-order. The discretization can be seen by Equation 3.1.

$$\phi_{\text{ip}} = \phi_{\text{up}} + \beta \nabla \phi \cdot \Delta \vec{r} \tag{3.1}$$

where ϕ_{ip} is the integrated point value, ϕ_{up} is the point value of the upwind node, $\vec{r}$ is the vector connecting the current node with the upwind node, β is the blend factor and $\nabla\phi$ is the control volume gradient.

Depending on the value of the gradient of the control volume and the bled factor, one of the three discretization schemes is used. A first-order scheme is robust, however, it introduces discretization errors that result in lower accuracy results near high spatial gradients. For a specified blend factor, the discretization error can be decreased. However, it can introduce oscillations near regions where the solution varies rapidly. A high-order discretization scheme bounds the blend factor to limit the discretization error and obtain high accuracy results. Therefore, the high-order discretization scheme is used.

3.3. Mesh

When performing a CFD analysis, one of the first and most important steps to do is to create a computational mesh. It is important that the mesh is of excellent quality to be able to correctly assess the results. In order to ensure a qualitative mesh, different checks will be performed when the mesh is created.

When creating a mesh, one has to decide whether to apply a structured or unstructured mesh. A structured mesh has the advantage to allow for the quality of the grid to be controlled by hand. Due to the simple topology and arrangement of cells, the solution algorithm is efficient. Unlike an unstructured grid, where the data has to be accessed through a connectivity matrix, the data of the structured grid can be accessed directly. A disadvantage of a structured grid could be that its quality deteriorates in closer proximity of edges and corners [45]. However, by applying blocking of the mesh, this can be resolved. Therefore, for this computational domain, it is determined to use a structured grid.

3.3.1. Computational Domain

Different CFD analysis will be performed. All the different computational analysis have some dimensions in common. All computational domains consist of two concentric cylinder. The radius of the inner drum equals 0.305m, and the radius of the outer drum equals 0.457m. These dimensions are used for the analysis because experimental data has been performed for a carousel wind tunnel with these exact dimensions [57]. Therefore, by using these dimensions, the results of the CFD analysis can be directly compared to the available experimental data. Furthermore, for the 2D analysis that will be performed, a depth of 0.1m is used. Since this only has one cell in depth of the carousel wind tunnel, to perform a 2D analysis, the depth of the model is irrelevant. For the 3D simulation, a depth of 0.304m will be used. This dimension is not random, but determined to have exactly one pair of Taylor vortices in the carousel wind tunnel. The amount of Taylor vortices is not increased further because this will result in a significant increase in computational effort. Recalling

Equation 2.7, it was determined that to create exactly one pair of Taylor vortices, the depth of the carousel wind tunnel needs to be equal to the distance between the inner and outer drum. Therefore it is chosen that the depth of the model is set to equal:

$$L = 2 \cdot (R_{\text{out}} - R_{\text{in}}) = 2 \cdot (0.457 - 0.305) = 2 \cdot 0.152 = 0.304 m$$

Therefore, if Taylor vortices are present, there should be exactly one pair of vortices in the carousel wind tunnel, which can be checked relatively easily once results have been obtained.

To create the structured mesh, the method of blocking is used. Blocking is used in order to divide different sections of the mesh to allow for refinement of a certain block when necessary. The blocks are converted into an O-grid to be able to create a mesh of high quality. The multiple blocks allows for a high quality mesh, the refinement can be done within these blocks. Blocking of the computational domain will be different for each analysis.

2D - Analysis

The most simple computational domain is the 2D analysis of the complete carousel wind tunnel. To create the O-grid, the domain is split into four equal blocks. This can be seen in Figure 3.2.

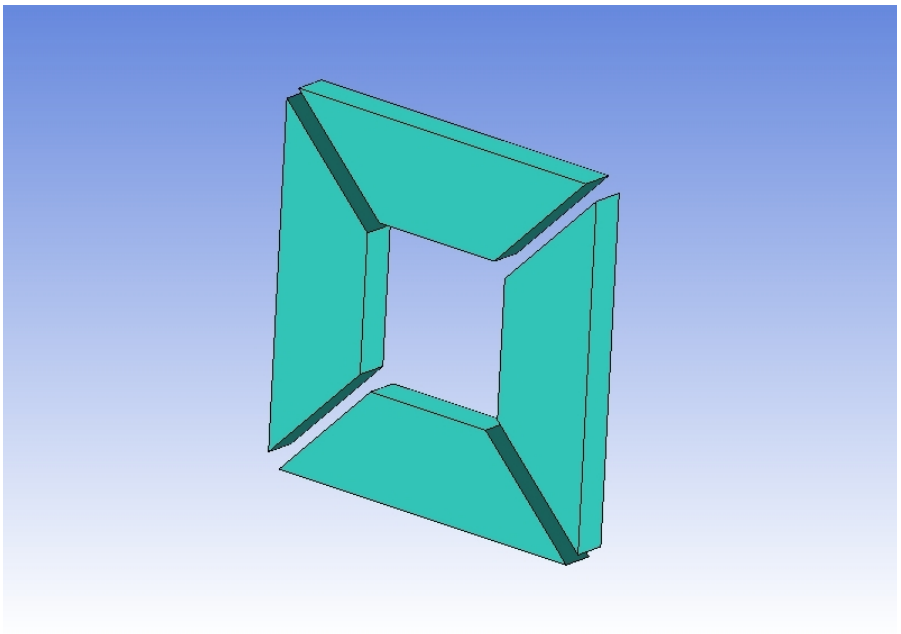

Figure 3.2: Blocking of the computational domain

2D - Quarter Drum Analysis

After realising that the computational domain is equal over the complete carousel wind tunnel for the 2D analysis, only a small part of the carousel wind tunnel is taken, which can be seen in Figure 3.3. By applying the correct boundary conditions, which will be explained in Section 3.4, this analysis gives the exact same results compared to performing an analysis of the complete computational domain. However, the advantage of using only a quarter of the computational domain is that fewer cells are used. This speeds up the computational analysis significantly.

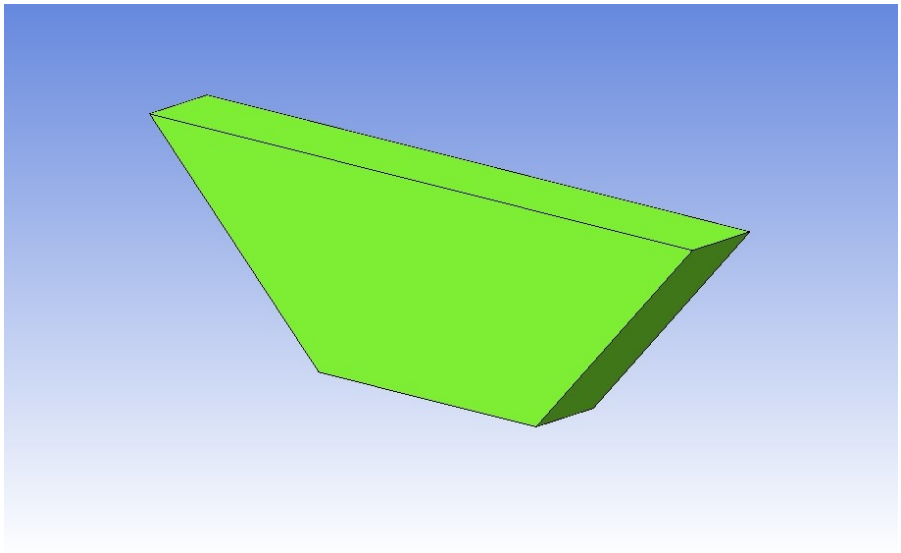

Figure 3.3: Blocking of the computational domain of the quarter mesh

2D Analysis Including Disturbance by Cylinder

The last 2D analysis that will be performed is a 2D analysis with a disturbance caused by a cylinder. A cylinder is placed in the computational domain to analyse the effect it has on the wake flow properties. The computational domain, and the blocking of the domain, can be seen in Figure 3.4. Comparing with the full computational domain without a disturbance, it can be seen that the number of blocks has increased from four to eleven. The difference in blocking comes from blocks one to eight. Blocks one to four have been made to allow more cells close to the cylinder to capture the boundary layer of the cylinder. Blocks five and six are implemented to provide more detail on the interaction between the flow around the cylinder and the boundary layer of the inner and outer drum of the carousel wind tunnel. Block seven allows for more detail on the incoming flow and lastly, block eight ensures sufficient detail on the wake of the cylinder.

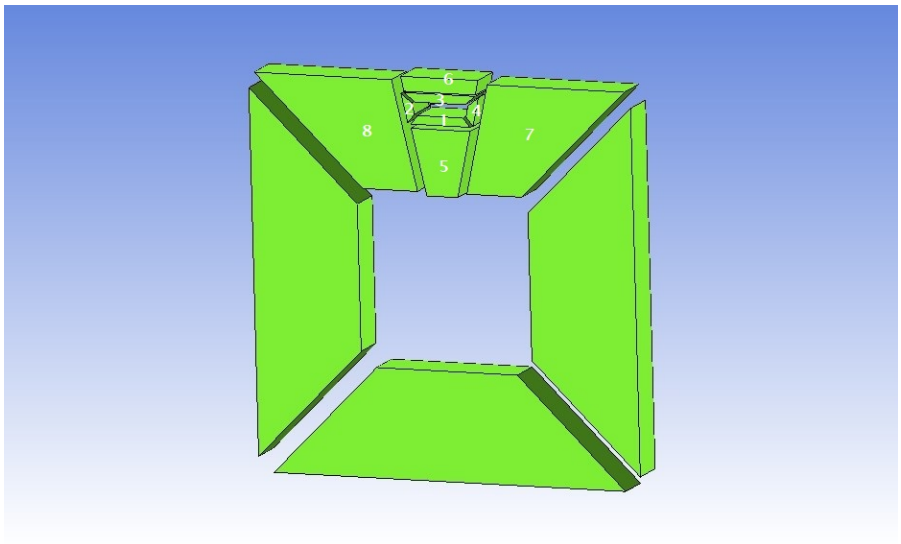

Figure 3.4: Blocking of the computational domain with flow disturbance

Furthermore, it must be noted that the regular 3D analysis, without any disturbance, looks identical to Figure 3.2. The only difference is the depth of the blocks. However, due to this small difference, the computational domain is not visualized again.

3.3.2. Grid Topology and Mesh Specifications

By applying blocks for the computational domain, the mesh can be fine-tuned. To create the mesh, there are three important parts which allow for fine-tuning it. The number of cells on the inner and outer drum, the number of cells in between the inner and outer drum, and the number of cells towards the direction of the tube. Furthermore, the cells can be either uniform distributed or (bi)exponentially. A uniform distribution has the same mesh size for all cells. On the other hand, a (bi)exponential distribution allows to specify in which direction, or both, the mesh size needs to be finer. This is useful when having cells near a wall, or a region with higher velocity gradients.

The mesh generated from the blocking consists of 159 580 cells and is visualized in Figure 3.5. The cells on the inner and outer drum are uniformly divided because there is not a specific part of the drum that is more important than another. The cells in between the inner and outer drum, however, have a biexponential distribution. This means that there are more cells located towards the inner and outer drum. This is because in the boundary layer the uncertainty and error is significantly higher compared to the middle section of the wind tunnel. In order to resolve this, more cells are located at this location. This can be seen in Figure 3.6, and more detailed in Figure 3.7. Lastly, the cells in the directions of the tube either only one cell is present to allow for 2D simulations, or a biexponential distribution is done. The biexponential distribution can be seen in Figure 3.8 and 3.9.

The main differences in the mesh when performing a 3D simulation is the amount of cells in the direction of the depth of the carousel wind tunnel. Instead of having only one cell in depth for the 2D cases, a biexponential distribution is used in the depth of the carousel wind tunnel as well. Since the depth of the model is equal to the gap between the inner and outer drum, the same amount of cells are used in the depth as in the gap of the model. This results in a total amount of cells used of 3 097 116. Comparing this with the 159 580 cells of the full drum and the 39 895 cells of the quarter drum, it can be seen that there is a large increase in amount of cells to allow for a high quality simulation to provide reliable results.

The figures provide only an indication on how the cells are distributed over the computational domain. Therefore, in the next section, the sizes of the cells are compared such that the resolution of the domain is known.

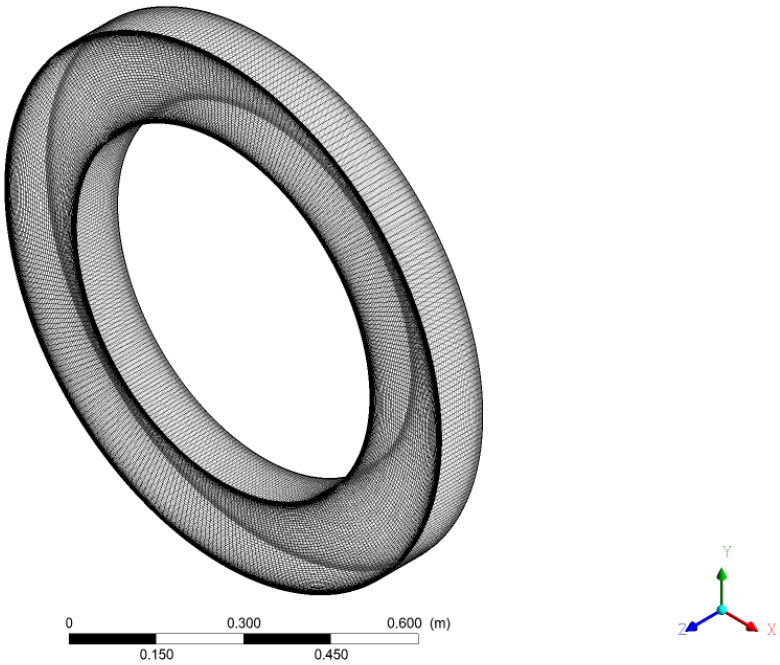

Figure 3.5: Isometric view of the mesh

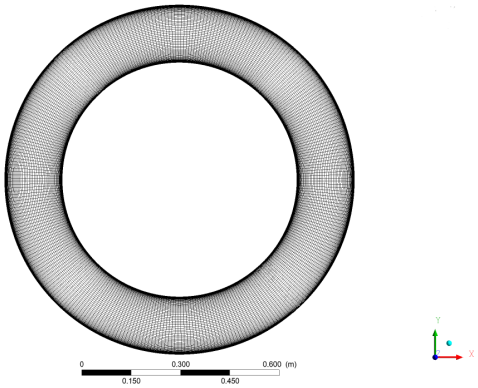

Figure 3.6: Global front view of the mesh

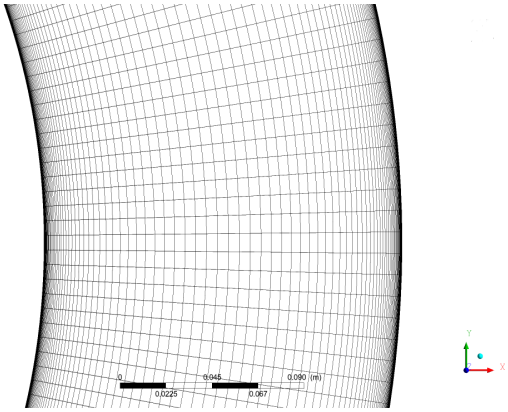

Figure 3.7: Close-up of the mesh

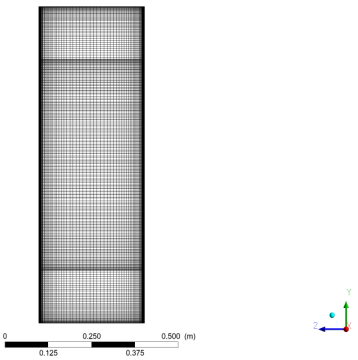

Figure 3.8: Global side view of the mesh in the 3D simulation

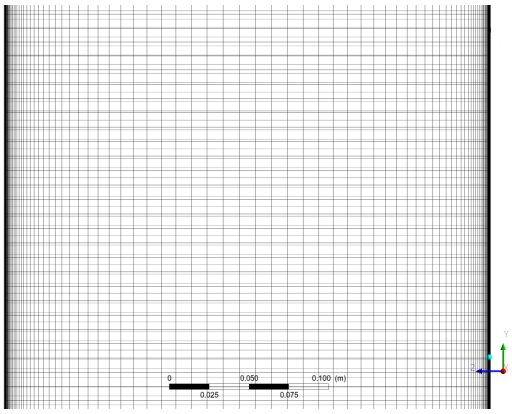

Figure 3.9: Close-up of the side of the mesh in the 3D simulation

Meshing and performing simulations on over the complete circumferential region of the carousel wind tunnel was the first approach. However, after investigation, it was concluded that the flow will be equal over the complete drum when performing 2D simulations. This investigation is shown in Chapter 4. Therefore, only a part of the carousel wind tunnel could be meshed, provided that the boundary conditions are done correctly. The smaller computational domain, of which the blocking can be seen in Figure 3.3, results in a significant reduction of computational time. The mesh of the computational domain of the quarter drum can be seen in Figure 3.10. The same reasoning is followed for the quarter mesh as for the mesh of the complete computational domain and thus more cells are located close to the inner and outer drum. The total amount of cells of the quarter drum is 39 895. This is a significant reduction in cells compared to the complete computational domain (159 580 cells) and will thus reduce the computational effort while not degrading the results of the simulation.

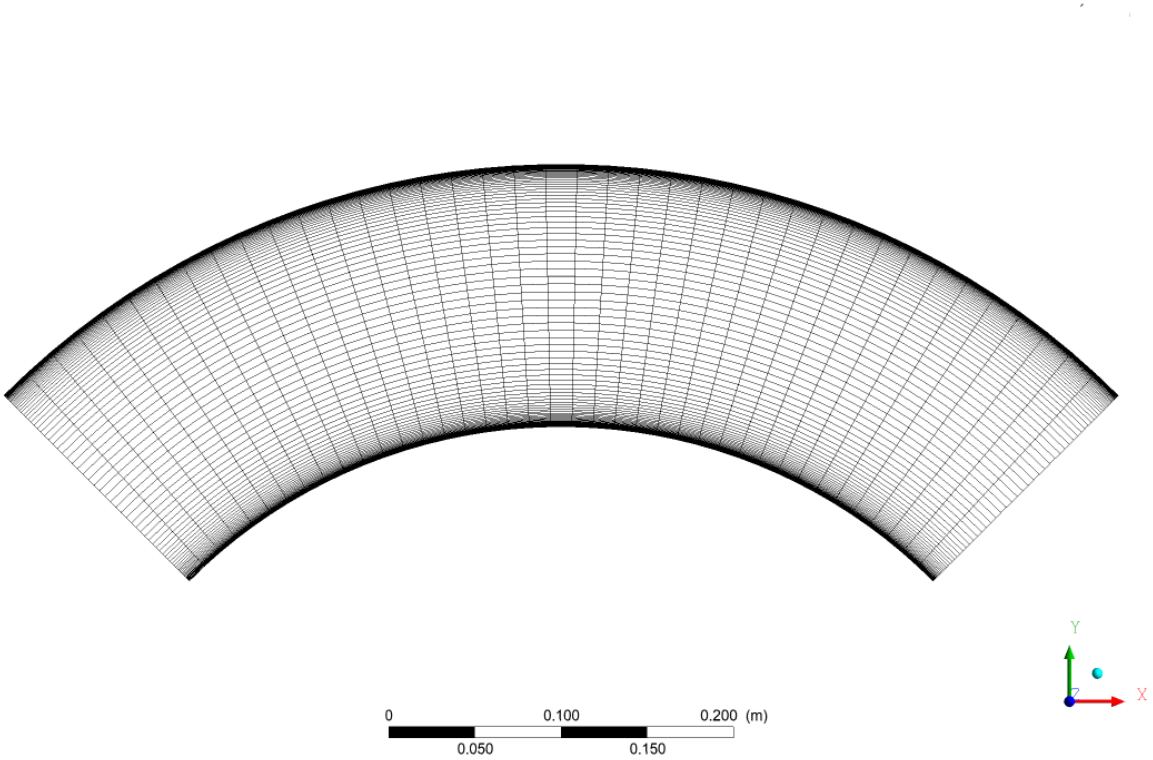

Figure 3.10: Front view of the quarter mesh

The amount of cells does not dictate the quality of the mesh. Therefore, in the next section, the mesh sizes will be discussed to provide reason for the quality of the mesh.

3.3.3. Mesh Quality & Minimum Size

The last step to do when the mesh is created, is to analyse the quality of the mesh. This is done in two ways. First of all, the mesh quality is checked by ANSYS CFX to ensure that there is no entanglement of the cells in the mesh, and to ensure a smooth and orthogonal mesh. For this mesh, the determinant and volume have been checked. Both have to be positive to ensure no cell entanglement is present. The values for the different meshes vary between 0.0525 and 1 for the determinant, and between $2.17 \cdot 10^{-14}$ and $4.79 \cdot 10^{-6}$ for the volume. Therefore, the quality of the mesh is sufficient to perform simulations.

Secondly, the quality of the mesh is determined based on how well resolved the boundary layers are. When only performing a check by ANSYS, all the cells can be structured correctly, however, if the cell size is too large at the walls, the boundary layer will not be resolved. To check this, an often used parameter is the y^+ value with respect to the minimum value of the cell in the domain. y^+ is a normalized value based on the properties at the wall, which will be explained in more detail in Section 3.7. Typically, the y^+ value has to be lower than 1 to resolve the boundary layers [63]. The values of y^+, on both the outer and inner drum, and the minimum size of the cell in the domain for the different generated meshed can be seen in Table 3.1.

Table 3.1: y^+ value and minimum size for the different meshes

	y^+_{inner}	y^+_{outer}	Min. Size
2D Full Drum	0.06	0.04	$5 \cdot 10^{-5}$
2D Quarter Drum	0.06	0.04	$5 \cdot 10^{-5}$
Disturbance by Cylinder	[0.033; 0.065]	[0.021; 0.036]	$4 \cdot 10^{-5}$
3D Full Drum	[0.05; 0.765]	[0; 0.09]	$5 \cdot 10^{-5}$

As can be seen by Table 3.1, all y^+ values are lower than 1. Therefore, it is concluded that the mesh is of sufficient quality to resolve the boundary layer and is of sufficient quality to correctly assess the results provides by the CFD simulation. In Section 3.6, a mesh convergence analysis will be done as a final step to assess if the mesh is of sufficient quality.

3.4. Boundary & Initial Conditions and Fluid Model

When the mesh is made, the next step to do is to create the boundary conditions. Since this model does not have an inlet (and outlet), the boundary conditions determine the flow characteristics. The boundary conditions are set on the inner drum, outer drum and the side surface of the carousel wind tunnel. The boundary conditions applicable to all the different analysis are:

- Inner drum: No-slip wall with rotational velocity (Ω = 169.07 rpm)
- Outer drum: No-slip wall

The boundary condition on the inner and outer drum are no-slip wall conditions. This means that the flow on the surface does not slide over it. Since for the carousel wind tunnel the inner drum rotates, the inner wall was set to have a rotational velocity.

Furthermore, when a 2D analysis is performed, the side surfaces are set to be symmetric due to the 2D flow characteristics that will be analysed. The symmetry on the sides of the model allow for no 3D effects of the sides to be included.

For the quarter drum, an additional boundary condition needs to be set on the front and back surfaces, namely a domain interface. The domain interface on the front and back surfaces have a rotational periodicity included, allowing the quarter drum to be simulated as a complete carousel wind tunnel.

Lastly, when implementing the cylinder, the boundary condition on this surface is set to be a wall with the no-slip condition.

When the boundary conditions are set, the initial conditions can be determined. It is assumed that the air in the carousel wind tunnel is at a standstill and thus all of the components (x, y, and z) of the velocity are set to zero. Furthermore, depending on the analysis, the pressure inside the carousel wind tunnel needs to be adjusted. If a simulation is performed in Earths conditions, the pressure inside the tunnel is assumed to be one atmosphere. However, when the simulation is performed in Martian atmospheric conditions, the pressure is set to 660 Pa. Furthermore, the temperature is set at 210 K [12].

The fluid model has a large influence on the results as this affects the flow characteristics. First of all, the fluid model used for the simulations in Earths atmosphere is air, assuming it is an ideal gas, where the dynamic viscosity is determined by Sutherland's law, which can be seen in Equation 3.2. The properties of air that are set in the fluid model can be seen in Table 3.2. The ideal gas law is not used to determine the viscosity because the accuracy of the ideal gas law drops significantly when going into more extreme conditions (which 660Pa and 210 K are). Miller et al.[39] indicates that the ideal gas law is accurate for normal to high temperatures. Therefore, Sutherland's law is used to calculate the viscosity.

Table 3.2: Properties of air assuming ideal gas

Air		
Elements	Value	Unit
Specific heat capacity	$1.0044 \cdot 10^3$	$J/kg \cdot K$
Molar mass	28.96	g/mol
Temperature	298.15	K

$$\mu = \mu_{\text{ref}} \left(\frac{T}{T_{\text{ref}}} \right)^{1.5} \frac{T_{\text{ref}} + S}{T + S} \tag{3.2}$$

where μ is the dynamic viscosity, μ_{ref} and T_{ref} are reference viscosity and temperature ($1.716 \cdot 10^{-5}$ kg/m·s and 273.15 K, respectively) and S Sutherland's temperature which equals 110.4 K.

Secondly, when the simulation is performed in Martian atmospheric conditions, the fluid model needs to be changed. First of all, the fluid used is changed. Since the atmosphere of Mars consists of 96% CO_2, the fluid in the carousel wind tunnel is set to CO_2 [33].

Furthermore, since the gas composition and atmospheric conditions are changed drastically, the parameters of Sutherland's formula need adjustments as well. The values of the reference viscosity and temperature, and of Sutherland's constant have changed to 9.81710^{-6} kg/m·s, 273 K and 222 K [7].

3.5. Turbulence Model

The last step to do before the simulation can be run is to determine the turbulence model. The turbulence model solves the equations for the steady mean solution of the Navier-Stokes equations. The heat transfer model represents how energy in the form of heat is transferred throughout the flow.

Starting with the turbulence model, in CFX different turbulence models can be chosen. Each turbulence model is different and not all the models can represent the same reality equally well. For example, the k - ϵ model performs well for exterior flows where there is a thin 2D shear layer. However, for a flow with high pressure gradients, the method offers poor predictions. For this flow problem, it is determined that the k - ω model is the most suitable. The k - ω model is a two-equation model. Turbulence is predicted by the two variables k and ω. K and ω are related by Equation 3.3 and 3.4.

$$\omega = 2\frac{1}{C_{\text{d}}}\frac{\epsilon}{k} \tag{3.3}$$

$$\nu_{\text{T}} = \frac{k}{\omega} \tag{3.4}$$

Where C_{d} is a constant, ϵ is the turbulence eddy dissipation (the dissipation of the velocity fluctuations occurs at a rate which is ϵ), k is the turbulence kinetic energy, ω the specific turbulence dissipation rate (the rate at which turbulence kinetic energy is converted into internal thermal energy), and ν_{T} is the eddy viscosity.

Since there are only two additional transport equations, the model offers low computational overhead. Furthermore, it offers accurate results for boundary layer flows and for flows including pressure gradients and separation. The main drawback is that the inflow and free stream boundary conditions highly affect the results. For this reason, the k - ω model is not applicable for external flows [1, 2, 78]. However, since the carousel wind tunnel is a closed environment, this drawback will not affect the results.

Lastly, the applicability of the k-ω model at low Reynolds number must be investigated. The Martian conditions result in low Reynolds number, which affects the flow and will thus also be estimated differently when using a different model. Khuwaranyu and Putivisutisak [28], provide a discussion about the feasibility of the k - ω model in low Reynolds number flows. Although the model can be adapted with a length scale correction (reducing the turbulent wall scale in the near-wall region) to improve the turbulence model further, it is determined that the k - ω model provides reliable results for boundary layer and free-shear flows. Furthermore, Patel and Yoon [49], obtained results for separating flows which where accurate with experimental data. Lastly, Monk and Chadwick [41], performed simulations of a delta wind at low Reynolds numbers and concluded that the k - ω model provides accurate results for different aerodynamic problems, including flows with strong curvature and flow separation. Although from literature the k - ω model is deemed an accurate turbulence model, results of a numerical simulation always have to interpreted with a critical view.

3.6. Convergence Criteria & Mesh Convergence

Before the final results can be discussed, one must be sure that the final results obtained, are indeed the final results. And not, that the flow characteristics in the wind tunnel will still vary. Therefore, before looking at the obtained results, the root mean square (RMS) values of the residuals of the momentum and mass equations of the Navier-Stokes equations are analysed to ensure convergence is obtained. For this problem, the convergence criteria is set at 10^{-6}. Different iterations are performed by CFX to determine the solution. When

the computational time required to reach the convergence criterion is too extensive, a maximum amount of iterations can be set to end the simulation.

Furthermore, to ensure that the amount of cells in the mesh is sufficient, and to analyse the effect of the mesh on the results, an independent mesh study is performed. Three different meshes, 11 184, 25 752 and 39 895 cells, are used to determine the results. To determine the accuracy of the mesh, the obtained results are compared to experimental data from Smith and Townsend [57]. This same data will be used as validation in Section 3.8.

In Figure 3.11, the three different velocity profiles corresponding to the coarse, medium and fine mesh are visualized. A more detailed analysis of the velocity profile will be given in Chapter 4. It can be seen that the results are identical for the part close to the inner drum. When the flow propagates in the middle section, and close to the outer drum, the differences are starting to become visible. The lower the resolution of the mesh, the lower the velocity. A quantification of the results can be seen in Table 3.3. Here the different results at the location $r/R_{out} = 0.948$ are compared. What could be seen in the figure of the velocity profile can now also be seen in the data. The lower the mesh resolution, the larger the underestimation of the velocity.

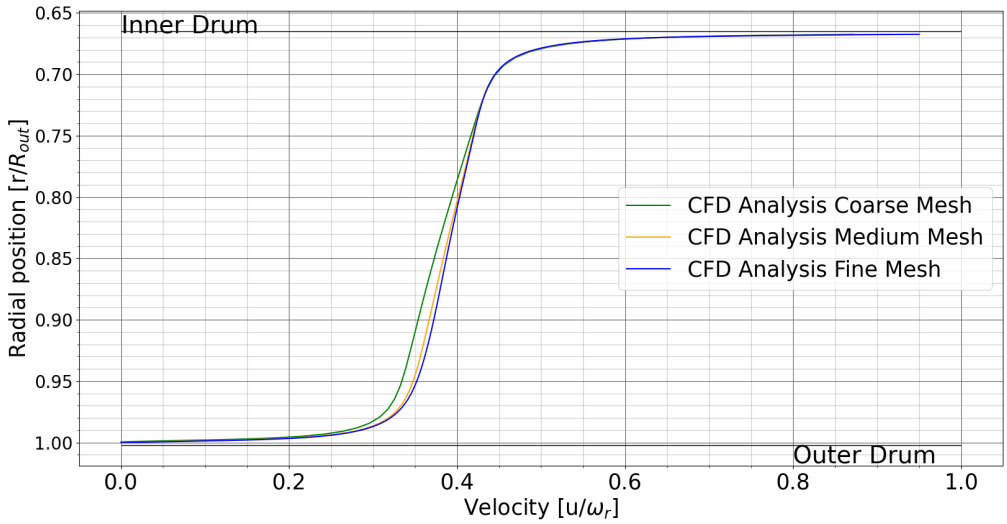

Figure 3.11: Mesh convergence of the velocity profile

Table 3.3: Quantification of the mesh convergence

Coarse	0.3350
Medium	0.3485
Fine	0.3530
Reference data (Smith and Townsend [57])	0.3546

3.7. Verification

In order to build confidence in the CFD analysis results, both verification and validation should be done. With verification, the results are compared to a known solution to verify if the CFD analysis does what it supposed to do, to determine if the analysis solves the right equations and provides the correct solution to the problem. Verification is done for a CFD analysis in Earth atmospheric conditions. Verification and validation of an analysis in Martian atmospheric conditions cannot be done because the analytical equations are semi-empirical and are thus not adapted to Martian conditions, and there does not exist any experimental data to compare the numerical data with to perform validation.

Verification is done by applying the law of the wall. The law of the wall is a normalized velocity profile applied to boundary layers. The law of the wall is divided into two parts, the viscous sublayer & buffer layer, this is the region closest to the wall where viscous forces are highest, and the buffer layer & logarithmic layer. The viscous sublayer & buffer layer and the buffer layer & logarithmic layer are defined by Equation 3.5 and 3.6 [59]. The buffer layer is a zone of overlap between the viscous sublayer and the logarithmic layer.

$$u^+ = y^+ \tag{3.5}$$

$$u^+ = \frac{u}{u_*} = \frac{1}{\kappa}\left(\log y^+ + B\right) \tag{3.6}$$

where u is the velocity, u_* is the shear velocity, y^+ is the distance from the wall normalized by $\frac{y \cdot u_*}{\nu}$, where y is the distance from the wall and ν the kinematic viscosity, and lastly, κ and B are empirical constant which equal 0.39 and 5, respectively. This shear velocity is a parameter related to the shear stress, and is determined based on the velocity gradient. This will be elaborated upon in Chapter 4.

In Figure 3.12, the analytical profile is plotted next to the velocity profile obtained from the CFD analysis. It can be seen that there is a large correlation between the two profiles. The main difference arises in the overlap layer between the viscous sublayer and the logarithmic layer, which is expected. Both at the viscous sublayer and the logarithmic layer, the results show close resemblance between the CFD simulation and the analytical law of the wall method. The shape and gradient of the analytical and numerical data has close resemblance, definitely in the viscous sublayer. At the logarithmic layer, the results show resemblance between y^+ of 10 and 100. Due to the analogy between the two profiles, it is concluded that the CFD analysis is verified.

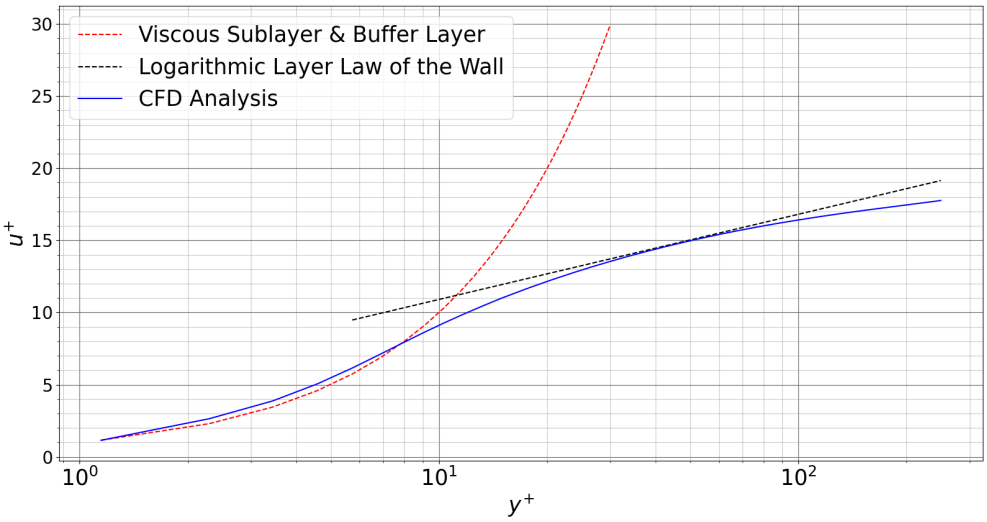

Figure 3.12: Velocity profile of CFD analysis vs analytical profile derived from the law of the wall

3.8. Validation

The last step to do before the results can be deemed correct, is to validate them. Validation is done to determine how closely the results of the analysis are related to the properties in real life. To check how well it represents the real physical phenomena. To verify the analysis, the numerical profile is compared to experimental data obtained from Smith and Townsend [57]. The comparison can be seen in Figure 3.13. It can be noticed that the outer and central region show a high correlation between the two velocity profiles. On the inner drum, the experimental data has a larger velocity gradient compared to the CFD simulation. The difference at the inner drum can be due to 3D effects such as Taylor vortices that occur, as mentioned by Greeley et al.[21]. These 3D effects have additional velocity components which affect the velocity profile compared to a 2D analysis. Since the analysis shows great correlation with the experimental data, it is concluded that the

numerical analysis is validated. Since the 3D effects are an important aspect of the flow in the carousel wind tunnel, this will be investigated in Chapter 4.

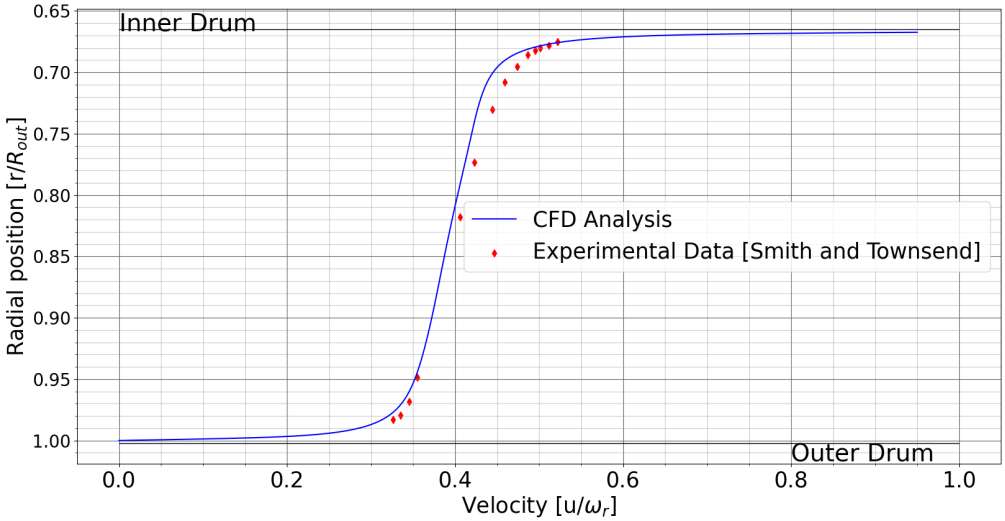

Figure 3.13: Velocity profile of CFD analysis vs experimental data from Smith and Townsend [57]

4

Results & Discussion

To provide an answer on the research questions, the results of the CFD analysis need to be analysed. This will be done in this chapter, while focusing on providing an answer to the different (sublevel) research questions. First of all, the results of the 2D CFD analysis are discussed. This includes the analysis at different Reynolds numbers. The Reynolds number is varied by changing the atmospheric properties between Earth and Mars, and by analysing different configurations of the carousel wind tunnel. This is done in Section 4.1. Secondly, in Section 4.2, the conditions are determined at which the threshold shear velocity in Martian atmospheric conditions can be measured. Next, the effect of placing a disturbance in the form of a cylinder in the flow is analysed in Section 4.3. Here, the flow over the cylinder in the CFD analysis is compared to literature, and the effect of the cylinder on the complete flow field is analysed. Furthermore, due to the cylindrical drums, the effect of curvature on the flow is analysed. By placing the cylinder in the flow, blocking occurs. The velocity is corrected for the effect of blockage, and the different steps are explained. In Section 4.4, the secondary flow effects due to having a 3D simulation are analysed, with an emphasis on Taylor vortices. The required conditions to perform aeolian experiments have been determined as well. Furthermore, the effect of vorticity on the shear velocity in the carousel wind tunnel is analysed. Now that all the CFD results are analysed, a comparison can be made with existing carousel wind tunnel designs. This is done in Section 4.5. Lastly, an overview of the research questions, and their answers, is given in Section 4.6.

4.1. 2D Velocity Profile

Determining the velocity in the carousel wind tunnel allows for concluding on the applicability of the measurements that can be performed. Therefore, emphasis is placed on the velocity in this chapter. From the velocity, it can be determined whether or not the flow properties are favourable to perform aerodynamic measurements. Furthermore, from the velocity at the boundary, the shear velocity is determined. Therefore, the velocity profile also provides an indication if the magnitude reached in the carousel wind tunnel is sufficiently large to measure the threshold shear velocity. First, a CFD analysis is performed in atmospheric conditions of Earth. The CFD analysis is performed at multiple different rotational velocities and conditions. The Reynolds number is therefore used as a non-dimensional parameter. The Reynolds number for a carousel wind tunnel equals:

$$Re = \frac{\rho U d}{\mu} \tag{4.1}$$

where ρ is the atmospheric density, U is the velocity at the inner drum, d is the gap distance, i.e. the distance between the inner and outer drum, and μ is the dynamic viscosity.

With a rotational velocity of 169 RPM, which corresponds to a velocity of 5.4 m/s at the inner drum, and a gap distance of 0.304m, the Reynolds number equals 55 860.

To quantify the velocity profile, a closer look is taken at a cross section of the flow. In Figure 4.1, the velocity profile can be seen. The y-axis is normalized by the radius of the inner drum, where the inner drum is on top,

and outer drum on the bottom, and the velocity is normalized by the rotational velocity of the inner drum, ω_r. In this figure, a region of high velocity close to the inner drum, and the velocity reducing to zero at the outer drum can be seen.

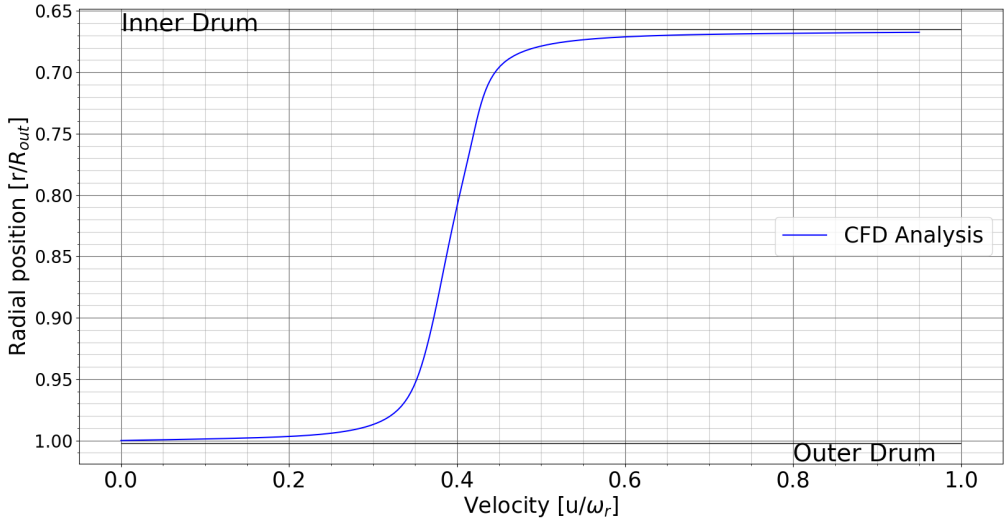

Figure 4.1: 2D velocity profile in the carousel wind tunnel

The boundary layer is calculated based on the vorticity. Vorticity in a flow represents the amount of rotation of which a flow consists. The end of the boundary layer is reached when the vorticity has reached 99% of the vorticity of the flow in the middle section of the carousel wind tunnel. This method had to be applied because there is no free stream on which the boundary layer can be based upon. Vorticity, $\vec{\omega}$, is defined as [29]:

$$\vec{\omega} = \frac{\partial u}{\partial x} - \frac{\partial v}{\partial y} \tag{4.2}$$

However, since the simulation is solely 2D, the second term disappears when looking at the local coordinate system of the flow. The boundary layer will thus be determined based on the gradient of the velocity component in the x-direction.

In Figure 4.2, the result of applying this method can be seen. The red dotted line indicates the boundary layer on the outer drum. A close-up can be seen in Figure 4.3. A closer look is taken at the region near the outer drum because this region is dominated by viscous forces, of which the uncertainty of the results is the highest. From the discussion above, it is known that at the outer drum, the velocity goes to zero due to the boundary condition. Furthermore, it can be seen that there is a high velocity gradient on the outer drum, as expected in the boundary layer.

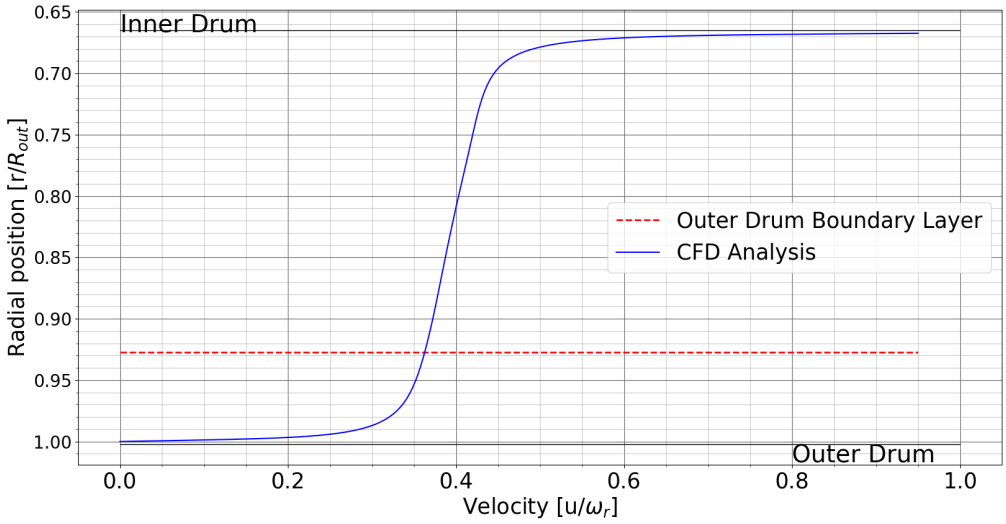

Figure 4.2: 2D velocity profile with boundary layer indication

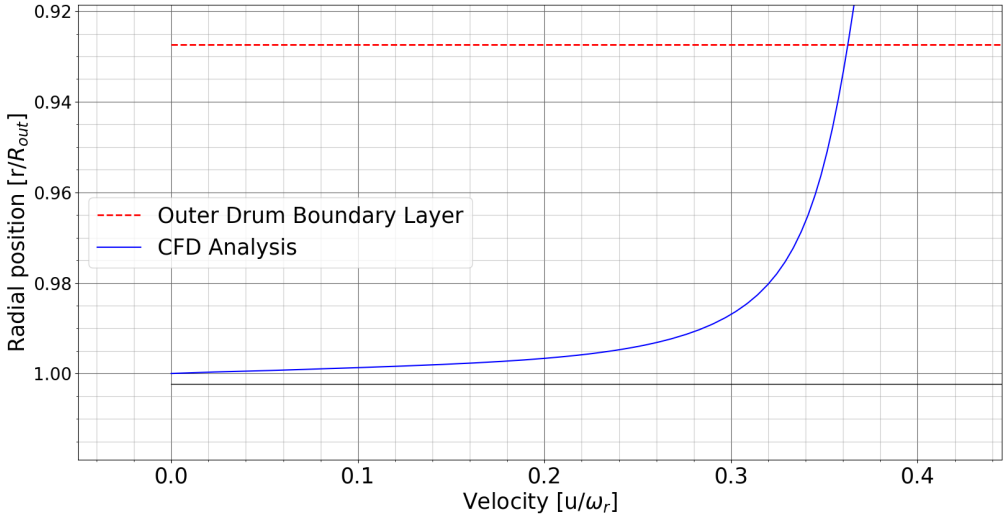

Figure 4.3: Close-up of the outer drum boundary layer

The shape factor of the boundary layer on the outer drum is determined to determine if the flow is laminar or turbulent. To calculate the shape factor, first, the displacement and momentum thickness, δ^* and θ have to be calculated. They are obtained from Equation 4.3 and 4.4.

$$\delta^* = \int_0^\delta \left(1 - \frac{\rho u}{\rho_e u_e}\right) dy \tag{4.3}$$

$$\theta = \int_0^\delta \frac{\rho u}{\rho_e u_e}\left(1 - \frac{u}{u_e}\right) dy \tag{4.4}$$

where δ is the boundary layer thickness, ρ the density, u the velocity and the subscript e corresponds to the edge of the boundary layer. The displacement thickness is a parameter that indicated the effect of the boundary layer on the flow. It indicates the height of the boundary layer, as if there was no velocity gradient. It thus represents the flow as if the fluid is frictionless [36]. This can be more clearly seen in Figure 4.4.

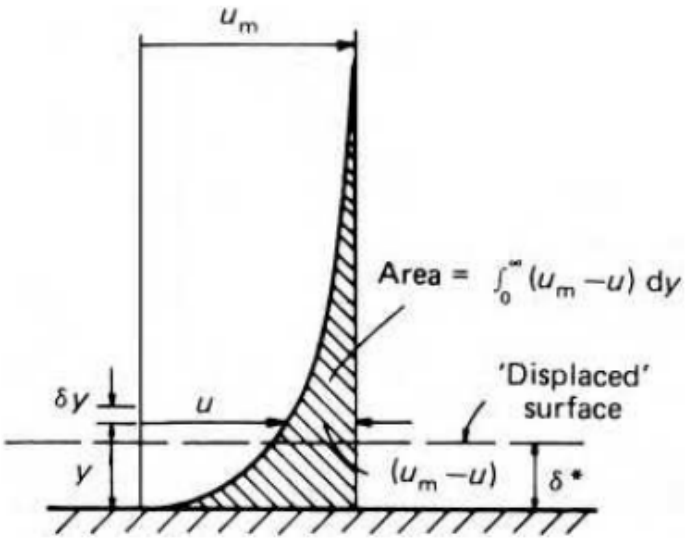

Figure 4.4: Displacement thickness [36]

The momentum thickness, on the other hand, follows the same reasoning as the displacement thickness, but for the momentum of the flow. It indicates the thickness of the flow of which the momentum in the boundary layer is equal to the momentum of a frictionless fluid [43].

When the displacement and momentum thickness are obtained, the shape factor can be determined. This is done by Equation 4.5.

$$H = \frac{\delta^*}{\theta} \tag{4.5}$$

The shape factor is generally and indication of the stability against separation and transition, however it also indicates what type of boundary layer profile there is, laminar or turbulent. The results of the displacement and momentum thickness, and of the shape factor can be seen in Table 4.1. From White [67], the shape factor has to be greater than one, which is the case for this boundary layer. Furthermore, the value of the shape factor indicates the type of boundary layer. For laminar flow, the shape factor varies between 2.0 (stagnation point) to 3.4 (separation point). For turbulent flow, this shape factor is in the range of 1.3 to 2.5. Looking at the value of the shape factor of this boundary layer, 1.495, it is concluded that the boundary layer is turbulent.

Table 4.1: Displacement thickness, momentum thickness and shape factor of the CFD analysis

Displacement thickness, δ^* [mm]	**Momentum thickness, θ [mm]**	**Shape factor, H [-]**
0.3677	0.2459	1.494972

4.1.1. Effect of Reynolds Number on the Velocity Profile

The goal of the carousel wind tunnel is to perform measurements in Martian conditions. Therefore, the conditions are changed to Mars and the velocity profile is analysed. The effect of including Martian atmospheric conditions is that the Reynolds number is lowered significantly. Lowering the Reynolds number lowers the ratio of the inertial component to the viscous component of the flow. From the velocity profile, which can be seen in Figure 4.5 and 4.6, it can be seen that the boundary layer has increased significantly. Which is expected as this indicates a relatively higher shear component of the flow.

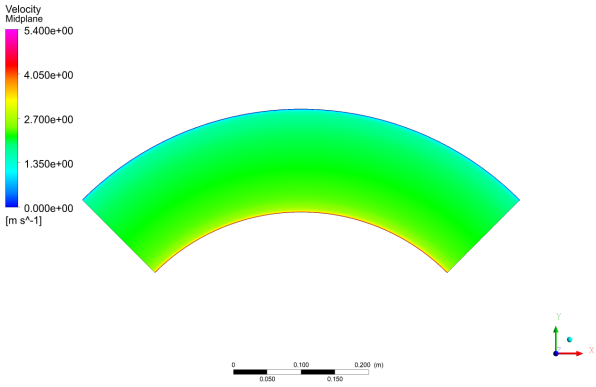

Figure 4.5: Velocity color plot in Earth atmospheric conditions

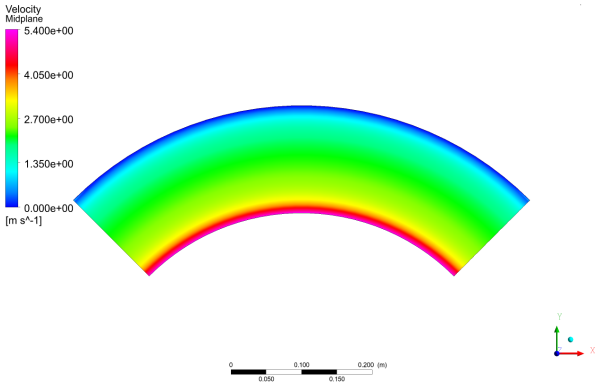

Figure 4.6: Velocity color plot in Martian atmospheric conditions

The boundary layer is increased both on the inner and outer drum. The velocity gradient is lower which results in a thicker boundary layer. This is expected because the relation between the Reynolds number and the boundary layer thickness (δ) is [51]:

$$\delta \propto \frac{1}{\sqrt{Re}} \tag{4.6}$$

And thus, the expected rise in thickness in boundary layer occurred going from high to low Reynolds number.

Furthermore, Schlichting and Gersten [55] indicated that for Re $\longrightarrow \infty$, the velocity profile becomes a straight vertical line. Same happens in the opposite way, a decrease in Reynolds number results in a velocity profile with a lower slope, which can be seen in Figure 4.7 as well.

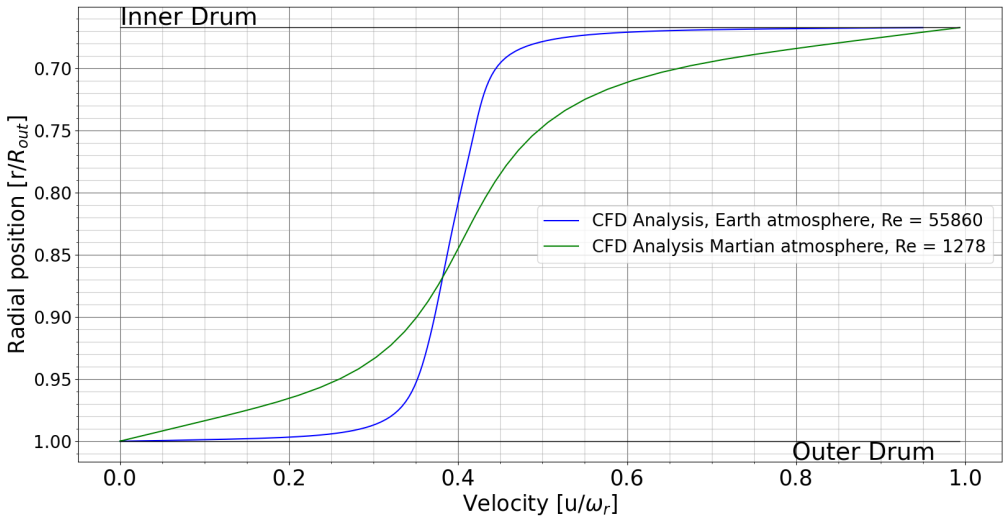

Figure 4.7: Velocity profile in Earth and Martian Atmospheric conditions

It is clear that the Reynolds number has a significant impact on the velocity profile. To analyse the effect of the Reynolds numbers, different configurations are tested, which have a different Reynolds number. The configurations that are analysed are:

1. Earth atmosphere, R_i/R_o = 0.667, Re = 55 860
2. Mars atmosphere, R_i/R_o = 0.667, Re = 1278
3. Mars atmosphere, smaller outer drum, R_i/R_o = 0.801, Re = 639

4. Mars atmosphere, larger outer drum, R_i/R_o = 0.5, Re = 2556
5. Mars atmosphere, higher RPM, R_i/R_o = 0.667, Ω = 338.14 Re = 2556

The resulting five velocity profiles can be seen in Figure 4.8. In the previous analysis, the reduction in Reynolds number resulted in a velocity profile with a lower velocity gradient and higher boundary layer thickness. These phenomena are confirmed with these simulations. The velocity gradient decreases with a reduced Reynolds number, and increased with an increased Reynolds number. Furthermore, it can also be seen that increasing the distance between the drums, reduces the overall flow velocity, and opposite for a decreased distance between drums. Comparing simulation 4 with 5, it can be seen that the same holds over the different dimensions. Simulations 4 and 5 have the same Reynolds number, but different dimensions, and portrait the same velocity profile, but scaled with their dimensions.

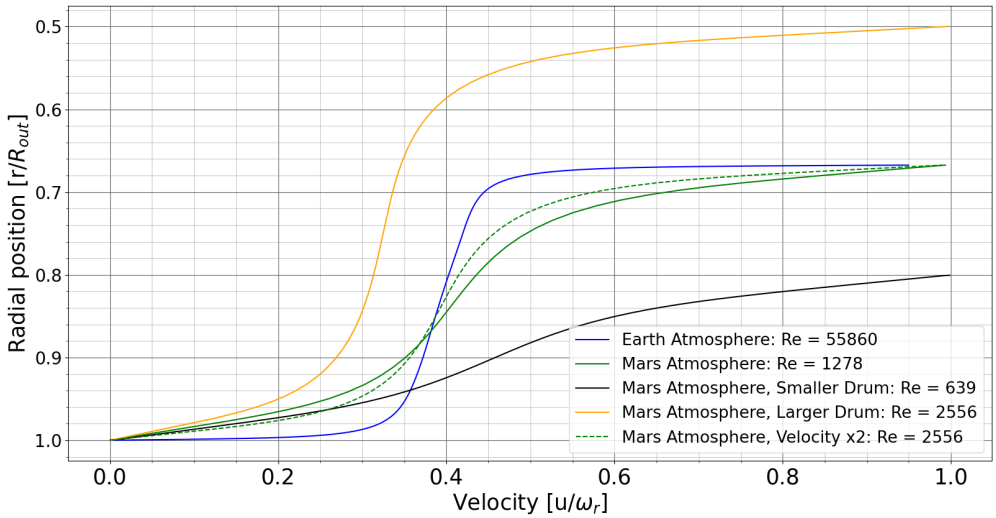

Figure 4.8: Velocity profile at different Reynolds numbers

The CFD analysis at the different Reynolds numbers is done to guide towards an answer if aerodynamic and planetary science experiments would be possible. The analysis on aeolian experiment is done in Section 4.2. When looking at the velocity profile to determine if aerodynamic force measurements, like lift and drag, are possible, the first aspect that can be noticed is that the flow velocity is not constant in the possible test section. The possible test section of the flow would be the central region, where the velocity gradient is low. This causes problems because the measured forces cannot be linked to the correct angle of attack of the flow. However, it can be seen that increasing the distance between the drums, straightens the velocity profile. Furthermore, since the velocity in the central region is reduced, a higher rotational velocity can be used. If a test object where to be placed, the Reynolds number with an increased rotational velocity in the larger carousel wind tunnel would be similar to the carousel wind tunnel with unchanged dimensions and a higher flow velocity in the central region. The conclusion of this 2D analysis on the applicability to perform aerodynamic measurements in the carousel wind tunnel should be kept in mind when discussing the results of a 3D analysis. Solely based on the 2D analysis, no definite answer can be given to the sublevel research question.

4.1.2. Mach Number - Reynolds Number Range

In Chapter 2, it was determined that there is a lack of data for low Reynolds numbers at medium to high Mach numbers. When the Mach number is above 0.2, there is no overlap between the available data, and the data useful to analyse the performance on Mars.

The Mach number will be calculated in the carousel wind tunnel for the middle section, as this would be of interest to perform aerodynamic measurements. From Figure 4.8, it can be seen that increasing the drum size, and thus increasing the Reynolds number, is not beneficial to achieve higher Mach numbers due to the

reduction in flow velocity. Furthermore, decreasing the distance between the inner and outer drum results in an increase of flow velocity, however, the Reynolds number decreases. Therefore, the Mach number is calculated for the regular carousel wind tunnel dimensions.

First of all, the Mach number is calculated for the analysis that has been performed. A rotational velocity of 169 RPM results in a flow velocity in the centre of the carousel wind tunnel of 2.1 m/s. Using a speed of sound of 230 m/s, this results in a Mach number of 0.009. It is thus clear, that the velocity in the carousel wind tunnel will have to be increased significantly to increase the Mach number.

From Demirci et al.[15], the maximum rotational velocity has been achieved while performing measurements. The rotational velocity achieved was 12 000 RPM. This corresponds to a velocity at the inner drum of 383 m/s, and a velocity of 153.31 m/s in the central section of the flow. Again using the speed of sound of 230 m/s, this corresponds to a Mach number of 0.67. At this rotational velocity, the Reynolds number equals 90 746. It can thus be seen that the Mach number is sufficient to gain more insight in the aerodynamics or airfoils at low Reynolds numbers. However, to increase the Mach number to transonic conditions such that shock waves are present, a rotational velocity of 14 400 RPM is necessary. Although this is technically feasible, further research needs to be performed to conclude if accurate measurements can be performed. A problem arising with such high rotational velocities are the vibrations due to the electromotor. The measurements performed by Demirci et al.[15] also show a high uncertainty, which could be due to the vibrations in the carousel wind tunnel. The effect that these vibrations have on the flow in the carousel wind tunnel are unknown, and thus further research must be performed on this topic. Therefore, it is concluded that further research is necessary to conclude on the ability of the carousel wind tunnel to be able to achieve Mach numbers in the transonic range, whilst providing accurate results.

4.2. 2D Conditions for Measuring the Threshold Shear Velocity

To determine the feasibility of performing aeolian experiments in the carousel wind tunnel, the 2D conditions needed to reach the threshold conditions are determined. The important factor in measuring the threshold shear velocity is the outer drum boundary layer. The indication of the boundary layer on the complete velocity profile and a close-up of the velocity profile can be seen in Figure 4.9 and 4.10. Here the conditions are from the regular carousel wind tunnel in Martian atmospheric conditions.

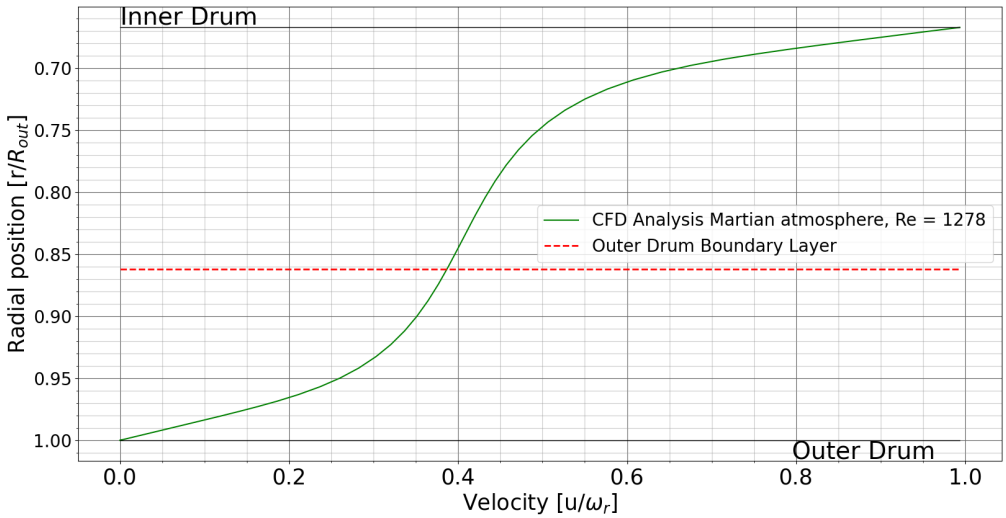

Figure 4.9: Velocity profile in Martian atmospheric conditions with boundary layer indication

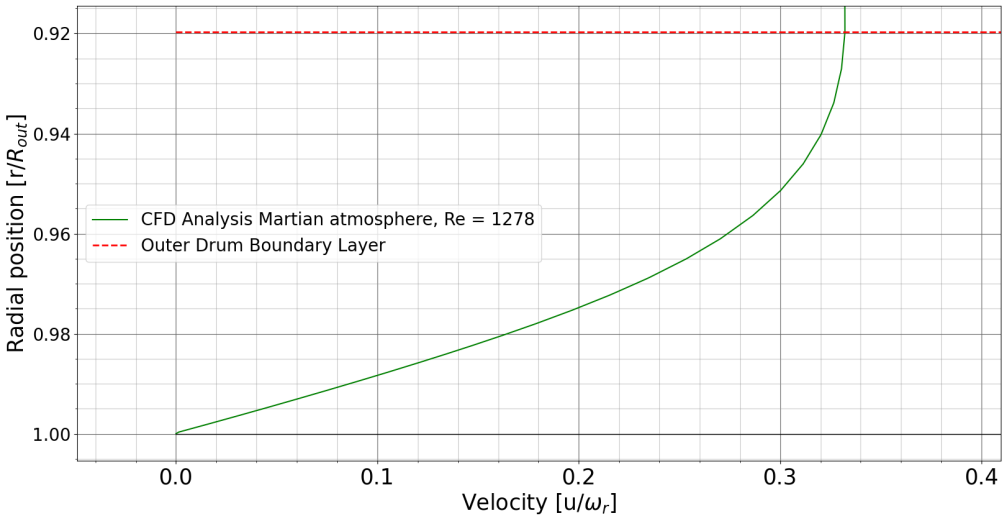

Figure 4.10: Close-up of the outer drum boundary layer in Martian atmospheric conditions

To calculate if the boundary layer is suitable to measure threshold shear velocities, first of all, the friction coefficient needs to be determined. The friction coefficient is calculated by Equation 4.7.

$$C_f = \frac{\mu \frac{\partial u}{\partial x}}{\frac{1}{2}\rho {U_e}^2} \tag{4.7}$$

Where μ is the dynamic viscosity, $\frac{\partial u}{\partial x}$ is the velocity gradient, ρ is the density, and U_e is the velocity at the edge of the boundary layer. All these parameters can be calculated based on the data from the simulations. Once the friction coefficient is determined, the shear velocity can be calculated. This is done by Equation 4.8.

$$u_* = U_e \sqrt{\frac{C_f}{2}} \tag{4.8}$$

Lastly, the shear stress is determined from the shear velocity. This is done because often the shear velocity is used in terms of shear stress and vice versa. Shear stress is used because this variable does not change when changing the atmosphere. The shear stress needed to start particle movement is the same on earth as it is on Mars. The shear stress equals [61]:

$$\tau = \rho u_*^2 \tag{4.9}$$

Implementing Equation 4.8, results in:

$$\tau = \frac{1}{2}\rho U^2 C_f \tag{4.10}$$

Doing this for the regular Martian case, results in the following values:

Table 4.2: Friction coefficient, threshold shear velocity and shear stress in Martian atmospheric conditions for Ω = 169RPM

C_f	$3.349 \cdot 10^{-2}$
u_*	0.2702 m/s
τ	$1.2 \cdot 10^{-3}\ N/m^2$

To determine a relation between the shear velocity that can be achieved by the carousel wind tunnel, a correlation is made between the shear velocity and the rotational velocity. Different simulation have been performed ranging from 84.5 to 5000 RPM. With this, the setting of the carousel wind tunnel can now be determined once the shear velocity is known. Both a linear and 2nd degree correlation have been made to determine what results in the most accurate prediction when extrapolating. The R^2 value of the linear and

polynomial fit equals 0.99389 and 0.9986. Since the polynomial fit provides a higher correlation, the polynomial fit will be used further in this report. The correlation equation equals:

$$y = -4.877 \cdot 10^{-8} x^2 + 1.142 \cdot 10^{-3} x + 0.05895$$

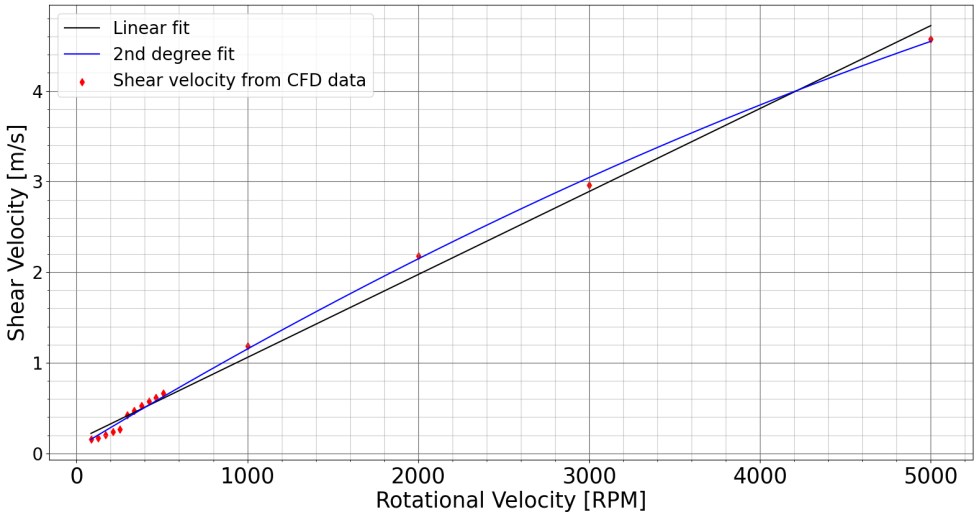

Figure 4.11: Linear and second degree regression Fit for shear velocity by rotational velocity

And thus the question remains, what is an approximate value of the shear velocity? This can be answered by looking at Figure 4.12 [14]. From this figure, the shear stress needed is determined and equals 0.2 N/m^2. Now that the shear stress is known, by calculating backward using Equation 4.9, the shear velocity can be determined and equals 3.4816 m/s. Using this value to calculate the rotational velocity needed, results in a rotational velocity of 3530 RPM, for this particular configuration of the carousel wind tunnel.

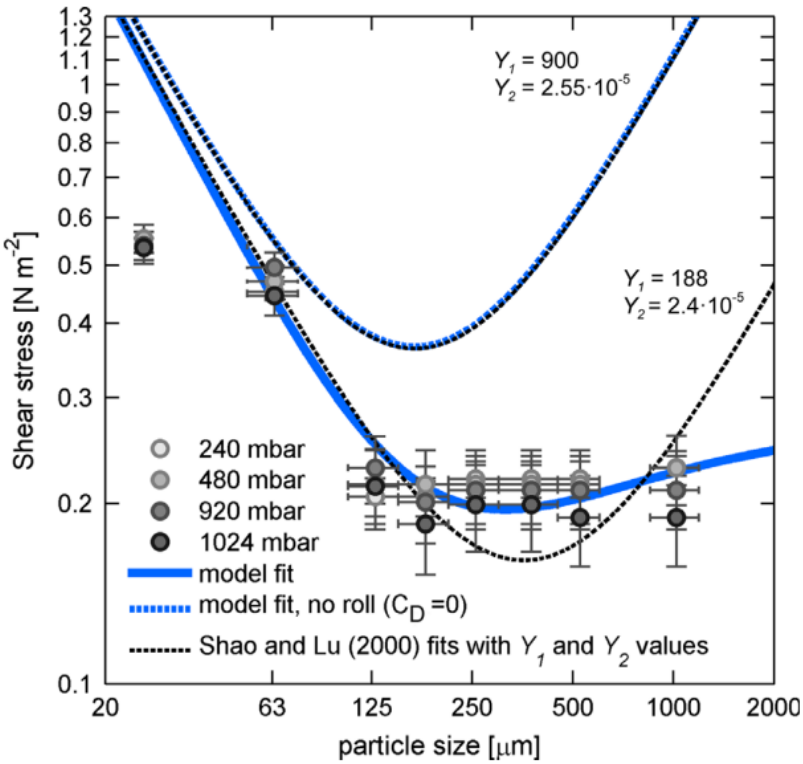

Figure 4.12: Shear stress vs particle size [14]

The next step to determine the feasibility of testing the threshold shear velocity in the carousel wind tunnel, is to perform a simulation where a test bench is included. This test bench is not seen as a full flow disturbance, which will be discussed in Section 4.3. The setup of the simulation can be seen in Figure 4.13. Only a small part, located between the two points, is cut out of the circular outer drum and made straight, such that sand particles could potentially be placed on this flat plate. To give an indication on dimensions, the straight part has a length of 4 cm.

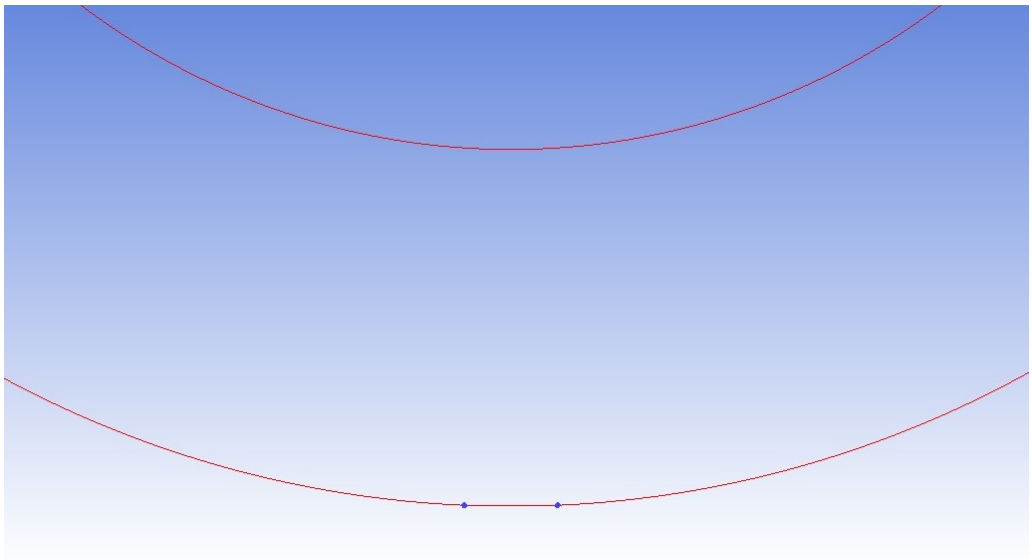

Figure 4.13: Setup test bench simulation

Now, a closer look is taken at the velocity profile over the test bench, to see if and how the velocity profile is altered. The velocity profile, with and without the test bench can be seen in Figure 4.14. It can be seen that the inclusion of the flat plate on the outside of the carousel wind tunnel only marginally affects the velocity profile. It results in a small difference in the velocity profile close to the central region. However, the shear velocity is dependent on the velocity gradient at the wall of the outer drum and on the boundary layer thickness. The influence on the velocity profile is negligible, as can be seen in Figure 4.14. Therefore, the inclusion of the flat plate does not affect the accuracy when measuring the shear velocity.

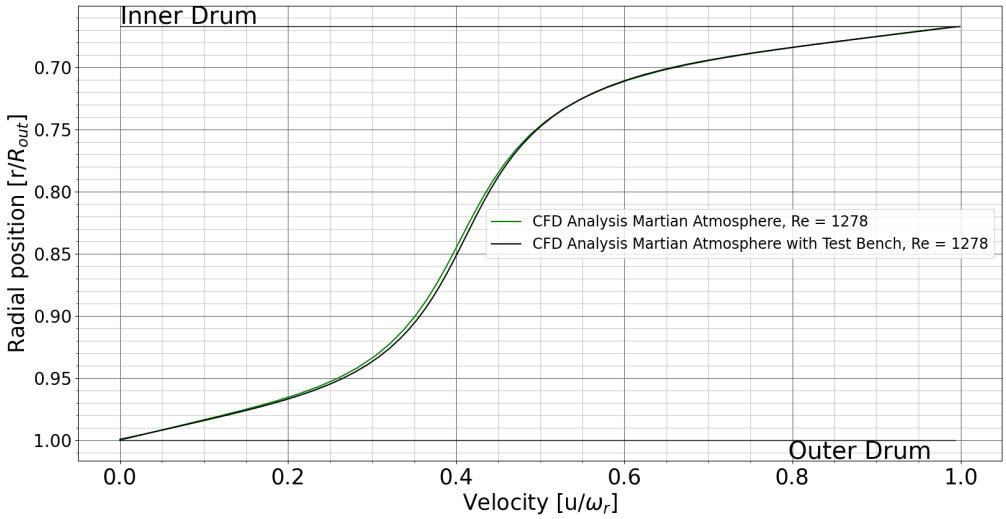

Figure 4.14: Velocity profile with and without the test bench

4.3. Effect of the Disturbance by a Cylinder on the Flow Properties

To perform measurements of aerodynamic forces in the carousel wind tunnel, a test object needs to be placed inside. By placing an object inside, the flow is disturbed and the velocity profile is altered. In order to perform accurate measurements, the alteration of the velocity profile needs to be known when the flow returns to the test object. To analyse the recovery of the velocity profile, a CFD analysis is performed with a test object. The chosen object is a cylinder with radius 1cm. The small cylinder is chosen for several reasons. First of all, the flow around a cylinder is well established. The different flow properties and how the flow reacts are well known in literature. Therefore, before analysing the effect of the velocity profile, the flow around the cylinder can be observed to verify that the flow behaves in a way that is expected. Secondly, a small cylinder of radius 1cm is chosen to prevent the cylinder to be too close to the walls. When then the cylinder would be placed close to the walls, the velocity gradients are large and the interpretation of the results get more complex.

To predict which flow phenomena should occur, the Reynolds number of the cylinder must be determined. To do this, the following equation is used:

$$Re = \frac{\rho \overline{U} D}{\mu} \tag{4.11}$$

Comparing this with Equation 2.1, some alterations have been made. First of all, the relative length of the Reynolds numbers, previously the gap distance, is now the diameter of the cylinder. Secondly, the flow velocity is depicted as the average flow velocity over the height of the cylinder. It is known from the previous analysis that the flow velocity is not uniform in the carousel wind tunnel, and thus, the average velocity is taken.

Two different simulations are run to let two different flow phenomena occur. First of all, the simulation is run at a Reynolds number of 36.9 (corresponding to a rotational velocity of 169.07 RPM), and secondly, at a

Reynolds number of 144. According to Figure 2.10, two flow phenomena should occur: Föpple vortices and vortex shedding.

4.3.1. Föppl Vortices

A closer look is taken at the result of the CFD simulation with regards to the Föpple vortices occurring. This is done by looking at the velocity and streamlines in Figure 4.15. From the velocity contour plot, it can be seen that behind the cylinder, there is a region of backflow indicated by the yellow and light green area. Here, the flow is directed opposite of the main flow, indicating the presence of vortices. With a Reynolds number of 36.9, it is expected that these vortices occur in the form of Föpple vortices. The Föpple vortices are confirmed when looking at the streamlines. They show a clear presence of two vortices in the wake of the cylinder.

The presence of the Föpple vortices proves that the flow in the carousel wind tunnel provides comparable aerodynamic phenomena. It was discussed in Chapter 2 that the carousel wind tunnel could be used as a benchmark to further improve turbulence models in Martian conditions. By experiencing Föpple vortices, which is a known phenomena in Earth conditions as well, the turbulence models can be compared to experimental data of the cylinder in the carousel wind tunnel to further improve turbulence models.

In Figure 4.15, it can be seen that the outer velocity contour is asymmetrical. This can be due to the curvature of the carousel wind tunnel, or due to the non-uniform inflow velocity. This will be further discussed in Subsection 4.3.3.

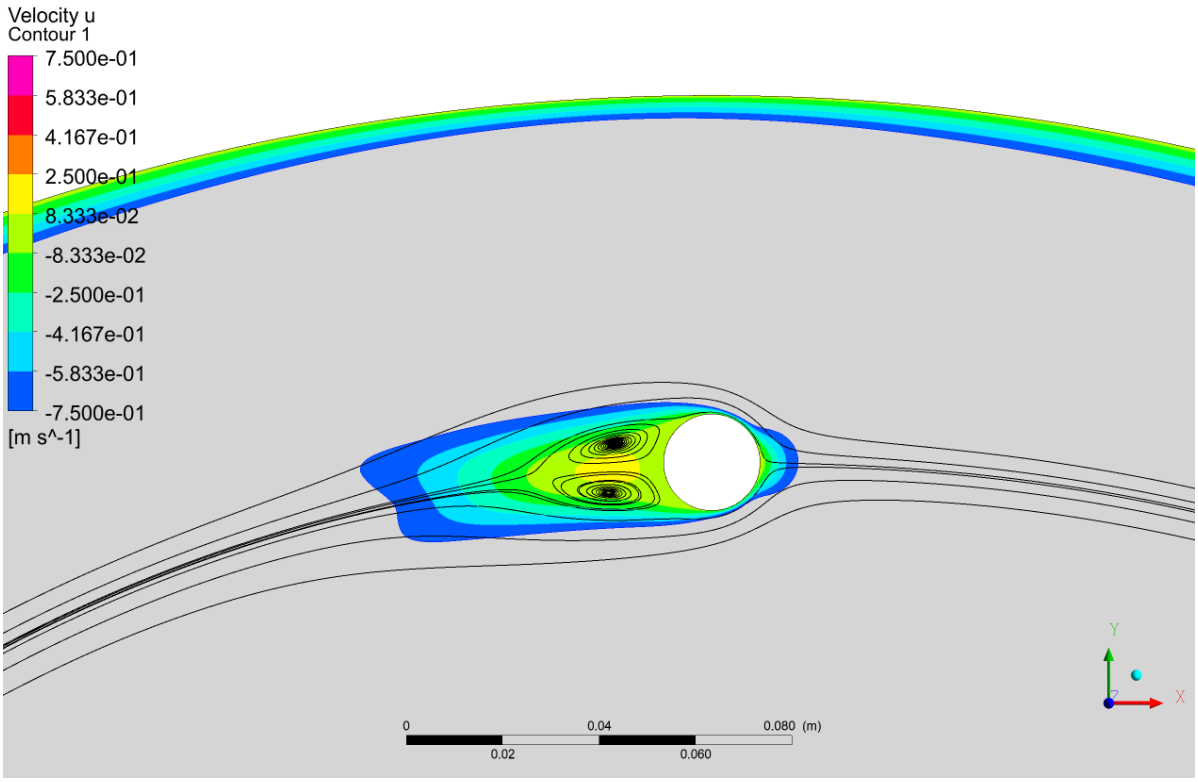

Figure 4.15: Streamlines and velocity contour plot of the flow past the cylinder in the carousel wind tunnel

4.3.2. Vortex Shedding

The second simulation is performed at a Reynolds number of 144. Comparing with Figure 2.10, it can be seen that vortex shedding should occur. A transient (time dependent) simulation was run to identify the vortex shedding. A time dependent simulation, and not steady state, has to be performed because the phenomena of vortex shedding is unsteady. The velocity flow field over time can be seen in Figure 4.16, 4.17 and 4.18. It must be noted that the time of the transient simulation is after a steady state simulation. First a steady state simulation is ran to enhance the computational speed. Comparing with Figure 2.10, it can be seen that the

wavy pattern consistent with vortex shedding is similar.

Although the pattern is present which is similar to vortex shedding, there are no vortices present in the wake of the cylinder. This can be due to one of the following two reasons:

- The time step of the transient simulation is to high to catch the phenomena of vortex shedding.
- The non-uniform inflow velocity influences vortex shedding in the wake of the cylinder.

The minimum time step required in a transient simulation is dependent on the minimum size of the mesh and the velocity, based on the Courant-Friedrichs-Lewy (CFL) number:

$$\text{CFL} = \frac{U}{\Delta x} \cdot \Delta t \tag{4.12}$$

From Chapter 3, the minimum size is determined to be equal to $4 \cdot 10^{-5}$. From de Moura and Kubrusly [13], it is determined that a CFL number of 0.4 - 0.5 provides results of high quality with minimal error. Based on the values of the velocity, minimum size and CFL number, the required time step is calculated to be equal to $2.96 \cdot 10^{-6}$s. It is thus clear that the time step of 0.01s used, is insufficient to capture all the correct phenomena. However, decreasing the time step increases the computational effort significantly. A time step of $2.96 \cdot 10^{-6}$s is unable to be used due to limiting computational resources. Therefore, a time step of 0.01s is used for this analysis.

Secondly, the non-uniform velocity can have an effect on the flow propagation of the vortices in the wake of the cylinder. Both the incoming flow, as the shear it experiences due to the rotating inner drum after the cylinder, can influence shedding of the vortices.

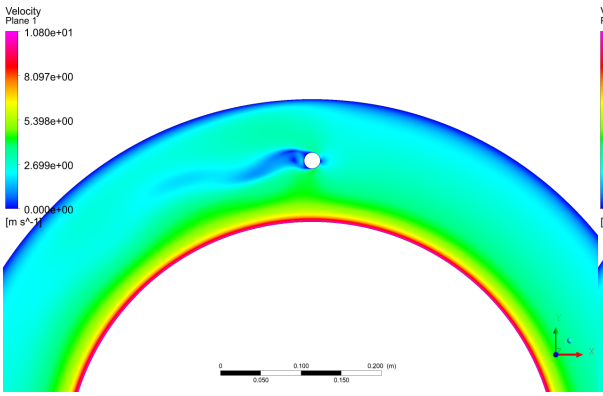

Figure 4.16: Velocity color plot of the transient simulation at t = 2s

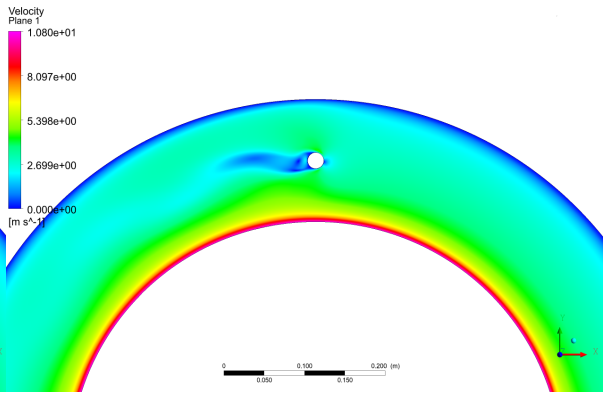

Figure 4.17: Velocity color plot of the transient simulation at t = 6s

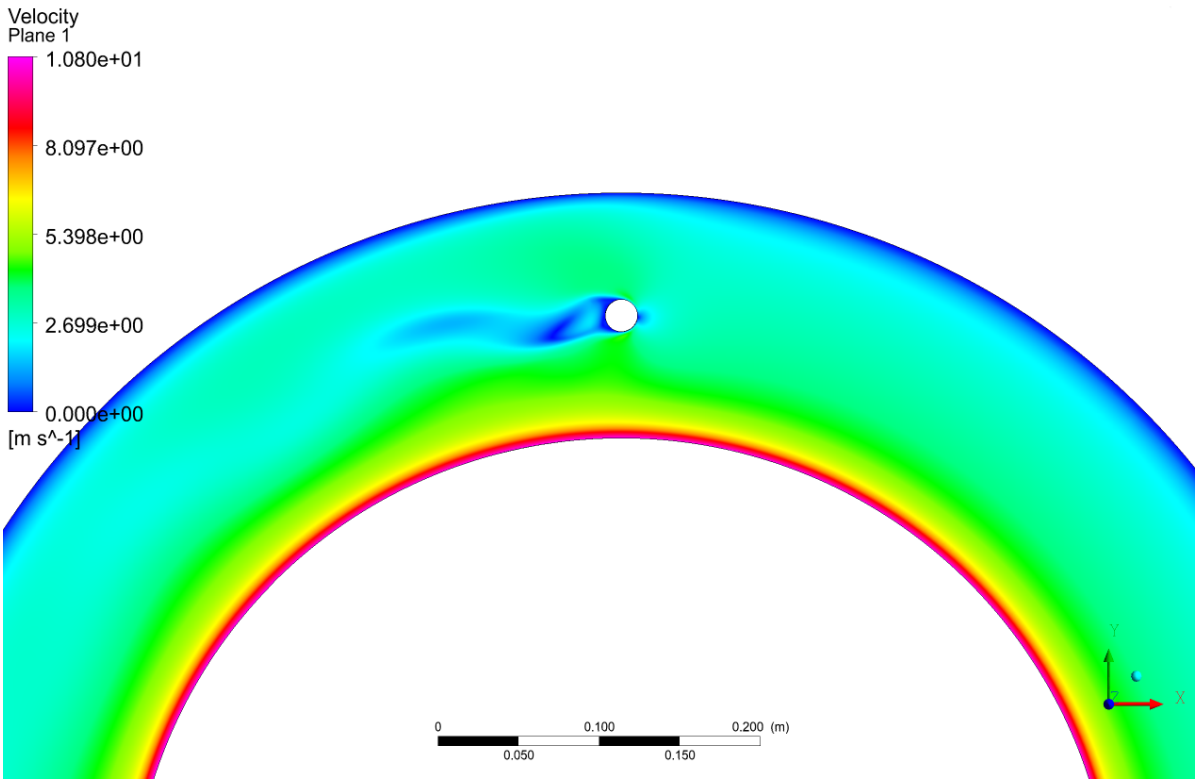

Figure 4.18: Velocity color plot of the transient simulation at t = 10s

When vortex shedding is present, the shedding frequency can be calculated. The shedding frequency is calculated based on the oscillating lift coefficient over time, which can be seen in Figure 4.19. The shedding frequency is determined by the time difference between two peaks of lift coefficient when it is stabilized. The time step between two peaks equals 0.0875s, which corresponds to a shedding frequency of 11.4 Hz.

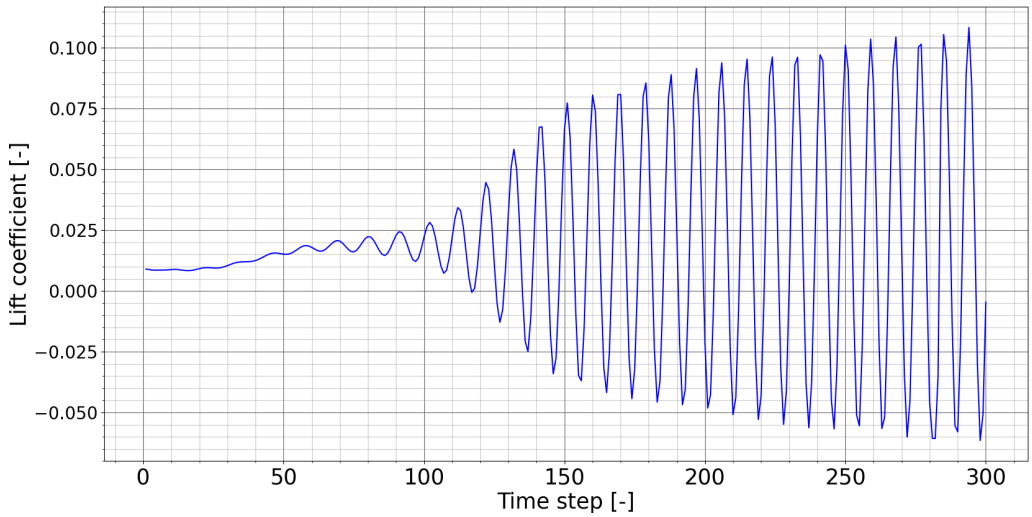

Figure 4.19: Lift coefficient vs time step

To measure the shedding frequency by a non-dimensional quantity, the Strouhal number (St) is defined by Equation 4.13 [3, 10]:

$$St = \frac{fD}{U} \tag{4.13}$$

where f is the shedding frequency, D is the diameter of the cylinder, and U is the flow velocity.

With a shedding frequency of 11.4Hz, a diameter of 0.02m and an average velocity of 3.225 m/s, the Strouhal number equals 0.071. For larger Reynolds numbers, the Strouhal number is constant with a value of 0.2. However, for smaller Reynolds numbers, up until 300, the Strouhal number increases with increasing Reynolds number. The Strouhal number varying with the Reynolds number can be seen in Figure 4.20 [10]. With a Strouhal number of 0.071 at a Reynolds number of 144, the Strouhal number is significantly lower compared to the reference data. Therefore, it is concluded that due to the time step and influence of the velocity profile, vortex shedding cannot be accurately compared with the available reference data.

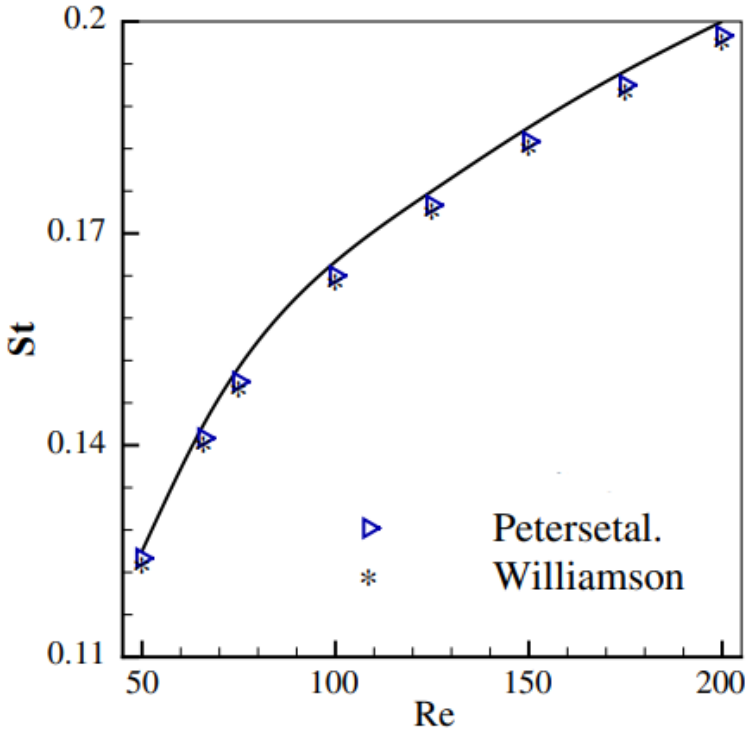

Figure 4.20: Strouhal number vs Reynolds number, adapted from Bhattacharyya and Singh [10] with data from Williamson [71] and Peters et al.[50]

4.3.3. Curvature Effect in the 2D Flow Field

To analyse the effect of curvature on the flow, the Föpple vortices are analysed again. In Figure 4.15, the results from a steady state simulation of the contour of a range of the velocity over the cylinder can be seen. The shape of this outer contour is analysed with respect to the curvature. To analyse the effect of curvature, the plot of the contour of the curved profile (red line in Figure 4.21), is converted to a straight velocity profile (blue line in Figure 4.21).

It can be seen that the direct effect of the curvature is relatively minimal. Both shapes remain closely related. The asymmetric contour is not resolved solely by removing the curvature. The asymmetric contour is the cause of the tiled velocity profile. Due to the lower absolute velocity on the upper side of the cylinder, the contour is longer on that side. The contour plot indicated a velocity component, which in this case is relatively small. Therefore, the asymmetric case is due to the elongation on the upper side. At the lower side, a higher a absolute velocity is reached and thus behind the contour a more negative value of the velocity is situated.

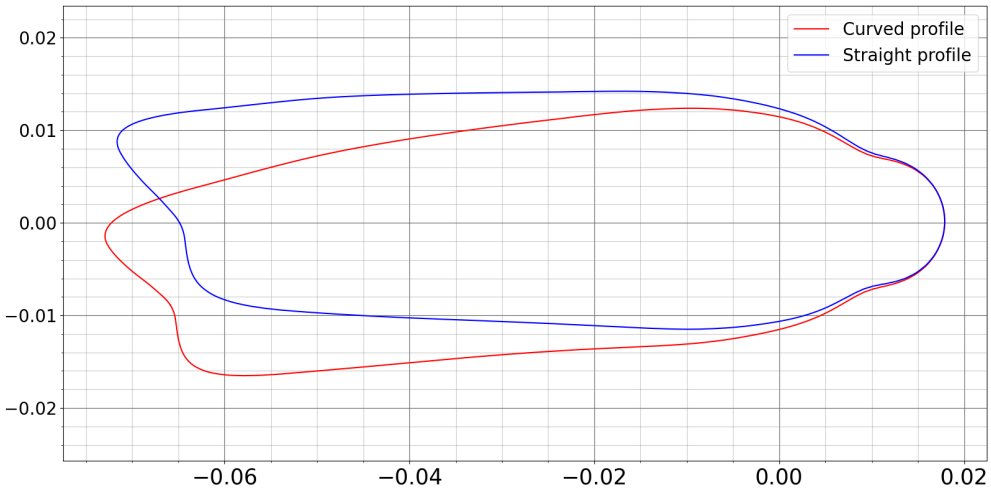

Figure 4.21: Curved and straight contour profile

4.3.4. Effect on the Flow Propagation in the Carousel Wind Tunnel

To determine the effect the cylinder has on the complete wind tunnel, which is important to know when wanting to place a test object, the effect of the cylinder on the flow propagation in the carousel wind tunnel is investigated. First of all, the velocity in the complete carousel wind tunnel is examined. This is done by looking at the colour contour plot in Figure 4.22. The reduction in flow velocity due to the wake can clearly be seen. Furthermore, due to the increase in flow velocity above and below the cylinder, the boundary layer is affected. This can be more clearly seen in the pressure contour plot in Figure 4.24. The low pressure under and behind the cylinder results in a decreased pressure at the boundary layer on the inner drum. Furthermore, next to the boundary layer of the inner and outer drum, a high pressure region in front of the cylinder corresponds to the stagnation point and thus high pressure. Lastly, in Figure 4.23, it can be seen that the pressure gradient is not uniform at different sections in the carousel wind tunnel. Some fluctuations are present, which will be discussed in more detail next.

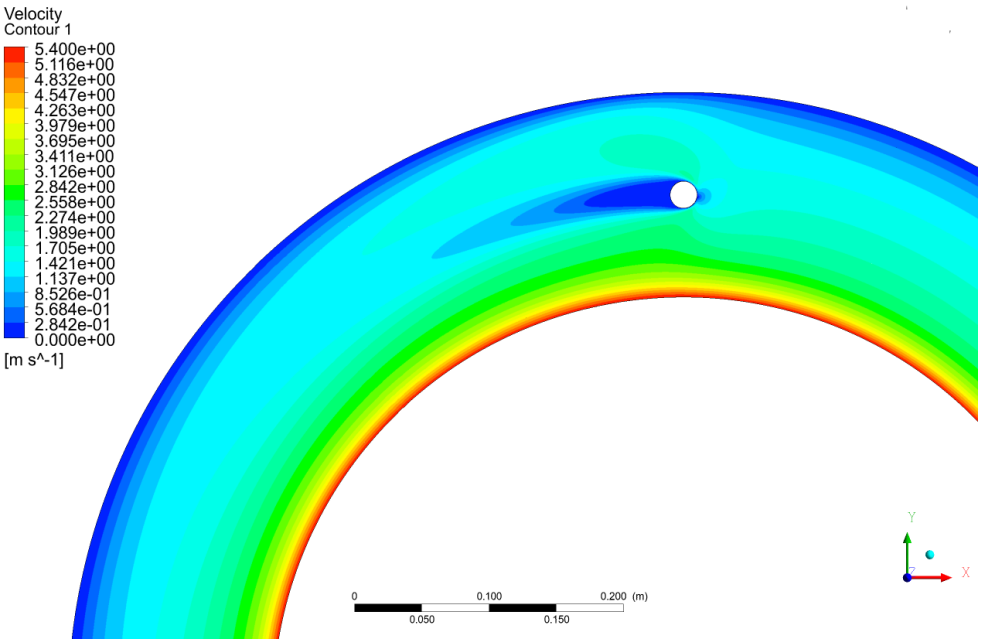

Figure 4.22: Close-up contour plot of the velocity in the cylinder-region

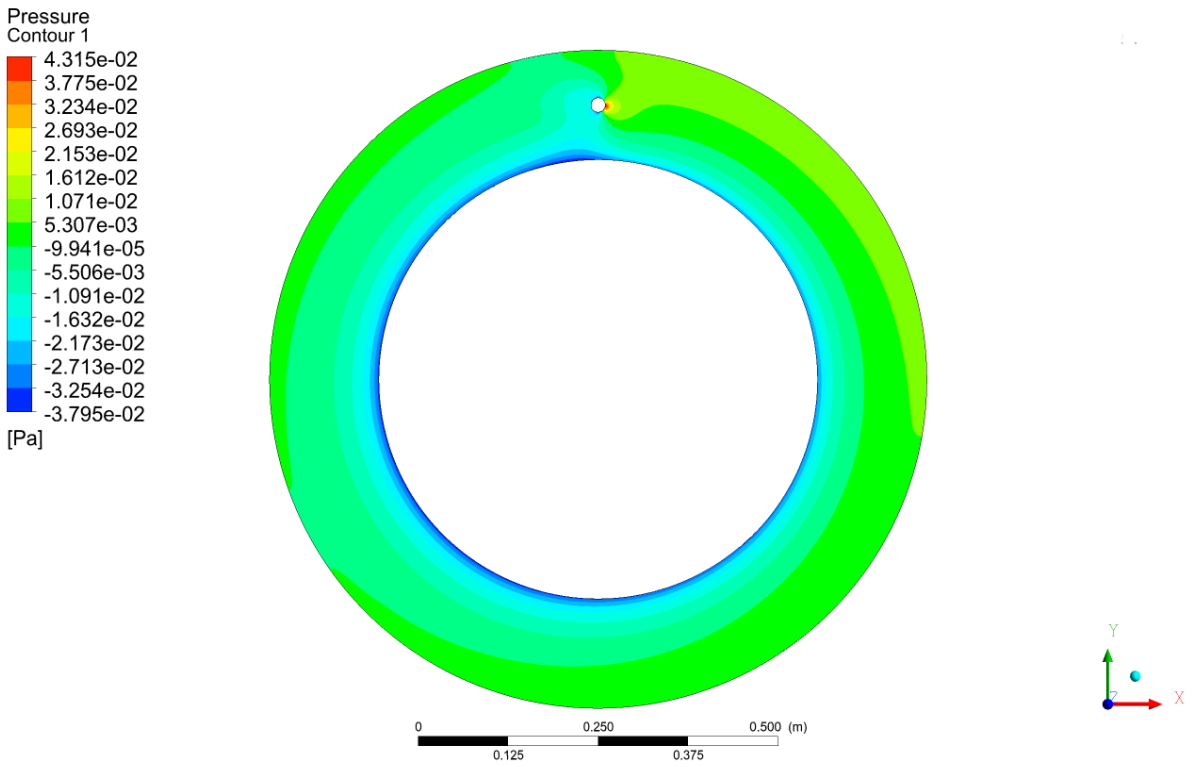

Figure 4.23: Contour plot of the pressure in the carousel wind tunnel, disturbance simulation

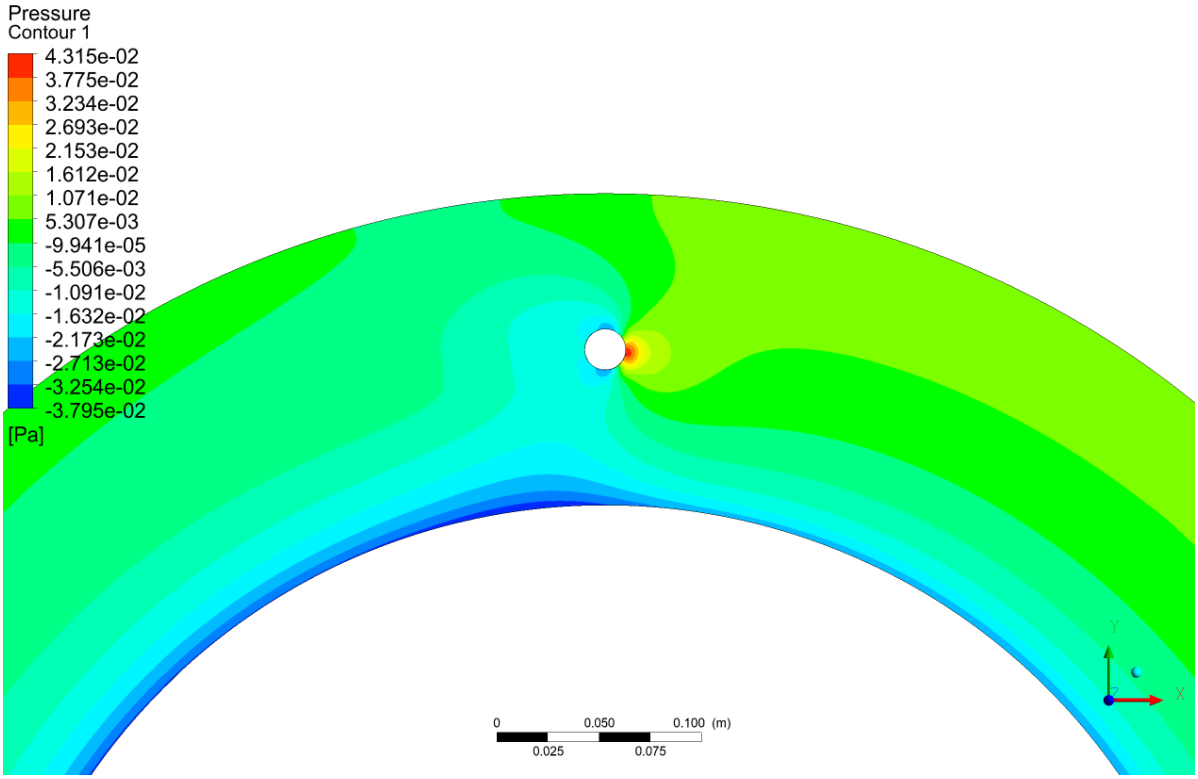

Figure 4.24: Close-up contour plot of the pressure in the cylinder-region

Lastly, the velocity profile is examined in detail at different sections in the carousel wind tunnel. The velocity profile is examined 90°, 180° and 270° counterclockwise relative to the location of the cylinder. The velocity profile at these three locations compared to the original velocity profile without the cylinder causing the disturbance can be seen in Figure 4.25. It is clear that the disturbance results in a definite alteration of the velocity profile. Although the profile closer to the cylinder (at 270°) takes a shape that is comparable to the undisturbed velocity profile, it is significantly different. This indicates that when implementing a test object, the velocity profile will be different and form a new one depending on the shape of the test object.

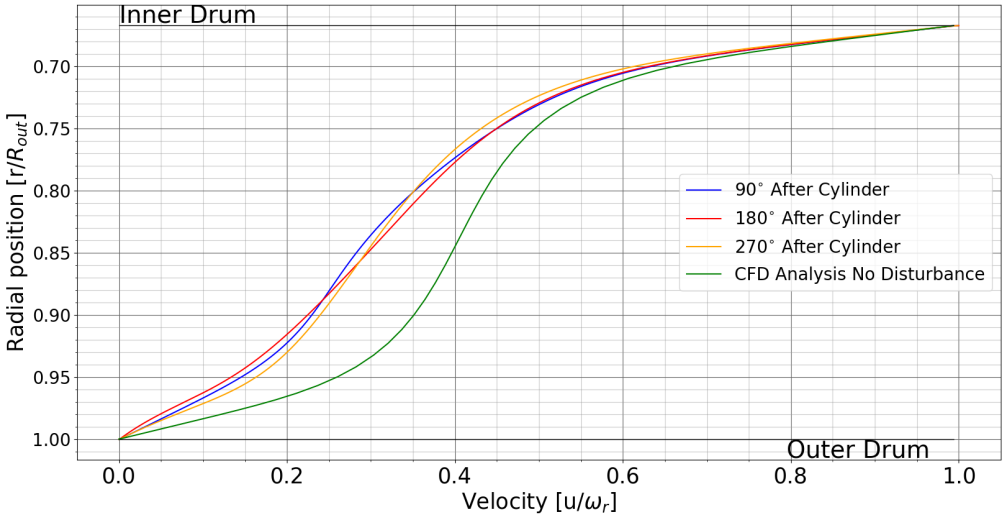

Figure 4.25: Progression of the disturbed velocity profile

4.3.5. Effect of Blockage on the Velocity Profile

Blockage in a wind tunnel is a common effect that occurs in every closed wind tunnel facility. Blockage is the increase of velocity (and also lift, drag, ...) over the test object due to the placement of the test object in a closed environment with walls. Therefore, the measured parameters are different compared to real situations, and it should thus be corrected for. The correction is done by a parameter which correct the velocity by Equation 4.14 [64]. In this report, the solid and wake blockage factors are considered.

$$U' = \frac{U}{(1+\epsilon_b)} \tag{4.14}$$

where U' is the undisturbed (apparent) velocity and ϵ_b the total blockage factor.

The total blockage factor is divided into two elements, the solid blockage factor and the wake blockage factor:

$$\epsilon_b = \epsilon_s + \epsilon_w \tag{4.15}$$

where ϵ_s is the solid blockage (blockage due to the model), and ϵ_w is wake blockage.

Due to the displacement of the streamlines in the wind tunnel due to the walls, the velocity is different compared to a 'free flight' scenario. The tunnel walls cause a increase in axial velocity. The increase in axial velocity due to the solid blockage is accounted for by Equation 4.16 [20].

$$\epsilon_s = \frac{\pi}{6}\left[1+1.2\beta\left(\frac{t}{c}\right)\right]\frac{A}{\beta^3 h^2} \tag{4.16}$$

where β is the Prandtl-Glauert compressibility correction factor $\sqrt{1-M'^2}$ (with M' being the uncorrected Mach number), t is the thickness of the cylinder (height), c is the chord of the cylinder (diameter), A is the

cross sectional area and h is the height of the tunnel.

The last blockage factor is the wake blockage. The wake blockage factor is accounted for by Equation 4.17.

$$\epsilon_w = \frac{1}{4}\left(\frac{c}{h}\right)\frac{1+0.4M'^2}{\beta^2}C'_d \tag{4.17}$$

where $C_d{}'$ is the uncorrected drag coefficient. This drag coefficient can be calculated by determining the normal and axial force component of the cylinder:

$$c_\mathrm{d} = c_\mathrm{n} sin\alpha + c_\mathrm{a}\cos\alpha \tag{4.18}$$

where c_n and c_a equal:

$$c_\mathrm{n} = \frac{1}{c}\int_0^c (C_\mathrm{p,l} - C_\mathrm{p,u})dx \tag{4.19}$$

$$c_\mathrm{a} = \frac{1}{c}\int_0^c \left(C_\mathrm{p,u}\frac{dy_\mathrm{u}}{dx} - C_\mathrm{p,l}\frac{dy_\mathrm{l}}{dx}\right)dx \tag{4.20}$$

where $C_\mathrm{p,l}$ and $C_\mathrm{p,u}$ are the pressure coefficients of the upper and lower side of the cylinder and $\frac{dy_\mathrm{u}}{dx}$ and $\frac{dy_\mathrm{l}}{dx}$ is the gradient of the cylinder on the respectively upper and lower side.

However, since the angle of attack is assumed to be zero, the normal component gets removed from the equation and thus only c_a needs to be determined. From Equation 4.20, it can be seen that the pressure coefficient is needed. The pressure coefficient equals [5]:

$$C_\mathrm{p} = \frac{p - p_\infty}{q_\infty} \tag{4.21}$$

Here, the parameters static pressure (p), freestream static pressure (p_∞) and freestream dynamic pressure (q_∞) are known from the CFD analysis, and thus, C_d can be calculated.

Doing this results in a total correction factor of 0.156. Applying this to the velocity profile, results in Figure 4.26. It can be seen that the velocity profile is reduced in velocity (shifted to the left), as expected. The shifted profile is relatively large. It is therefore concluded that for the application of measuring aerodynamic forces, it is crucial that blockage correction factors are applied to obtain reliable and accurate results. It must be noted that the correction is applied over the complete velocity profile, and thus the velocity at the inner drum is lower than the rotational velocity. In a real life application this would not be the case, however, the main importance is the effect of the blockage on the general velocity profile.

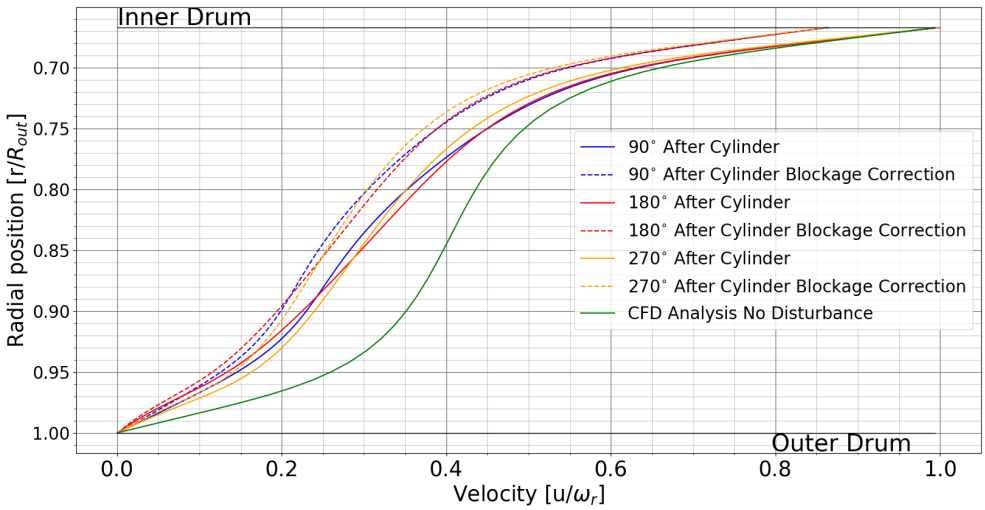

Figure 4.26: Progression of the disturbed velocity profile with and without blockage correction

Based on the analysis of the flow disturbance, it is concluded that accurate measurements of aerodynamic forces are not achievable. Due to the fact that every different test object results in a different velocity profile, no correlation can be made between the incoming flow velocity and the forces that will be measured. Although the effect of blocking can be accurately applied, the velocity profile remains unstable over the complete domain of the carousel wind tunnel. The velocity profile does not recover to its undisturbed velocity profile, and it does not transform to a velocity profile which is feasible to perform measurements in. However, as this is still a 2D simulation, a 3D analysis is necessary to make a definite conclusion. The effect of the walls will affect the velocity profile and its flow propagation which does not allow for a definite conclusion to be made at this point.

4.4. 3D Velocity Field

The last step in determining the feasibility of the carousel wind tunnel for both the measurement of aerodynamic forces, and the measurement of threshold shear velocities is to perform a 3D simulation. The 3D simulation includes the sides as walls, instead of extending it to infinity, which is the case for the 2D simulation. Therefore, the simulation provides data on the flow effects that occur due to the presence of the side walls.

4.4.1. Secondary Flow Effects

The most well known secondary flow effect of Taylor-Couette flow, and thus for the carousel wind tunnel, is the Taylor vortices. In the Martian simulation with rotational velocity of 169 RPM, the Reynolds number of the carousel wind tunnel equals 1278. Comparing this with Figure 2.8, it can be seen that the Reynolds number is on the edge between modulated waves and turbulent Taylor vortices. Therefore, it is expected that one of these two flow phenomena will be present.

To investigate this, first of all, a closer look is taken at the velocity in the YZ-plane (plane parallel to the length of the carousel wind tunnel). In Figure 4.27, the velocity in the carousel wind tunnel can be seen. This velocity plane indicates that a pair of Taylor vortices are indeed present. This is confirmed by comparing it with literature, which is depicted in Figure 4.28 [44]. Here, the same patters is depicted. However, multiple pair of Taylor vortices are present. From Equation 2.7, it is known that the amount of Taylor vortices is dependent on the length of the carousel wind tunnel. With the width and height of the Taylor vortices being equal to the gap width, the number of Taylor vortices is equal to the ratio of the length to the gap width. Therefore, as mentioned in the previous section, it was chosen for the length of the model to be 0.304m such that exactly one pair of Taylor vortices is present, and which is now also proven to be the case.

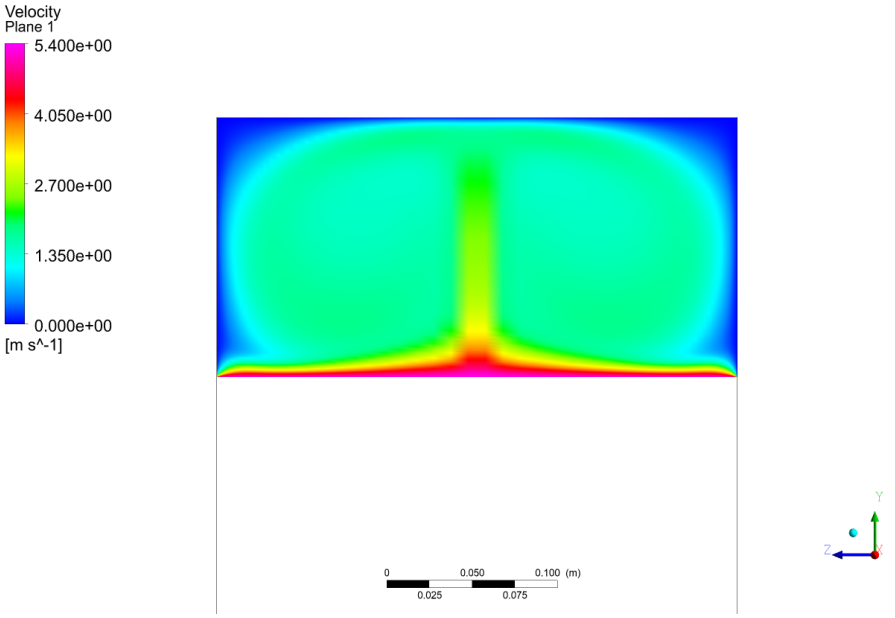

Figure 4.27: Close-up colour plot of the velocity in the carousel wind tunnel in a 3D simulation

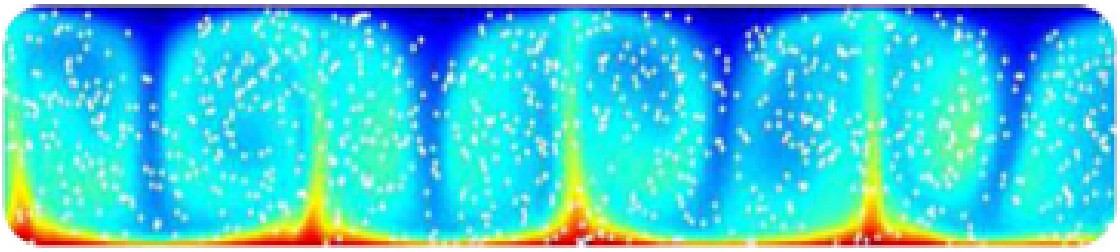

Figure 4.28: Velocity at the YZ-plane from Nemri et al.[44]

Next to the velocity plane, the pair of Taylor vortices can also be seen when tracing particles. Particles are simulated in the carousel wind tunnel and their path is saved. By doing this, the Taylor vortices can be seen over the complete carousel wind tunnel. When tracing the particles, a toroidal shape is present in the carousel wind tunnel. This toroidal shape can be seen in Figure 4.29.

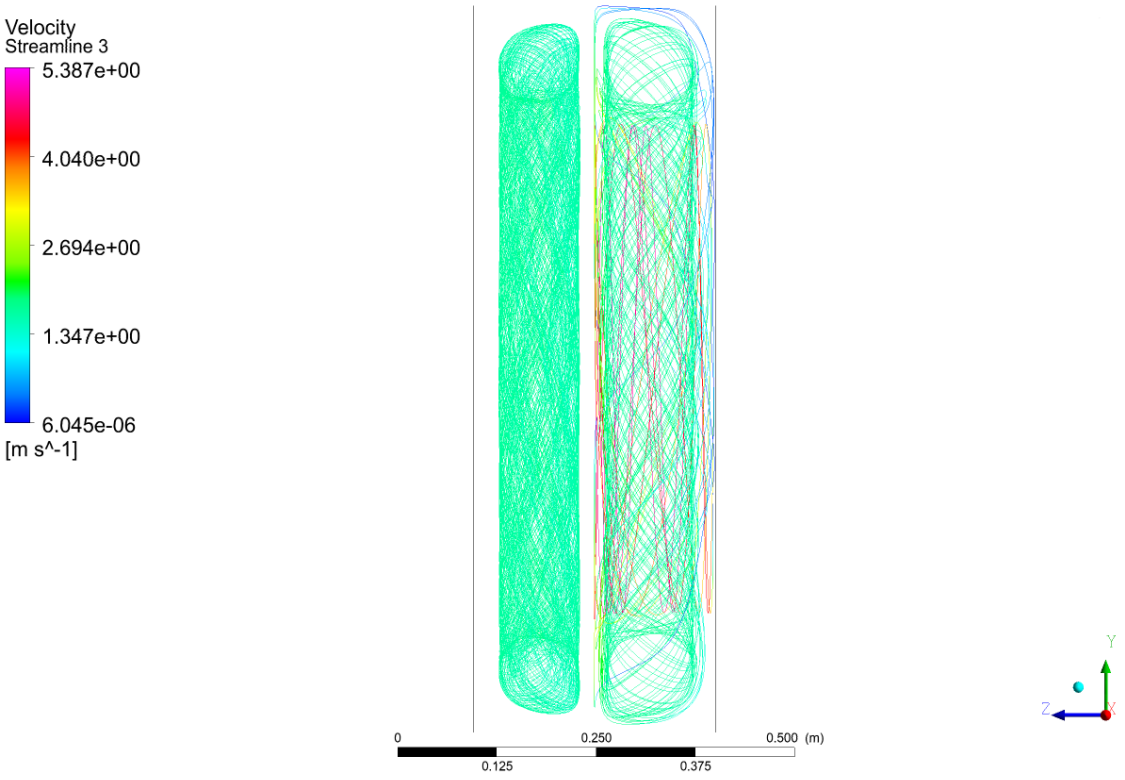

Figure 4.29: Side view of the 3D streamlines in the carousel wind tunnel

Lastly, to show both the direction and the velocity of the fluid, a vector plot is made. The vector plot can be seen in Figure 4.30. Here, the length of the vectors cannot be related to the velocity due to the fact that the vector plot is 3D, and the figure shown is a plane. The 2D vectors in the plane are a projection of the 3D vectors. However, what can clearly be seen is the rotating effect of the Taylor vortices by looking at the direction of the vectors. Here, it can be seen that the pair of Taylor vortices are indeed counter rotating.

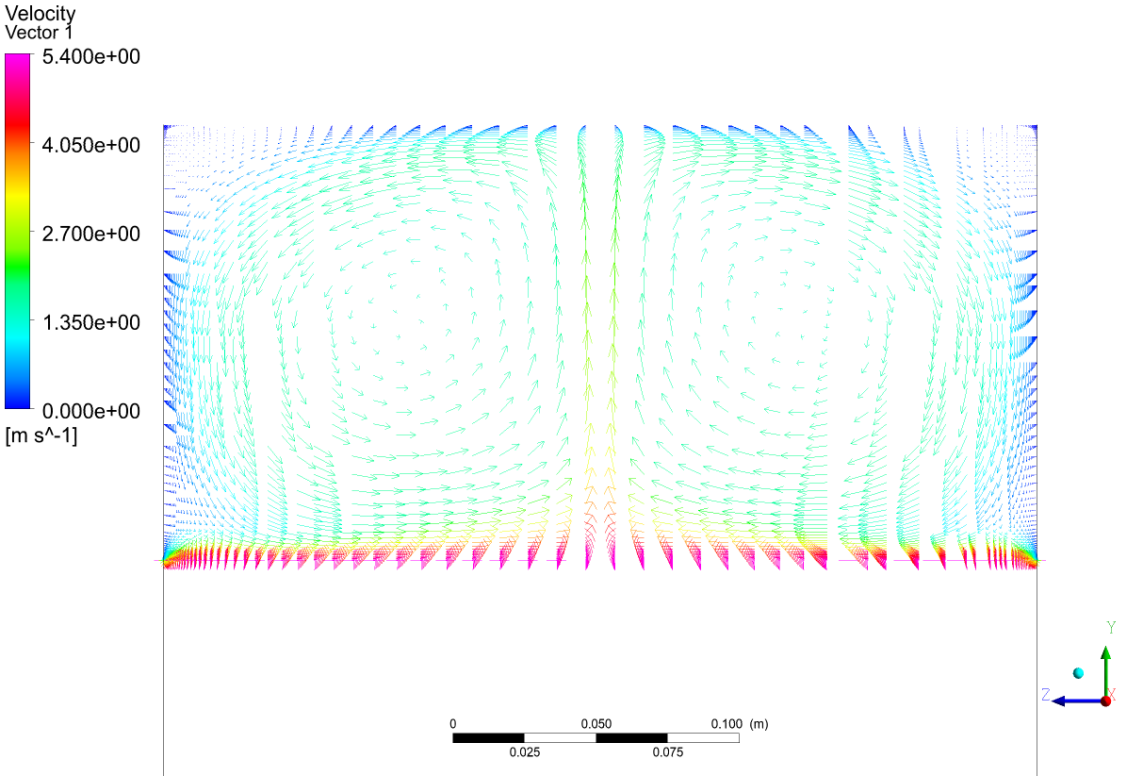

Figure 4.30: Velocity vector in the carousel wind tunnel indicating the vorticity

4.4.2. Curvature Effect in the 3D Flow Field

The carousel wind tunnel consists of two cylindrical drums. Due to the curved surface, the flow is curved as well. It is important to know where the curvature of the flow is high. When the flow curvature would be high in the region where aerodynamic or planetary science experiments would take place, it would take additional corrections to be able to obtain reliable and high quality data.

To investigate the effect of the flow curvature the following parameter is defined [57]:

$$\psi = \frac{U/r}{dU/dr} \tag{4.22}$$

This parameters is the ratio of the flows angular velocity to the radial velocity gradient. The result can be seen in Figure 4.31. If the parameter ψ is close to -1, it indicates that the flow is dominated by the curvature [57]. The closer the value is to 0, and thus the higher the velocity gradients, the less the flow is affected by curvature. From Figure 4.31, it can be seen that only close to the inner and outer drum, the parameter is close to zero. And thus, for the Reynolds number of 1278, the flow is dominated by the curvature in most of the central region of the carousel wind tunnel. This again indicates that performing accurate aerodynamic measurements will be extremely difficult, if not impossible in the carousel wind tunnel. However, it also indicates that the measurements of aeolian process, which will be located a the outer drum, will not be affected by the curvature.

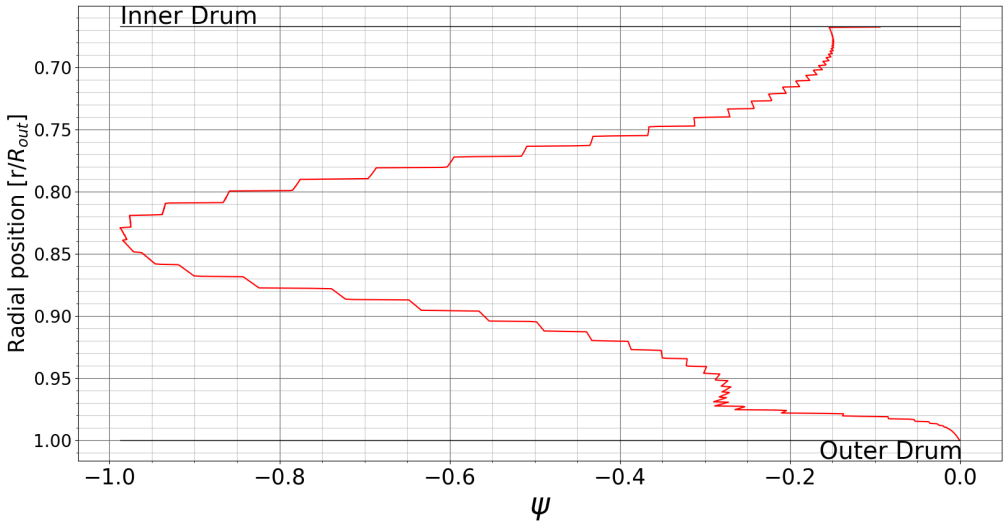

Figure 4.31: Flow curvature parameter, ψ vs radial position

4.4.3. Vorticity in the Carousel Wind Tunnel

In Subsection 4.4.1, the Taylor vortices have been identified. To define the area in the carousel wind tunnel where the vorticity component of the flow is larger than the shear component, the Q-criterion is defined. The Q-criterion can be derived from the velocity gradient. The velocity gradient, $\nabla\vec{v}$, can be decomposed into the following two parts [76]:

$$\nabla\vec{v} = \frac{1}{2}\left(\nabla\vec{v} + \nabla\vec{v}^{\,T}\right) + \frac{1}{2}\left(\nabla\vec{v} - \nabla\vec{v}^{\,T}\right) = \vec{S} + \vec{\Omega} \tag{4.23}$$

Where $\vec{S}$ is the rate of strain, or the symmetric part, and $\vec{\Omega}$ is the vorticity tensor, also known as the antisymmetric part.

From the two parts, symmetric and antisymmetric, the Q-criterion is defined by Equation 4.24.

$$Q = \frac{1}{2}\left(||\vec{\Omega}||^2 - ||\vec{S}||^2\right) \tag{4.24}$$

For Q > 0, it indicates the existence of vortices. Looking at the definition, Equation 4.24, it is defined as areas where the magnitude of the rate of strain ($\vec{S}$) is lower than the magnitude of the vorticity ($\vec{\Omega}$). It provides info into the locations in the carousel wind tunnel where rotation of the flow is relatively more present compared to the shear components of the flow [76]. Therefore, to visualize where the vortices are present, the areas of the flow where Q > 0 are visualized. This is done in Figure 4.32. It is no surprise that these grey areas coincide with the Taylor vortices. However, now they are mathematically defined by the Q-criterion.

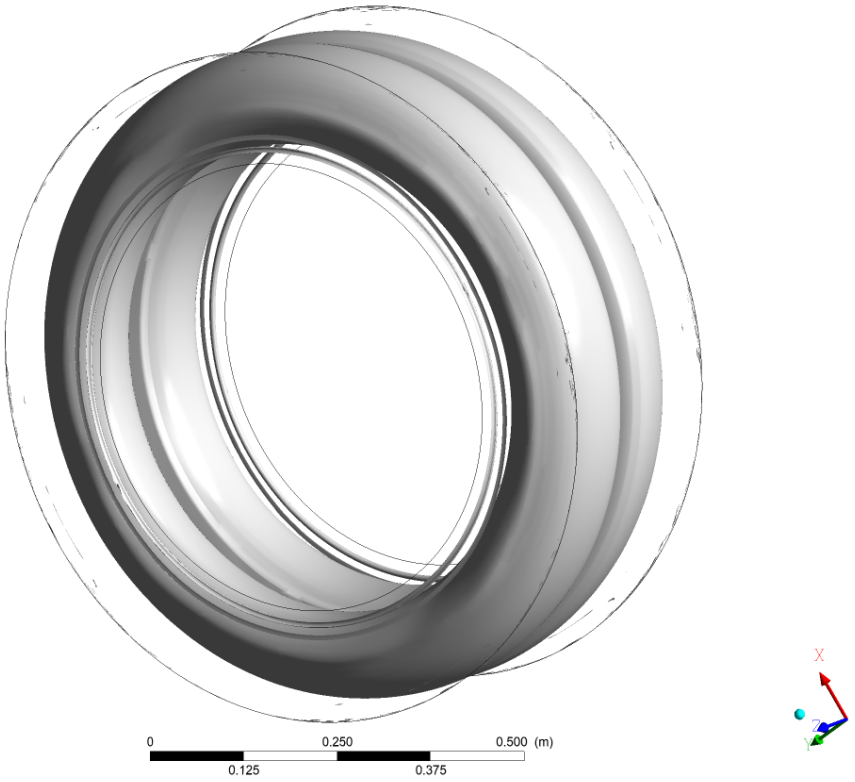

Figure 4.32: ISO view of the Q-criterion

Although the Q-criterion relates vorticity relative to the shear component of the flow, the strength of the vorticity still needs to be defined. Therefore, the vorticity is plotted over the centre line in the carousel wind tunnel in Figure 4.33. Vorticity is plotted for two different rotational velocities: 169 and 3520 RPM. Vorticity increases with increasing rotational velocity. Furthermore, at half the spanwise location, vorticity changes from a positive to a negative value. This is due to the merging two vortices. Furthermore, since they are counterrotating, the magnitude of each vortice is different.

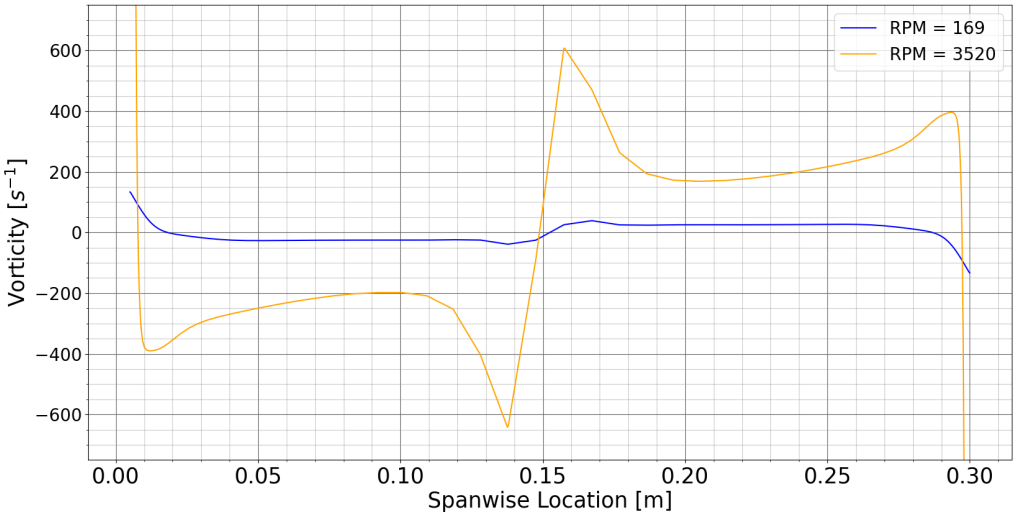

Figure 4.33: Vorticity on the centre line of the carousel wind tunnel

The strength of the vorticity in the carousel wind tunnel is calculated by Equation 4.25 [77].

$$J = \int\int_A \omega \cdot n dA \tag{4.25}$$

where J is the strength of the vorticity, ω is the vorticity, n the unit vector, and A the surface area.

The strength of the vorticity equals 22 904 m^2/s for a rotational velocity of 169 RPM, and $1.1{\cdot}10^6 m^2/s$ for a rotational velocity of 3520 RPM. Here, the strength of the vorticity is connected with the aim of this report: to determine whether or not measurements are possible. To vorticity on the centre line indicates that aerodynamic measurements are not possible with this configuration and setting. Although the Q-criterion showed where the vorticity is greater relative to the shear component, the vorticity will still have an influence in the outer regions of the drum. Therefore, in the next subsection, the effect of vorticity on the shear velocity is determined.

The outcome of the analysis on the vorticity in the flow field of the carousel wind tunnel provides a mathematically insight in the difficulty of performing aerodynamic measurements, The location where vorticity is significantly present coincides with the location where aerodynamic measurements where to be performed. Only if the vorticity in the carousel wind tunnel can be reduced, there would exist a possibility in performing aerodynamic measurements.

4.4.4. Effect of Vorticity on the Shear Velocity

In the previous subsection, the vorticity strength in the carousel wind tunnel is analysed. From the Q-criterion, the vorticity component of the flow was lower at the walls compared to the shear component. However, the vorticity distribution in the carousel wind tunnel does affect the velocity distribution over the outer drum. Therefore, it will have an effect on the shear velocity. This effect can be seen in Figure 4.34. It can be seen that the shear velocity is far from uniform along the outer drum. The shear velocity increased when propagating towards the middle section, which is consistent with the vorticity along the centre line of the carousel wind tunnel. The vorticity has a direct effect on the shear velocity at the outer drum. Accurate determination of the Taylor vortices is required to relate the section on the outer drum to the correct shear velocity. The configuration can be used to measure the threshold shear velocity. The particles are placed on the outer drum, and the inner drum starts to rotate. Since the relation between the shear velocity and the location on the outer drum is known, the threshold shear velocity can be determined. When particle movement occurs, the location of the particles, and thus the threshold shear velocity, is known.

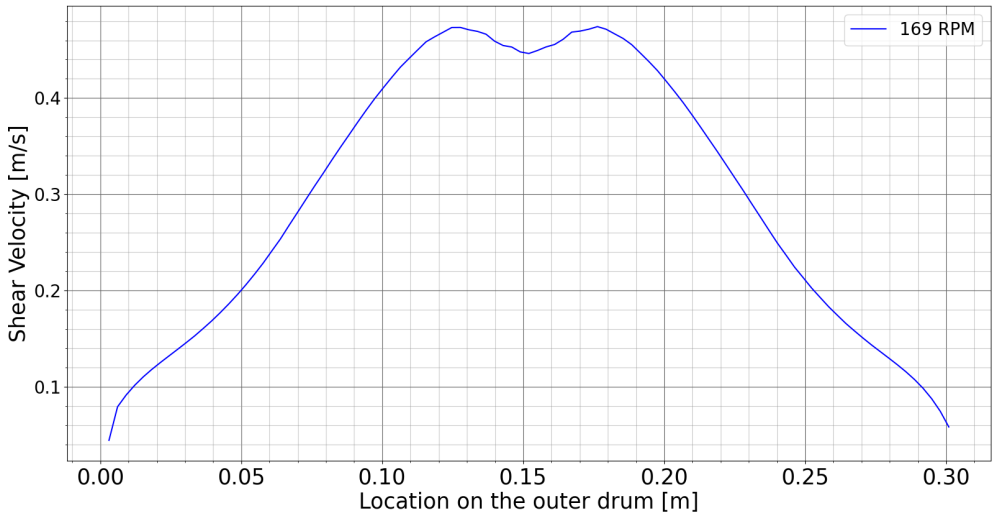

Figure 4.34: Shear velocity distribution in the carousel wind tunnel at a rotational velocity of 169 RPM

In Section 4.2, it is determined that a rotational velocity of 3530 RPM was necessary in order to achieve

the threshold shear velocity. However, this calculation was a 2D calculation where any 3D effects were ignored. Therefore, the shear velocity over the outer drum is plotted in Figure 4.35. The shear velocity required equalled 3.48 m/s. In Figure 4.35, it can be seen that this shear velocity is reached. Therefore, the carousel wind tunnel in this configuration is capable of performing aeolian measurements to determine the threshold shear velocity. However, it must be noted that the presence of the Taylor vortices make the measurements more difficult. Both the location of the particle, and the relation between the shear velocity and the location on the outer drum must be known with high accuracy. The carousel wind tunnel has a depth of 30.5cm. Therefore, a few millimeter difference can results in a significant difference in shear velocity, as can be seen in Figures 4.34 and 4.35. Therefore, an analysis and discussion is performed to determine how the threshold shear velocity can be determined without Taylor vortices being present.

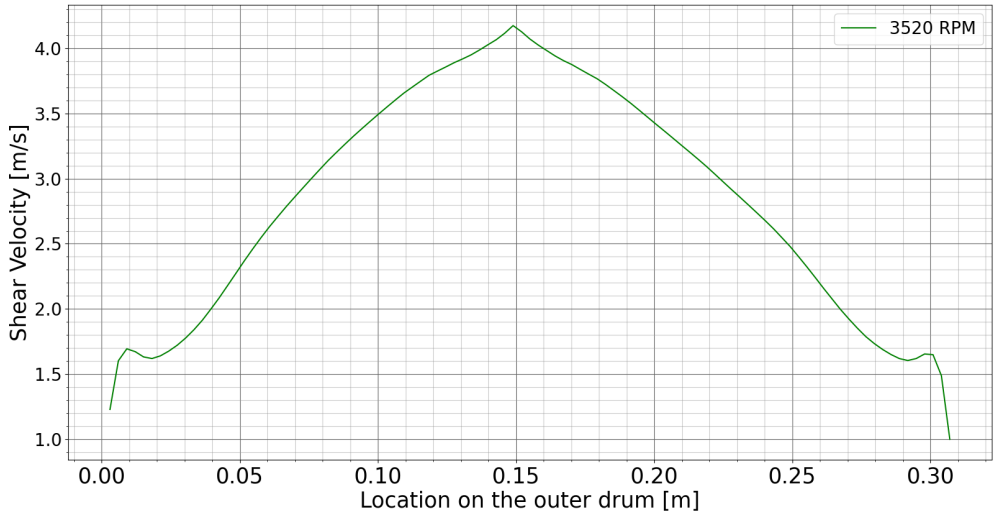

Figure 4.35: Shear velocity distribution in the carousel wind tunnel at a rotational velocity of 3520 RPM

To be able to use the carousel wind tunnel for aeolian experiments in the exact atmospheric conditions of Mars without Taylor vortices being present, modifications need to be made. From literature, it is determined that a Reynolds number of at least 40 000 is necessary for the flow to be fully turbulent, with no Taylor vortices being present [19, 57]. With the rotational velocity of 3230 RPM, the Reynolds number equals 34 044. As a results, the minimum necessary Reynolds number (40 000) would result in a shear velocity above the threshold shear velocity. Therefore, the carousel wind tunnel in its current configuration cannot be used to measure the threshold shear velocity for particles in need of a shear stress of 0.2 Pa to start moving in the exact Martian atmospheric conditions without Taylor vortices being present. Three possible solutions have been found:

1. Measure the threshold shear velocity of smaller particles, who are in need of a shear stress > 0.2 Pa, according to Figure 4.12.
2. Increase the gap size between the inner and outer drum by increasing the outer drum radius.
3. Increase the gap size between the inner and outer drum by decreasing the inner drum radius.

Measurement of Smaller Particles

Looking back at Figure 4.12, it can be seen that for particles with sizes in range of 20 to 63 μm, the shear stress is in range of 0.45 to 0.55 Pa. This is significantly higher compared to the 0.2 Pa of which the necessary rotational velocity of 3230 RPM was calculated. By this increase in shear stress, the threshold shear velocity will be increased as well, following from Equation 4.9. The shear velocity for this range of shear stress will be between 5.22 m/s (for a shear stress of 0.45 Pa), and 5.77 (for a shear stress of 0.55 Pa). Therefore, a higher rotational velocity for this configuration of the carousel wind tunnel is necessary to reach the threshold shear velocity. Following from this, it is thus possible that the Reynolds number of 40 000 is reached before the

threshold shear velocity is reached. Using the fit obtained in Section 4.2, it is determined that the rotational velocity will be in the range of 46 264 and 54 727. Therefore, no secondary effects are introduced into the flow, and the threshold shear velocity is not reached before the flow is completely turbulent with no Taylor vortices.

Increased Gap Size by Extending Outer Drum Radius

A second possible solution would be to increase the size between the inner and outer drum. By increasing the size between the inner and outer drum, the Reynolds number is increased. However, one must also look at the effect this has on the shear velocity. To analyse this, a new set of simulations is done, and a new regression between the shear velocity and rotational velocity is made.

The radius of the outer drum is extended to 0.610m. For this model, the correlation between the shear velocity and the rotational velocity can be seen in Figure 4.36. The necessary shear velocity of 3.48 m/s, corresponding to particles of 0.2 Pa, is achieved at a rotational velocity of 6074 RPM based on this 2D simulation. Since the distance between the inner and outer drum is enlarged, the Reynolds number is increased as well. The rotational velocity of 6074 RPM with a gap width of 0.305m correspond to Reynolds numbers of 92 105 respectively. Both Reynolds numbers are well over the limiting Reynolds number of 40 000 at which the flow becomes turbulent with no secondary flow effect.

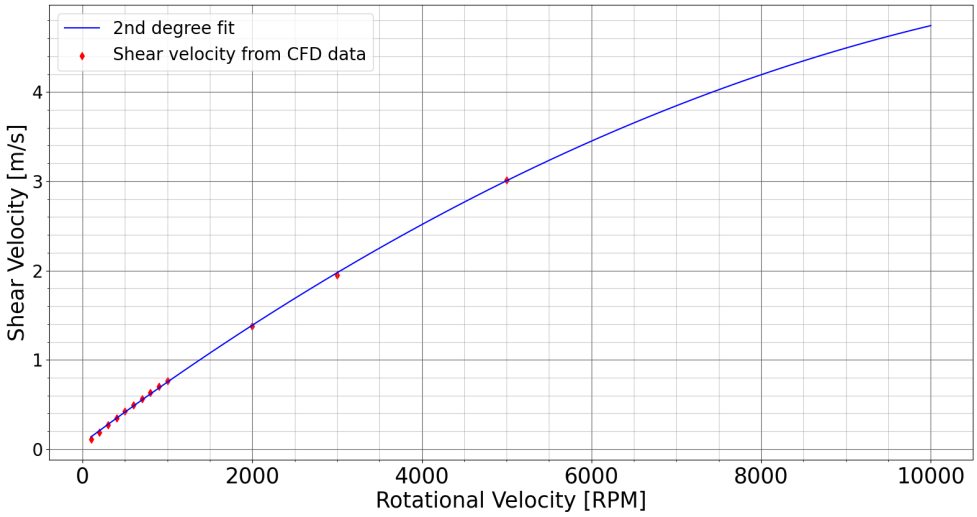

Figure 4.36: Shear velocity vs rotational velocity for a gap width of 0.305m, R_i = 0.305m and R_o = 0.610m

Increased Gap Size by Reducing Inner Drum Radius

The last possible solution to measure threshold shear velocities in a fully turbulent flow is to reduce the inner drum radius. The same objective is reached for as for the increased outer drum radius: increasing the Reynolds number. However, similar to increasing the outer drum radius, the effect of decreasing the inner drum radius on the shear velocity must be investigated. This is done in a similar manner, i.e. by performing CFD simulations and determining the relation between the shear velocity and the rotational velocity.

The correlation can be seen in Figure 4.37. It can be seen that the shear velocity of 3.48m/s will not be reached within an acceptable range of rotational velocity. It is therefore concluded that decreasing the inner drum size is not effective in trying to achieve accurate results for aeolian experiments.

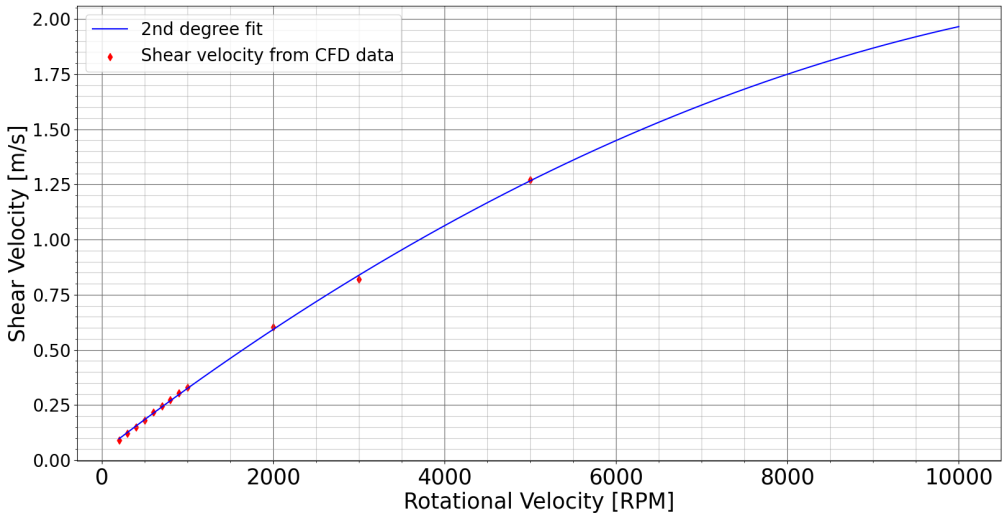

Figure 4.37: Shear velocity vs rotational velocity for a gap width of 0.305m, R_i = 0.152m and R_o = 0.457m

4.5. Comparison with Existing Carousel Wind Tunnel

Now that the carousel wind tunnel has been analysed in detail, a comparison can be made, and a critical opinion can be formed on the carousel wind tunnels already in use, or ones that have been used in the past. For this comparison, two carousel wind tunnels will be analysed: by Demirci et al.[15] and by Greeley et al.[21, 25, 31, 68].

4.5.1. CWT of Greeley, Iverson, Leach & White [21, 25, 31, 68]

The first use of a carousel wind tunnel to perform measurements in was by Greeley and Williams [21], and later on analysed by Iversen [25], Leach [31] and White [68]. This design dates back from 1987. The idea was to use the carousel wind tunnel to measure threshold shear velocities. The carousel wind tunnel was build with dimensions: R_i = 0.356m and R_o = 0.531m and operated at a rotational velocity of 515 RPM. They performed measurement on the velocity profile, which matched their semi-empirical analytical equation until close to the inner drum. It is mentioned that this difference is due to secondary flow effects, which are not analysed further. However, it is known now that these secondary flow effect have a large influence on the flow characteristics in the carousel wind tunnel and should thus not be neglected.

In the proposed design, which can be seen in Figure 4.39, the outer drum rotates as well, creating a pseudo gravity. The gravity can be varied by varying the rotational velocity of the outer drum. By applying this, the gravitational acceleration can be varied. However, when rotating the outer drum, the detection of the particle movement becomes a lot more complicated, which should be accounted for in the design.

Secondly, it is mentioned that by coordinating the rotational velocity of both the drums, a particle could take off and land at the exact same location. This seems very unlikely as one small perturbation will result in changing the particles' path significantly.

The measurements performed by Greeley et al.[21] show good correlation. However, the next design of the carousel wind tunnel has both the pseudo gravity and tracking of a particle to lift off and land at the same location. These two additional implementations are deemed unlikely to provide detailed results, as discussed above.

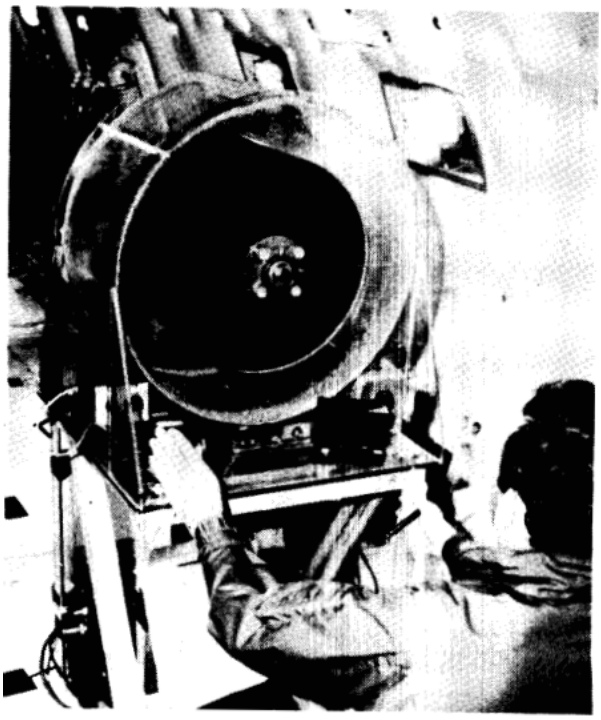

Figure 4.38: Carousel wind tunnel on board the KC-135 aircraft of NASA [21]

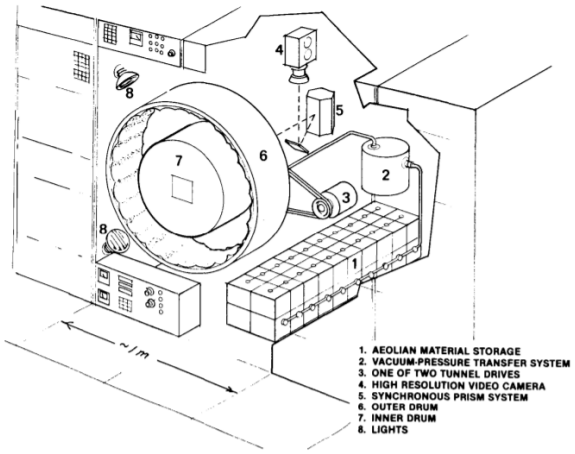

Figure 4.39: Conceptual design of the carousel wind tunnel along the International Space Station [21]

4.5.2. CWT of Demirci et al.[15]

Secondly, the experiment of Demirci et al.[15] is used for comparison. This experiment applies a carousel wind tunnel in zero-gravity conditions at extremely low pressures to erosion of planetesimals (a solid object that moves through a dense gas and dust in space). An image of their design can be seen in Figure 4.40 [15].

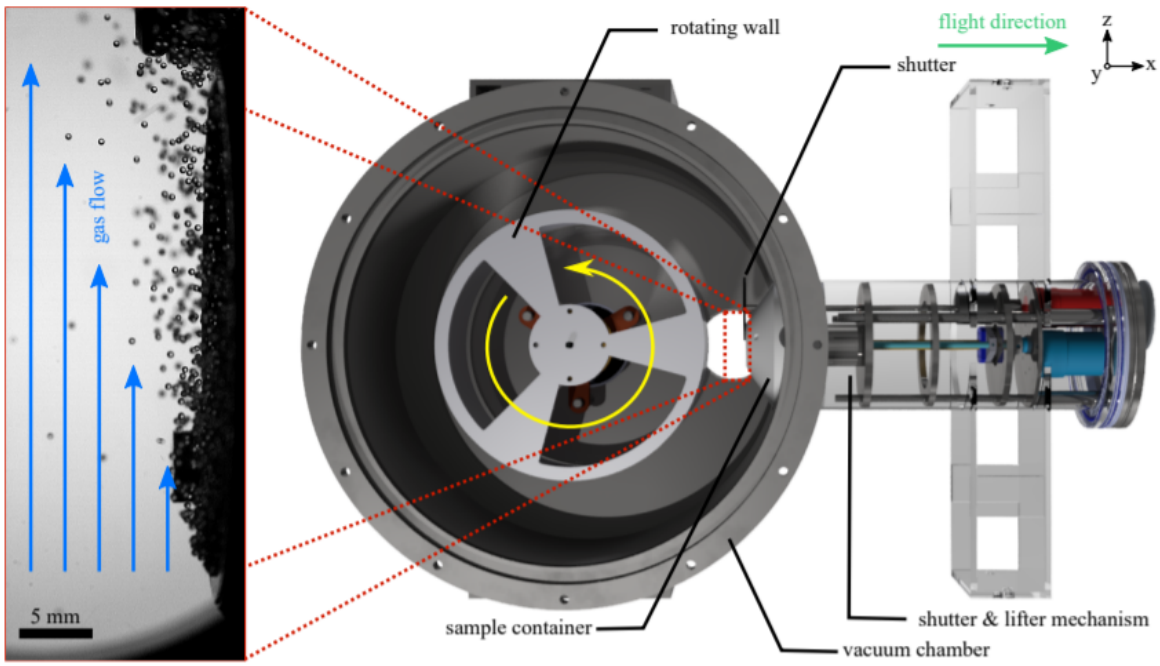

Figure 4.40: Design example of a carousel wind tunnel, by Demirci et al.[15]

The most notable difference of this design is the implementation of a sample container. The sample con-

tainer is used to store the particles which are tracked. They have to be contained in the sample container until the test facility is in zero-gravity conditions. At this point, the sample container opens and the particles are released. The velocity of the flow is done by particle tracking velocimetry technique. Next to the sample container, two important differences are the rotational velocity at which it is operated, and the pressure. The inner drum rotates at a rotational velocity of 3000 RPM. The pressure equals 10^{-1} mbar, which corresponds to 10 Pa. This is a significant difference compared to the 660 Pa where the CFD analysis is performed in.

Due to this extremely low pressure, the velocity profile in the wind tunnel will be a couette flow. This is more or less a linear line going from the inner to the outer drum. Due to the couette flow, the effect of the walls is lowered, and thus controlling the flow is relatively easy. Demirci et al. performed measurements by particle image velocimetry. The particles are tracked from a test bed. Although it was shown that a test bed on the outer drum does not significantly effect the velocity profile when having a part of the outer drum straight, the test bed implemented is relatively high in height and can thus possibly have an effect on the velocity profile. The distance between the inner and outer drum is only 12cm. The test bench has a height of 2.7cm, and thus occupies more than 20% of the gap. This is a significant height which should be investigated. One advantage is the pressure being extremely low such that a couette flow is created. Basically a linear velocity profile in the carousel wind tunnel, which has fewer impact from a disturbance compared to the complete velocity profile in the Martian atmosphere.

It is recommended to analyse the effect of the test bed on the flow due to the large uncertainty. When looking at Figure 4.41, it can be seen that the uncertainty is relatively high, definitely in the range of the shear stress. The blue line indicates the pressure at which the CFD simulation is performed, for comparison. This shear stress is determined based on the velocity profile. It is thus crucial that the velocity profile is measured accurately. The complete origin of the uncertainty is unknown. A maximum error of 5% is introduced due to the gravitational accelerations. However, the error is well above 5%, and thus a further investigation of the effect of the test bench on the velocity profile is recommended.

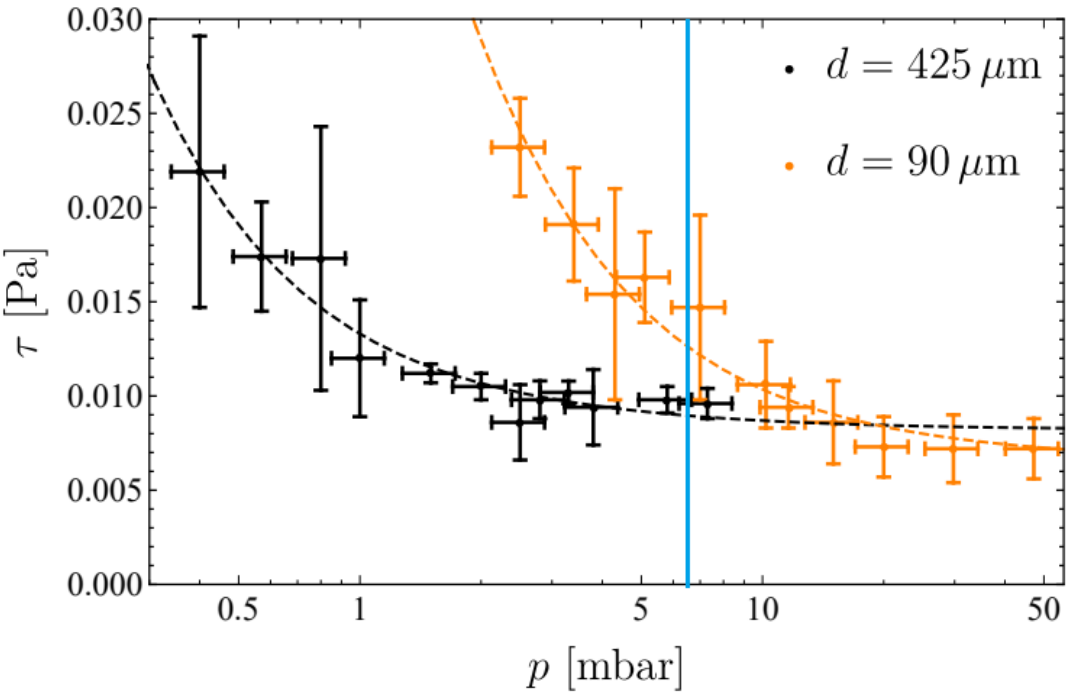

Figure 4.41: Uncertainty on the shear stress in function of the pressure [15]

4.6. Overview of the Answers on the Research Questions

Now that all the analysis has been performed, an overview on the research questions can be made. The main research question was:

> Can a velocity profile be created in a carousel wind tunnel in Martian atmospheric conditions that allows for both the measurement of aerodynamic forces and threshold shear velocities?

However, to be able to answer this, the sublevel research questions needed to be answered. The sublevel research questions where:

1. Are we able to create a boundary layer in the carousel wind tunnel that allows us to measure threshold shear velocities?
2. Can inflow and wake flow properties be generated to measure aerodynamic forces on a test object?
   (a) What is the angle and velocity of the inflow?
   (b) Does the flow recover from the wake of a test object?

The most promising application after the analysis is the application of measuring threshold shear velocities. To answer sublevel research question 1, the analysis at the required rotational velocities has been performed. It was determined that with the current configuration, threshold shear velocities are achievable. However, Taylor vortices are introduced in the flow, which could lead to more difficulties when performing measurements. Therefore, an investigation is done to increase the Reynolds number which allowed for secondary flow effects to be reduced. This is done by increasing the distance between the inner and outer drum. Furthermore, this question was linked to research question 2.B. The analysis showed that straightening the outer drum to create a test bench was possible without influencing the velocity profile significantly.

Next to the aeolian measurements, the analysis that are performed also had the goal to analyse the possibility of performing aerodynamic measurements. However, it is deemed impossible to create accurate measurements. Due to the non-uniform velocity profile, the measured forces cannot be linked to the correct flow properties. Furthermore, when implementing a test object that has significant influence on the wake, the velocity profile cannot recover, and no clear inflow property can be determined.

Before applying the carousel wind tunnel as a testing facility, the effect of the high rotational velocities on the flow need to be determined. Although Demirci et al.[15] applied rotational velocities up to 12 000 RPM, the flow at the higher pressure compared to Demirci et al. can be affected. Such high rotational velocities are often combined with strong vibrations. Further analysis must be performed on the effect of these vibrations on the flow.

5

Conclusion

In this report, the feasibility of the carousel wind tunnel as a testing facility for aeordynamic and aeolian experiments is analysed. The carousel wind tunnel is analysed at different conditions building up towards to 3D simulation. This is done to ensure sufficient knowledge is brought along when discussing the effects of performing a 3D analysis. The different analysis that have been performed are: 2D analysis while varying the Reynolds number, 2D analysis including a disturbance by a cylinder to the flow, and a 3D analysis.

First of all, a 2D analysis was performed in Earth atmospheric conditions which corresponds to a Reynolds number of 55 860. This is done to perform verification and validation. It is concluded that there is close agreement between the available experimental data, and the data from the CFD analysis. Furthermore, the analytical equations to perform verification showed close agreement as well. Next, the atmospheric conditions are changed to the values of Mars, and alterations to the dimensions of the carousel wind tunnel are made. Consequently, the Reynolds number decreased significantly within a range of [639; 2556] which resulted in a decrease of the slope of the velocity profile. This agrees with the available data from literature. From this velocity profile, the conditions needed to perform aeolian experiments are determined. It was concluded that based on the 2D simulations, to measure the threshold shear velocity of a particle with a size between 125 μm and 1000μm, a rotational velocity of 3530 RPM is needed.

Secondly, the effect of having a disturbance by a cylinder in the flow is analysed in a 2D simulation. From the results, it was concluded that the flow over the cylinder follows the conventional flow regimes of a cylinder. However, the curvature effect is significantly present. Furthermore, the cylinder has a significant effect on the velocity profile. It does not recover to its original undisturbed case, and the velocity profile remains variable over the complete carousel wind tunnel. Therefore, it is determined that aerodynamic measurements are deemed inaccurate when the test object has a significant effect on the wake of the flow.

Lastly, a 3D analysis is performed. It was expected that Taylor vortices would be present, which would disrupt the accuracy of both aerodynamic and aeolian experiments. Based on the results, while the Reynolds number is sufficiently low, the secondary flow effects remain present. The Taylor vortices do not result in the inability of the carousel wind tunnel to perform aeolian measurements, however, it can become more difficult to obtain high accuracy. Therefore, the Reynolds number can be increased, resulting in a fully turbulent state, which would ensure high accuracy results. However, the distance between the inner and outer drum need to be increased by increasing the radius of the outer drum. With this configuration, a rotational velocity of 6074 RPM would be necessary to perform aeolian experiments, based on a 2D simulation.

The carousel wind tunnel design is an interesting design that remains to have an opportunity to be useful to gain insight in phenomena occurring on Mars. However, due to its nature to create secondary flows, it remains difficult to perform accurate (aerodynamic) measurements. Aeolian experiments remain possible based on this analysis, however, further analysis on the effect of rotating the inner drum at high rotational velocities is required.

Bibliography

[1] *ANSYS CFX-Solver Theory Guide*. ANSYS, Inc., 2009.

[2] *ANSYS CFX-Solver Modeling Guide*. ANSYS, Inc, SAS IP, Inc., 2011.

[3] Mohammed Alziadeh. *Flow-sound Interaction Mechanism of a Single Spirally Finned Cylinder in Cross-Flow*. PhD thesis, 08 2017.

[4] D. C. Andereck, S. S. Luis, and H. L. Swinney. Flow regimes in a circular couette system with independently rotating cylinders. 164, 1986.

[5] John D. Jr Anderson. *Fundamentals of Aerodynamics*. McGraw-Hill Education, 2017. ISBN 978-1-259-12991-9.

[6] J. Balaram, Mimi Aung, and Matthew P. Golombek. The ingenuity helicopter on the perseverance rover. *Space Sci Rev*, 2021. doi: https://doi.org/10.1007/s11214-021-00815-w.

[7] Rafael Bardera, Suthyvann Sor, and Adelaida García-Magariño. Aerodynamics of mars 2020 rover wind sensors. 2020. doi: http://dx.doi.org/10.5772/intechopen.90912.

[8] EJ Benny Thompson and M Gunasekaran. Review analysis on laminar separation bubble at low reynolds numbers. *J. Phys.: Conf.*, 2021.

[9] Pieter Bergout, Roberto Verzicco, Richard J. A. M. Stevens, Detlef Lohse, and Daniel Chung. Calculation of the mean velocity profile for strongly turbulent taylor-couette flow at arbitrary radius ratios. *Journal of Fluid Mechanics*, 905, 2020.

[10] S. Bhattacharyya and A.K. Singh. Vortex shedding and heat transfer dependence on effective reynolds number for mixed convection around a cylinder in cross flow. *International Journal of Heat and Mass Transfer*, 53(15):3202–3212, 2010. ISSN 0017-9310. doi: https://doi.org/10.1016/j.ijheatmasstransfer.2010.03.006. URL `https://www.sciencedirect.com/science/article/pii/S0017931010001390`.

[11] M.C. Bourke et al. *Planetary Aeolian Geomorphology*. John Wiley & Sons Ltd., 2019.

[12] Hervé Bézard, Thibault Désert, Thierry Jardin, and Jean-Marc Moschetta. Numerical and experimental aerodynamic investigation of a micro-uav for flying on mars. 2020.

[13] Carlos A. de Moura and Carlos S. Kubrusly. *The Courant–Friedrichs–Lewy (CFL) Condition*. Springer, 2013. ISBN 978-0-8176-8393-1. doi: 10.1007/978-0-8176-8394-8.

[14] S. J. de Vet, J. P Merrison, M. C. Mittelmeijer-Hazeleger, E. E. van Loon, and L. H. Cammeraat. Effects of rolling on wind-induced detachment thresholds of volcanic glass on mars. 2014. doi: https://doi.org/10.1016/j.pss.2014.07.012.

[15] Tunahan Demirci, Niclas Schneider, Tobias Steinpilz, Tabea Bogdan, Jens Teiser, and Gerhard Wurm. Planetesimals in rarefied gas: Wind erosion in slip flow. *University of Duisburg-Essen, Faculty of Physics*, 2020.

[16] Thibault Desert, Thierry Jardin, Hervé Bézard, and Jean-Marc Moschetta. Numerical predictions of low reynolds number compressible aerodynamics. *Aerospace Science and Technology*, pages 211–223, 2019. ISSN 1270-9638.

[17] S. Dong. Direct numerical simulation of turbulent taylor–couette flow. *J. Fluid Mech*, 587:373–393, 2007. doi: 10.1017/S0022112007007367.

[18] M Drela. Transonic low reynolds number airfoils. *J. Aircraft, 29, 6 pp. 1106–1113*, 1992.

[19] P. R. Fenstermacher, Harry L. Swinney, and J. P. Gollub. Dynamical instabilities and the transition to chaotic taylor vortex flow. *J. Fluid Mech.*, 94(1):103–128, 1979. doi: 10.1017/S0022112079000963. URL https://doi.org/10.1017/S0022112079000963.

[20] H.C. Garner, E.W.E. Rogers, W.E.A. Acum, and E.C. Maskell. Subsonic wind tunnel wall corrections. *AGARDograph 109*, 1966.

[21] R. Greeley and R.J. Williams. Experiments in planetary and related sciences and the space station. 1987.

[22] Siegfried Grossmann, Detlef Lohse, and Chao Sun. High–reynolds number taylor-couette turbulence. *The Annual Review of Fluid Mechanics*, 2016. doi: 10.1146/annurev-fluid-122414-034353.

[23] Michael J. Hambrey and Neil F. Glasser. *Sediment Entrainment, Transport, and Deposition*, pages 984–1003. Springer Netherlands, Dordrecht, 2011. ISBN 978-90-481-2642-2. doi: 10.1007/978-90-481-2642-2_475. URL https://doi.org/10.1007/978-90-481-2642-2_475.

[24] E.L. Houghton and P.W. Carpenter. *Aerodynamics for Engineering Students Fifth Edition*. Butterworth Heinemann, 2003.

[25] J.D. Iversen and R. Greeley. Sediment-transport experiments in zero-gravity. 1987.

[26] J.D. Iversen and B.R. White. Saltation threshold on earth, mars and venus. 1982. doi: 10.1111/j.1365âĂŘ3091.1982.tb01713.x.

[27] Mohsen Jahanmiri. Laminar separation bubble: Its structure, dynamics and control. *Division of Fluid Dynamics Department of Applied Mechanics Chalmers University of Technology*, 2011. ISSN 1652-8549.

[28] K. Khuwaranyu and S. Putivisutisak. Combined low-reynolds-number k–ω model with length scale correction term for recirculating flows. *Journal of Engineering and Technology Research*, 1:171–180, 2009.

[29] Vikas S Krishnamurthy. *The Vorticity Equation on a Rotating Sphere and The Shallow Fluid Approximation*, volume 39. Discrete and Continuous Dynamical Systems, Number 11, 2019. doi: 10.3934/dcds.2019273.

[30] Pijush K. Kundu and Ira M. Cohen. *Fluid Mechanics*. Elsevier Inc, 2008. ISBN 978-0-12-373735-9.

[31] R.N. Leach, R. Greeley, J. Iversen, B. White, and J.R. Marshall. Design and calibration of the carousel wind tunnel. 1986.

[32] John H. Lienhard. *Synopsis of Lift, Drag, and Vortex Frequency Data for Rigid Circular Cylinders*. Technical Extension Service, Washington State University, 1966.

[33] Paul R. Mahaffy et al. Abundance and isotopic composition of gases in the martian atmosphere from the curiosity rover. *Science*, 2013. doi: 10.1126/science.123796.

[34] Anyoji Masayuki, Nose Kei, Ida Shingo, Numata Daiju, Nagai Hiroki, and Asai Keisuke. Low reynolds number airfoil testing in a mars wind tunnel. *American Institute of Aeronautics and Astronautics*, 2010.

[35] W.H. Mason. Configuration aerodynamics: Transonic aerodynamics of airfoils and wings. 2006.

[36] Bernard Massey. *Mechanics of Fluids*. Taylor & Francis, 2006.

[37] J. Merrison, H. Gunnlaugsson, P. NÃyrnberg, A. Jensen, and K Rasmussen. Determination of the wind induced detachment threshold for granular material on mars using wind tunnel simulations. 2007. doi: https://doi.org/10.1016/j.icarus.2007.04.035.

[38] J.P. Merrison, H. Bechtold, H. Gunnlaugsson, A. Jensen, K. Kinch, P. Nornberg, and K. Rasmussen. An environmental simulation wind tunnel for studying aeolian transport on mars. *Planetary and Space Science*, 56:426–437, 2007. doi: 10.1016/j.pss.2007.11.007.

[39] F.P. Miller, A.F. Vandome, and J. McBrewster. *Ideal Gas Law: Equation of State, Ideal Gas, Gas, Boyle's Law, Charles's Law, Kinetic Theory, Rudolf Clausius, State Function, Pressure, Volume, Amount of Substance, Mole (unit), Gas Constant, Kelvin*. Alphascript Publishing, 2009. ISBN 9786130246068. URL https://books.google.be/books?id=9s_iQgAACAAJ.

[40] Mochammad Agoes Moelyadi. Improvement of transonic aerofoil aerodynamic performance with trailing edge modification using wedge configuration. *ICAS Congress*, 2002.

[41] David Monk and Dr. Edmund A. Chadwick. Comparison of turbulence models effectiveness for a delta wing at low reynolds numbers. *7th european conference for aeronautics and space sciences (eucass)*, 2017. doi: 10.13009/EUCASS2017-653.

[42] Sean Mulligan, Giovanni De Cesare, John Casserly, and Richard Herlock. Understanding turbulent freesurface vortex flows using a taylor couette flow analogy. 2017. doi: 10.1038/s41598-017-16950.

[43] Bruce R. Munson, Donald F. Young, and Theodore H. Okiishi. *Fundamentals of Fluid Mechanics*. John Wiley & Sons, Inc., 2002.

[44] Marouan Nemri, Eric Climent, Sophie Chartona, Jean-Yves Lanoë, and Denis Ode. Experimental and numerical investigation on mixing and axial dispersion in taylor–couette flow patterns. *The Institution of Chemical Engineers*, 2012. doi: http://dx.doi.org/10.1016/j.cherd.2012.11.010.

[45] K.C. Ng, M.Z. Yusoff, K. Munisamy, H. Hasini, and N.H. Shuaib. Time-marching method for computations of high-speed compressible flow on structured and unstructured grid. *American J. of Engineering and Applied Sciences*, 2:89–94, 2008.

[46] P. Nornberg, J.P. Merrison, and H.P. Gunnlaugsson. The new danish/esa simulation wind tunnel at aarhus university. *41st Lunar and Planetary Science Conference*, 2010.

[47] Tomohisa Ohtake, Yusuke Nakae, and Tatsuo Motohashi. Nonlinearity of the aerodynamic characteristics of naca0012 aerofoil at low reynolds numbers. *JOURNAL OF THE JAPAN SOCIETY FOR AERONAUTICAL AND SPACE SCIENCES*, 55(644):439–445, 2007. doi: 10.2322/jjsass.55.439.

[48] Rodolfo Ostilla-Mónico, Roberto Verzicco, Siegfried Grossmann, and Detlef Lohse. The near-wall region of highly turbulent taylor-couette flow. *J. Fluid Mech*, 788:95–117, 2016. doi: 10.1017/jfm.2015.675.

[49] VC Patel and JY Yoon. Application of turbulence models to separated flow over rough surfaces. *J. Fluid Eng-T.*, pages 234–241, 1995.

[50] U. Peters, H. Nischl, H.A. Dwyer, and V. Denk. A numerical investigation of the karman vortex street in shear flow and comparison with experiments. *Proc. 2nd European Comput. Fluid Dyn. Conf., Stuttgart, Chichester*, pages 615 – 622, 1994. doi: 10.1017/S0022112089002429.

[51] P.P. Puttkammer. Boundary layer over a flat plate. 2013.

[52] Matthew D. Ripley and Laura L. Pauley. The unsteady structure of two-dimensional steady laminar separation. *Physics of Fluids A: Fluid Dynamics*, 5, 1993. doi: 10.1063/1.858719. URL `https://doi.org/10.1063/1.858719`.

[53] Ethan Romander, A. Witold, J. F. Koning, and Wayne Johnson. Low reynolds number airfoil evaluation for the mars helicopter rotor. *AHS International 74th Annual Forum & Technology Display*, 2018.

[54] Ben Dhia Rouae, Tilton Nils, and Martinand Denis. Impact of osmotic pressure on the stability of taylor vortices. *Journal of Fluid Mechanics*, 933:A51, 2022. doi: 10.1017/jfm.2021.1101.

[55] Hermann Schlichting and Klaus Gersten. *Boundary Layer Theory*. Springer-Verlag Berlin Heidelberg, 2017. ISBN 978-3-662-52917-1.

[56] Yaping Shag. A simple expression for wind erosion threshold friction velocity. *Journal of Geophysical Research, No. D17, pages 22,437-22,443, September 16*, 105, 2000.

[57] G. P. Smith and A. A. Townsend. Turbulent couette flow between concentric cylinders at large taylor numbers. *J. Fluid Mech., 2.01. 123, pp. 187-217*, 1982.

[58] Fook-Chi Soo. Determination of threshold velocity and entrainment rates from a copper tailings pond. *University of Tennesse*, 2001. URL `https://trace.tennessee.edu/utk_gradthes/4227`.

[59] John Southard. *Introduction to Fluid Motions and Sediment Transport*. Massachusetts Institute of Technology, 2022.

[60] B. K. Sreejith and A. Sathyabhama. Experimental and numerical study of laminar separation bubble formation on low reynolds number airfoil with leading-edge tubercles. *Journal of the Brazilian Society of Mechanical Sciences and Engineering*, 42(171), 2020. doi: 10.1007/s40430-020-2229-2. URL https://doi.org/10.1007/s40430-020-2229-2.

[61] Roland B. Stull. An introduction to boundary layer meteorology. 1988. doi: https://doi.org/10.1007/978-94-009-3027-8.

[62] G. I. Taylor. Distribution of velocity and temperature between concentric rotating cylinders. *Proceedings of the Royal Society*, 151, 1935. doi: 10.1098/rspa.1935.0163.

[63] S. ten Pas. The influence of y^+ in wall functions applied in ship viscous flows. *(Maritime Research Institute Netherlands*, 2016.

[64] W.A. Timmer. Wind tunnel wall corrections for two-dimensional testing up to large angles of attack. *Springer Nature Switzerland AG*, 2021. doi: 10.1007/978-3-030-05455-7_27-1. URL https://doi.org/10.1007/978-3-030-05455-7_27-1.

[65] Melissa G. Trainer, Michael H. Wong, Timothy H. McConnochie, Heather B. Franz, Sushil K. Atreya, Pamela G. Conrad, Franck Lefèvre, Paul R. Mahaffy, Charles A. Malespin, Heidi L.K. Manning, Javier Martín-Torres, Germán M. Martínez, Christopher P. McKay, Rafael Navarro-González, Álvaro Vicente-Retortillo, Christopher R. Webster, and María-Paz Zorzano. Seasonal variations in atmospheric composition as measured in gale crater, mars. *Journal of Geophysical Research: Planets*, 124(11):3000–3024, 2019. doi: https://doi.org/10.1029/2019JE006175. URL https://agupubs.onlinelibrary.wiley.com/doi/abs/10.1029/2019JE006175.

[66] Johnson Wayne, Withrow-Maser Shannah, Young Larry, Malpica Carlos, Koning Witold J.F., Kuang Winnie, Fehler Mireille, Tuano Allysa, Chan Athena, Datta Anubhav, Chi Cheng, Lumba Ravi, Escobar Daniel, Balaram J., Tzanetos Theodore, and Grip Håvard Fjær. Mars science helicopter conceptual design. 2020.

[67] Frank M. White. *Viscous Fluid Flow*. McGraw-Hill Education, 2006.

[68] B.R. White et al. Saltation threshold experiments conducted under reduced gravity conditions. 1986.

[69] Richard J. Wiener, Philip W. Hammer, Charles E. Swanson, David C. Samuels, and Russell J. Donnelly. The effect of a coriolis force on taylor-couette flow. *Journal of Statistical Physics*, 1991. doi: 10.1007/BF01048804.

[70] D.A. Williams and J.K. Smith. Masa facility overview: planetary aeolian laboratory. *47th Lunar and Planetary Science Conference*, 2016.

[71] C. H. K. Williamson. Oblique and parallel modes of vortex shedding in the wake of a circular cylinder at low reynolds numbers. *Journal of Fluid Mechanics*, 206:579–627, 1989. doi: 10.1017/S0022112089002429.

[72] Justin Winslow, Hikaru Otsuka, Bharath Govindarajan, and Inderjit Chopra. Basic understanding of airfoil characteristics at low reynolds numbers (10^4–10^5). *Journal of Aircraft*, 55, 2018. doi: 10.2514/1.C034415.

[73] Dominic Xavier, Fernando Manoj, G Kannan, and Kumar R. Praveen. Study on the shock formation over transonic aerofoil. *Advances in Aerospace Science and Applications*, 3(2):113 – 118, 2013. ISSN 2277-3223.

[74] T. Xiao, Z. Chen, Y. Wang, and et al. Laminar separation bubble dynamics and its effects on thin airfoil performance during pitching-up motion. *Journal of Aerospace Engineering*, 2021. ISSN 0954-4100.

[75] Zhiyin Yang. On bypass transition in separation bubbles: a review. *Propulsion and Power Research*, 8(1):23–34, 2018. doi: 10.1016/j.jppr.2018.12.004. URL https://doi.org/10.1016/j.jppr.2018.12.004.

[76] Jie-min Zhan, Yu-tian Li, Wing-hong Onyx Wai, and Wen-qing Hu. Comparison between the q criterion and rortex in the application of an in-stream structure. *Physics of Fluids*, 31(12):121701, 2019. doi: 10.1063/1.5124245. URL https://doi.org/10.1063/1.5124245.

[77] Z. Zhang and W Li. Calculation of the strength of vortex currents induced by vortex generators on flat plates and the evaluation of their performance. *Energies*, 15, 2017. doi: 10.3390/en15072442. URL https://doi.org/10.3390/en15072442.

[78] W. Zheng, H. Mahgerefteh, S. Brown, and S. Martynov. An integral multi-phase turbulence compressible jet expansion model for accidental releases from pressurized containments. 2016.

A

Appendix - Preliminary CFD Analysis of a Wing in the Carousel Wind Tunnel

A.1. Laminar Separation Bubble

Before performing a computational fluid dynamics analysis of a wing in the carousel wind tunnel, one must understand the reason for doing so. Flying on Mars results in flying at a low Reynolds number due to the low atmospheric density, which has an influence on the performance of an airfoil. To understand this influence, one must understand the phenomenon of a laminar separation bubble. A laminar separation bubble occurs at a Reynolds number below 10^5 [8], and is thus within the range of the Reynolds number of a wing on Mars.

When the flow propagates over an airfoil, up until the point of maximum thickness, the flow accelerates. Afterwards, the deceleration of the point results in an increased pressure. A positive pressure gradient is present, called an adverse pressure gradient [53]. The decreased velocity profile can be seen in Figure A.1. Due to the adverse pressure gradient, the pressure increases when the flow propagates, resulting in a deceleration of the flow due to this pressure force [24].

Looking at the velocity profile in Figure A.1, it can be seen that due to the continuous deceleration, the velocity gradient will become zero on the airfoil. This is indicated by point S in Figure A.1 and is called the separation point. Here, the resulting shear stress equals zero due to the zero velocity gradient. The relation between the shear stress and the velocity gradient can be seen in Equation A.1. At this point, the boundary layer separates from the surface and as a result, the thickness of the boundary layer increases.

$$\tau = \mu \frac{\partial u}{\partial x} \tag{A.1}$$

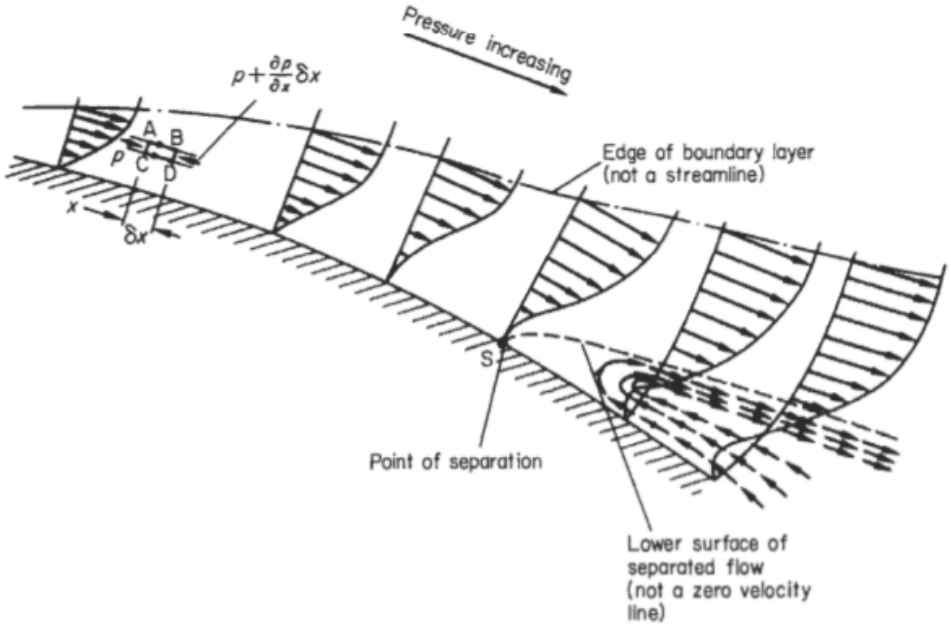

Figure A.1: Laminar boundary layer separation [24]

After separation of the laminar boundary layer, transition to turbulent flow due to disturbances in the flow can occur [75]. Due to momentum exchange with the mean flow, small disturbances cause an increased energy of the laminar boundary layer, which can result in transition from a laminar to turbulent boundary layer [60]. The thickness of the boundary layer is increased when the boundary layer becomes turbulent. A laminar separation bubble can only be formed when the boundary layer reattaches to the surface, therefore, the transition to turbulence is necessary to allow for reattachment. When the turbulent flow has gained sufficient energy, the boundary layer can reattach to the surface [74]. As a result, under the separated shear layer, a fluid bubble is present. In this bubble, called the laminar separation bubble, the flow is directed upstream due to the adverse pressure gradient. The circulatory motion of the fluid flow in the laminar separation bubble and the adverse pressure gradient which results in the flow going upstream can be seen in Figure A.2 [24].

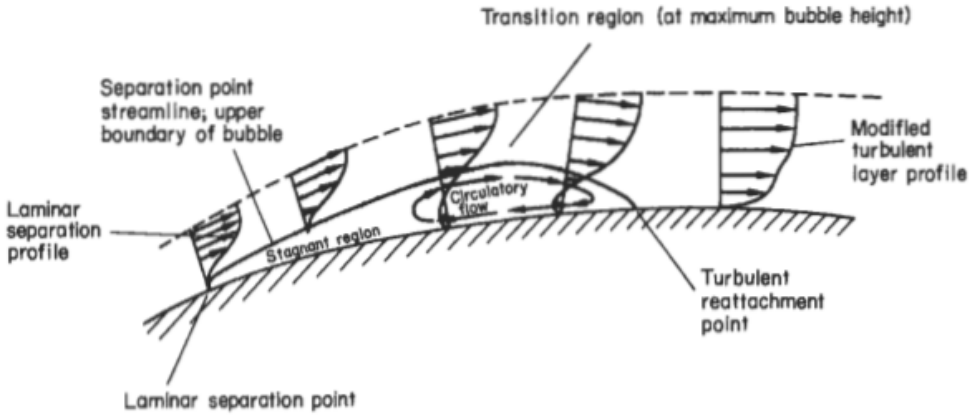

Figure A.2: Laminar separation bubble [24]

The pressure distribution is affected by the laminar separation bubble, which can be seen in Figure A.3 [27]. In the figure, the point of separation (S), transition (T) and reattachment (R) of the flow can be seen. The perturbed pressure distribution where the laminar separation bubble is present is plotted next to an inviscid pressure distribution without a laminar separation bubble. The location where the laminar separation

bubble is present can be identified by the constant pressure coefficient in the graph [52]. The constant pressure region occurs due to the recirculating velocities, which are lower compared to the velocities outside the laminar separation bubble. This region is therefore seen as a static fluid region, which result in a constant pressure. Furthermore, when the laminar separation bubble is reattached, the pressure coefficient is lower over the airfoil compared to the inviscid solution. Lastly, the reattached boundary layer remains turbulent.

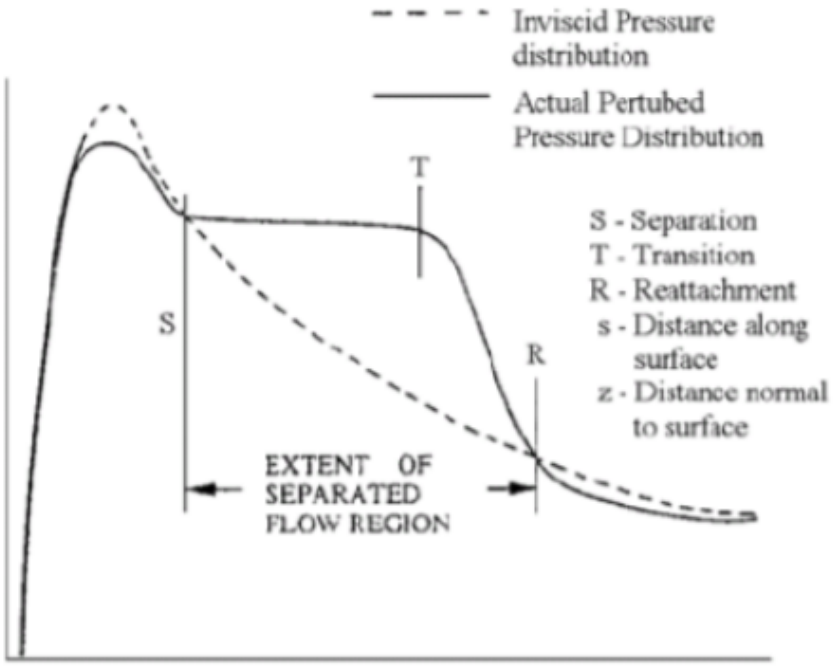

Figure A.3: Pressure distribution on the top surface of an airfoil [27]

A.2. Computational Domain of the 3D - Analysis with a Wing

As discussed above, the laminar separation bubble has a distinctive effect on the pressure distribution, and thus the performance of a wing. Therefore, valuable data would be gathered by performing measurements of a wing in Martian atmospheric conditions. To analyse the feasibility of this, a computational fluid dynamics analysis is performed with a wing in the carousel wind tunnel. Before the analysis can be done, the computational domain is determined.

The complete computational domain and blocking of the 3D analysis with a wing can be seen in Figure A.4. A close-up of the region around the wing can be seen in Figure A.5. It can be seen that the amount of blocks is significantly higher compared to the computational domain without the wing. The region around the wing is mapped by six different blocks. This is to ensure a fine transition of the mesh between the O-grid of the carousel wind tunnel, and the O-grid of the wing. Furthermore, the computational domain of the inflow is divided into five different blocks. In the wake of the wing, and for the other parts of the carousel wind tunnel, the domain is split into three different blocks per section. This is to ensure good quality near the walls of the carousel wind tunnel, and to capture the effect of the wake.

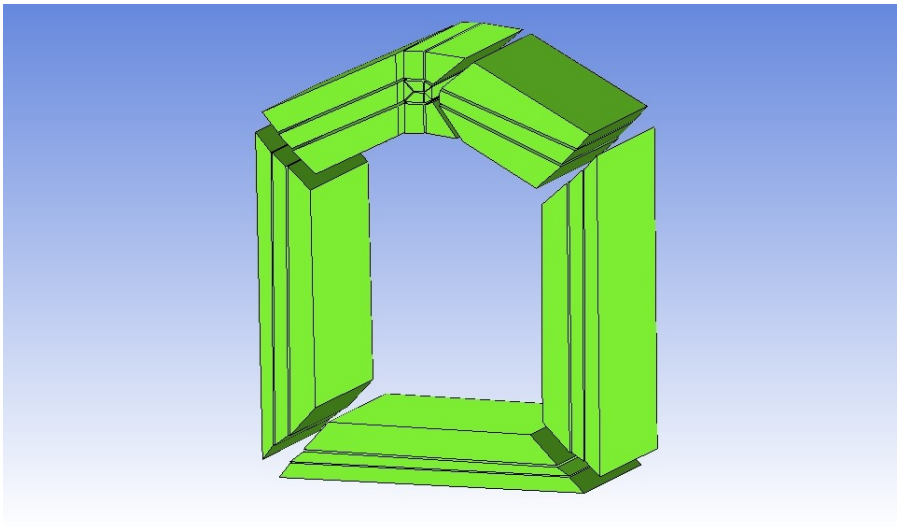

Figure A.4: Blocking of the computational domain of the 3D analysis with a wing

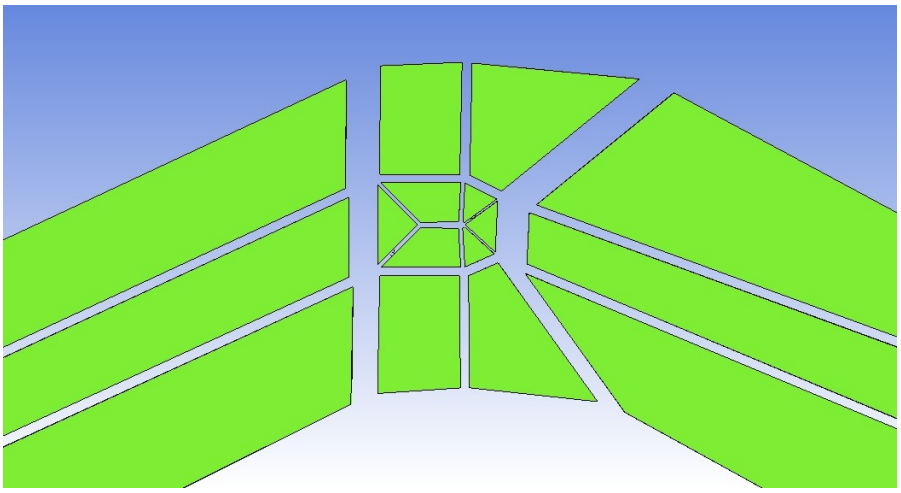

Figure A.5: Close-up of the blocking of the computational domain of the 3D analysis with a wing

A.3. Mesh of the 3D - Analysis with a Wing

Next, a mesh of the wing in the carousel wind tunnel is created. The mesh of the 3D analysis with a wing can be seen in Figure A.6, and a close-up of the area close to the wing can be seen in Figure A.7. The same distribution is used as for the regular 3D analysis. This means that there is a biexponential distribution in the direction of the depth of the carousel wind tunnel, and in between the inner and outer drum. Furthermore, an exponential distribution around the wing is used to have sufficient detail to capture the boundary layer. Due to the complexity of this flow, a large amount of cells are used. This mesh contains 10 592 374 cells, which is significantly more compared to the standard 3D analysis, which had 3 097 116 cells. This indicates the high computational effort required to gather data.

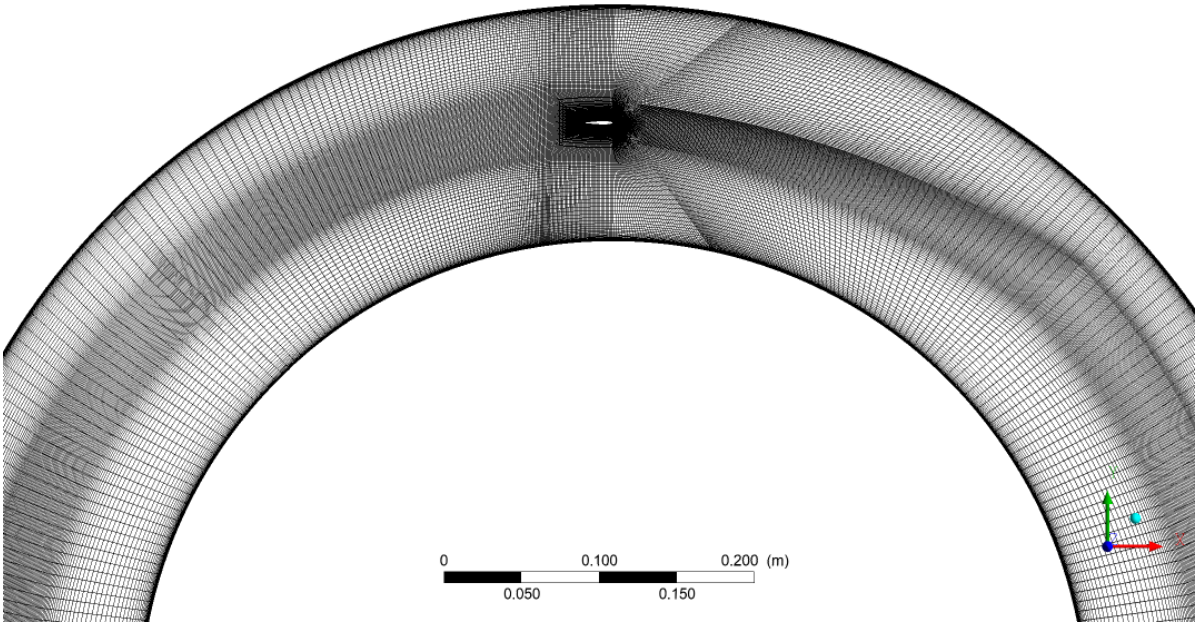

Figure A.6: Global front view of the mesh of the 3D analysis with a wing

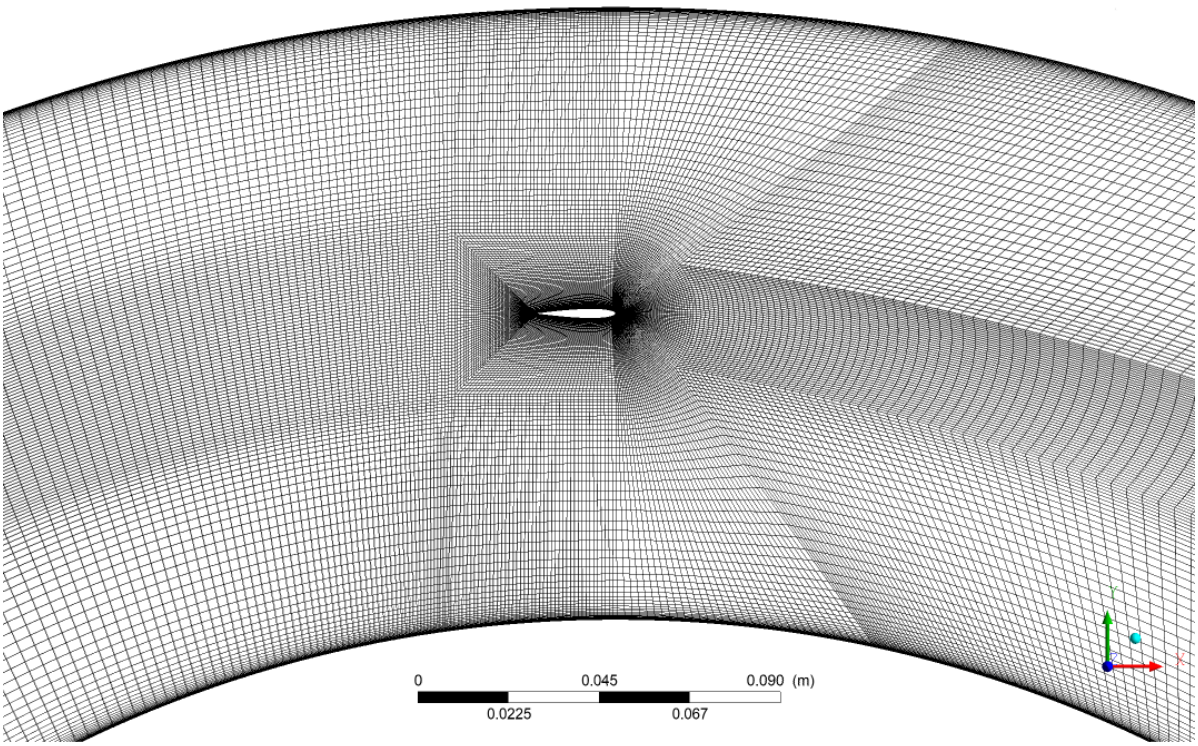

Figure A.7: Close-up of the mesh of the 3D analysis with a wing

Lastly, before analysing the results, the quality of the mesh is determined based on how well resolved the boundary layers are. All the cells can be structured correctly when performing a check by ANSYS, however, if the cell size is too large at the walls, the boundary layer will not be resolved. To check this, an often used parameter is the y^+ value with respect to the minimum value of the cell in the domain. y^+ is a normalized value based on the properties at the wall. Typically, the y^+ value has to be lower than 1 to resolve the boundary layers [63]. The values of y^+, on both the outer and inner drum, and the minimum size of the cell in the domain for the different generated meshed can be seen in Table A.1.

As can be seen, all y^+ values are lower than 1. Therefore, it is concluded that the mesh is of sufficient quality to resolve the boundary layer and is of sufficient quality to correctly assess the results provides by the CFD simulation.

Table A.1: y^+ value and minimum size for the different meshes

	y^+_{inner}	y^+_{outer}	Min. Size
Disturbance by a Wing	[0.04; 0.78]	[0; 0.125]	$4 \cdot 10^{-6}$

A.4. Results of the CFD Analysis of a Wing in the Carousel Wind Tunnel

To analyse the effect the vorticity in the carousel wind tunnel has on the measurements of a wing, the results of the CFD analysis are discussed. To determine the applicability of performing aerodynamic measurements in the carousel wind tunnel, the effect of vorticity on the wing needs to be understood. Therefore, the NACA 0012 airfoil is simulated in the carousel wind tunnel. The NACA 0012 airfoil can be seen in Figure A.8.

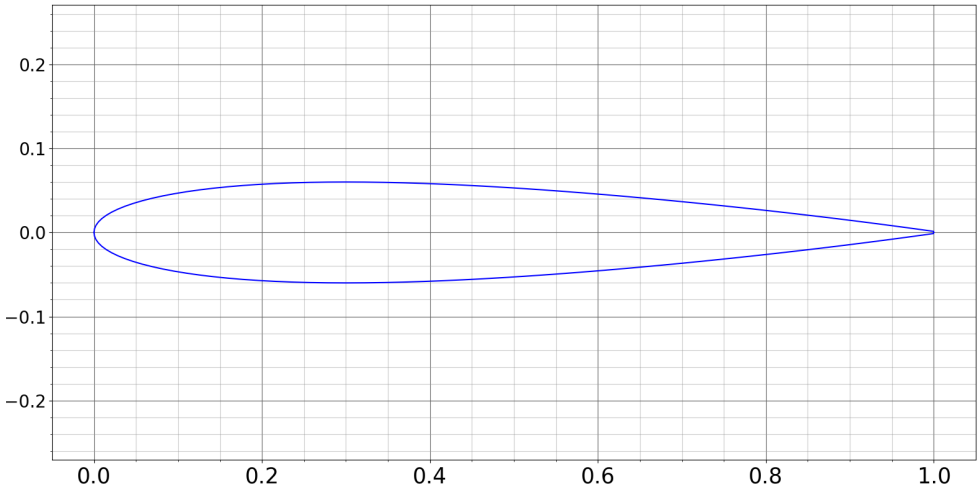

Figure A.8: NACA 0012 Airfoil

To analyse aerodynamic performance of the airfoil and flow dynamics, the angle of attack of the incoming flow must be known. This can be seen in Figure A.9. It shows an increasing angle of attack when progressing towards the middle section of the carousel wind tunnel. It must be noted that the angle of attack near the side walls (z = 0.0m and z = 0.304m) can be neglected. This is because the flow experiences an influence of the boundary layer on the side walls. The boundary layer retards the flow significantly, affecting the angle of attack, and the performance of the airfoil. Therefore, the results close to the walls will be neglected.

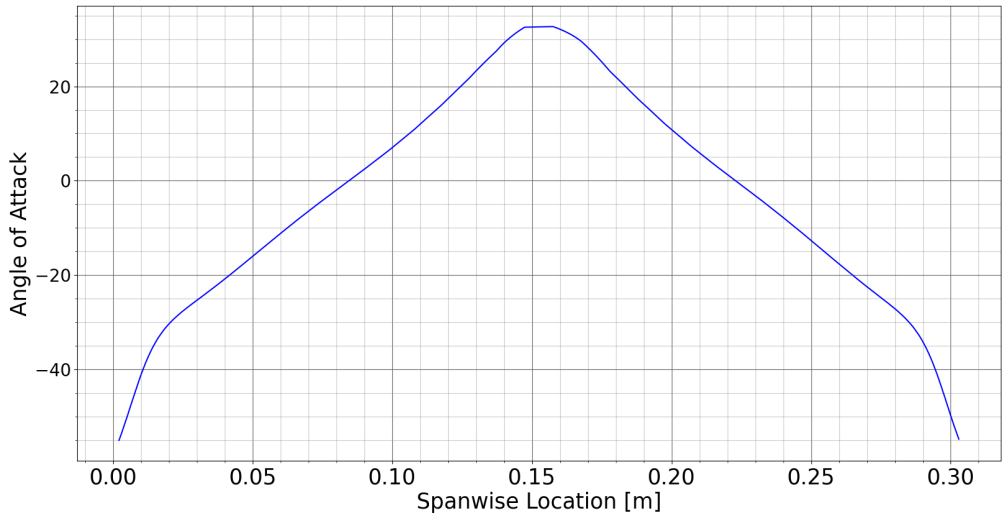

Figure A.9: Angle of attack distribution over the wing

Next, the lift coefficient and the Reynolds number are plotted over the span of the wing. Again, the values close to the side walls can be neglected. It can be seen that the lift coefficient and the angle of attack show great correlation. Since this is a symmetric airfoil, lift coefficient should be zero at zero angle of attack. The angle of attack is zero at z = 0.0845m and 0.2229m. The lift coefficient is zero at z = 0.0879m and z = 0.2196m. The difference between the spanwise location is 3.4mm and 3.3mm, respectively. The lift coefficient increases for increasing angle of attack. Although this is expected, the increase in lift coefficient is not solely due to the higher angle of attack. From Figure A.11, it can be seen that the Reynolds number increases when positioned more towards the centre. This Reynolds number almost doubles, significantly impacting the lift coefficient. The lift coefficient increases with increasing Reynolds number, and thus the increasing lift coefficient is not solely due to the increase in angle of attack.

Although the trend of the lift coefficient behaves as expected, there is a discrepancy in the angle of attack at which the lift starts to decrease, i.e. the stall angle. Comparing Figure A.9 with Figure A.10, the stall angle equals 27°. This stall angle is significantly higher than expected.

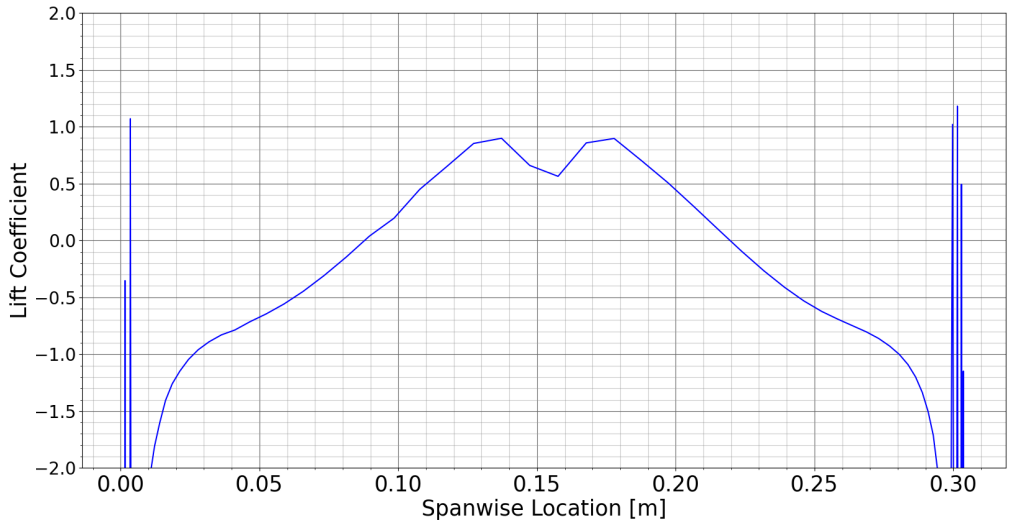

Figure A.10: Lift coefficient distribution over the wing

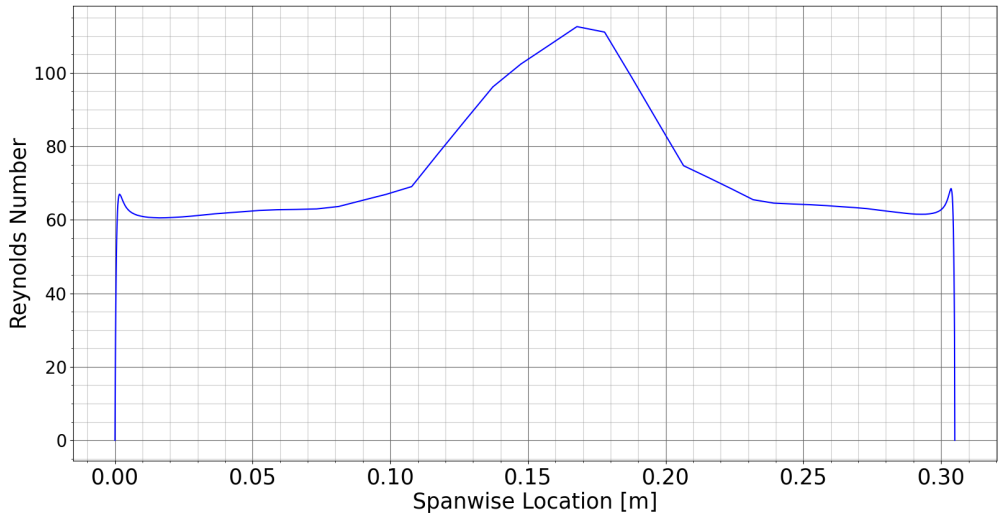

Figure A.11: Reynolds number distribution over the wing

In Section A.1, it is discussed that laminar separation bubbles are present on the airfoil for Reynolds numbers lower than 10^5. Therefore, on this wing, laminar separation bubble should definitely be present. The laminar separation bubbles are located by identifying the separation points on the wing. The separation points can be seen in Figure A.12. It must be noted that the data points are not distributed uniformly over the wing. Winslow et al.[72] investigated the presence of a laminar separation bubble at low Reynolds numbers at different angles of attack. It was concluded that the laminar separation bubble move upstream of the airfoil when increasing the angle of attack, which can be seen in Figure A.13. It must be noted that the absolute locations and angles of attack of the laminar separation bubbles cannot be compared to the CFD analysis because the Reynolds number is significantly higher ($3 \cdot 10^5$ compared to a maximum of 115). Furthermore, Winslow et al.[72] performed the analysis on an airfoil, while the CFD analysis is performed on a wing which thus has 3D effects. Therefore, the results of the CFD analysis cannot be compared to the results of the airfoil analysis in absolute terms. However, the same trend of the moving laminar separation bubble can be seen in Figure A.12, i.e. an increase in angle of attack results in a forward movement of the bubble. Furthermore, when the wing stalls, separation at the leading edge of the airfoil is present. This results in a deterioration of the lift over the airfoil, which causes the drop in lift coefficient.

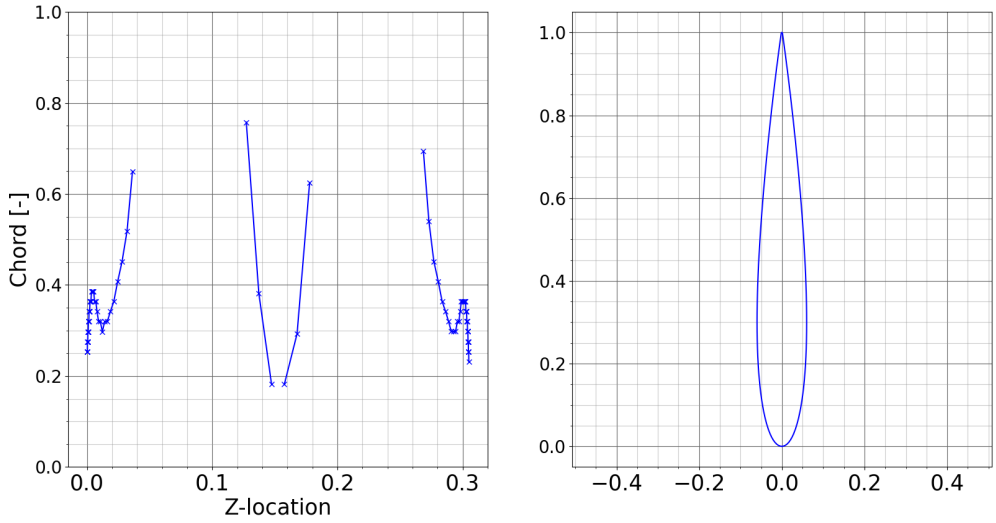

Figure A.12: Location of separation over the wing

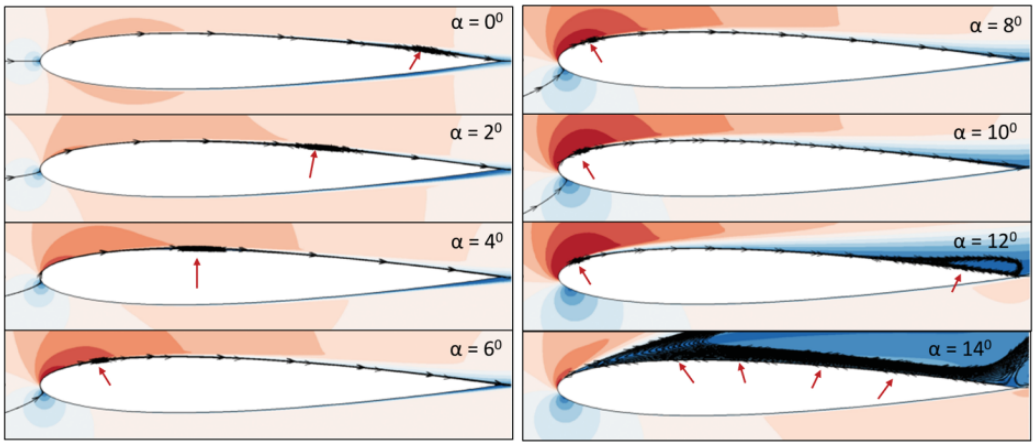

Figure A.13: Development of the laminar separation bubble with the red arrow indicating the location [72]

To conclude, the Taylor vortices result in a non-uniform flow in the carousel wind tunnel and over the wing. The vortices create different flow regimes over the wing. To allow for experiments in a uniform flow, for a certain configuration, one regime is set over the wing. This way, the configuration (rotational velocity or angle of attack for example) can be varied such that the effect of varying a certain parameter can be determined. However, since this is not the case, the flow characteristics over the airfoil will not be able to be measured accurately when performing an aerodynamic experiment in the carousel wind tunnel. In the current design of the carousel wind tunnel, it is therefore determined that no accurate aerodynamic measurements can be performed.